

Dynamic behaviour of piezoelectric sensors and their application in crack identification
for SHM

by

Huangchao Yu

A thesis submitted in partial fulfillment of the requirements for the degree of

Doctor of Philosophy

Department of Mechanical Engineering
University of Alberta

© Huangchao Yu, 2017

Abstract

The health monitoring of critical structures plays a crucial role in locating damage positions timely and preventing catastrophic failures. Much attention has been devoted to exploiting piezoelectric sensors/actuators to develop techniques of recording elastic wave signals to realize structural health monitoring (SHM). This thesis is to conduct a systematic investigation of the dynamic behaviour of piezoelectric sensors and their application in quantitative crack identification in SHM systems.

A typical SHM system contains piezoelectric sensors bonded to a host structure to be monitored. This structure is subjected to a dynamic excitation which will induce elastic wave propagation in it. When the wave encounters cracks, it will be scattered and the scattered wave will be recorded by the piezoelectric sensors. The recorded signals contain the information of the cracks thus can be used to identify the parameters of the cracks.

In this study, theoretical modelling and simulation are conducted to investigate the load transfer between the sensor and the host structure, the dispersion relation of wave propagation, and the multiple scattering of elastic waves. In addition, a crack identification technique is investigated using the voltage signals based on optimization method. Four aspects of the work were accordingly studied and examined. Firstly, a new model is developed for surface-bonded piezoelectric thin-sheets with bending effect. The coupled electromechanical behaviour and the effect of bending upon load transfer and local stress field are studied. Secondly, a new analytical treatment is provided for wave propagation in layered piezoelectric structures, including dispersion characteristics and harmonic wave propagation. The two lowest wave modes of the guided wave in such structures are analyzed.

Thirdly, a new semi-analytical solution is determined for the complicated dynamic interaction between piezoelectric sensors and cracks using pseudo incident wave method and superposition. This method has the advantages of the reliability of analytical solutions and the flexibility of typical numerical methods, and finds explicit relations between the voltage output of the piezoelectric sensor and the crack parameters. Inversely, by integrating this relation and known voltage data into an optimization process, a novel crack identification technique is established. This technique quantitatively identifies the position, the length and the orientation of typically embedded cracks effectively.

The methods proposed in this thesis can be used to understand the dynamic behaviour of piezoelectric based SHM systems, multiple scattering of elastic waves and provide insights into developing new methods for quantitative crack identification.

Preface

This section provides the statement indicating published journal and conference papers contained in this thesis. See below for details.

Chapter 1 of this thesis contains the introduction sections of a published paper: Huangchao Yu and Xiaodong Wang, “Modelling and simulation of surface-bonded piezoelectric actuators with bending effects.” *Journal of Intelligent Material Systems and Structures*, May 2016, DOI: 10.1177/1045389X16649701, and a conference paper: Huangchao Yu and Xiaodong Wang, “Dispersion characteristics of wave propagation in a piezoelectric coupled solid structure”, *Proceedings of CSME International Congress 2014*, June 1-4 2014, Toronto, Canada. I conducted this research under the supervision by Dr. Xiaodong Wang.

Chapter 2 of this thesis is based on a published journal paper: Huangchao Yu and Xiaodong Wang, “Modelling and simulation of surface-bonded piezoelectric actuators with bending effects.” *Journal of Intelligent Material Systems and Structures*, May 2016, DOI: 10.1177/1045389X16649701.

Chapter 3 of this thesis contains some results published in a refereed conference paper: Huangchao Yu and Xiaodong Wang, “Dispersion characteristics of wave propagation in a piezoelectric coupled solid structure”, *Proceedings of CSME International Congress 2014*, June 1-4 2014, Toronto, Canada. I conducted this research under the supervision by Dr. Xiaodong Wang.

Chapter 4 and 5 of this thesis don't contain contents of published journal papers. Some preliminary results were published in two referred conference paper: Xiaodong Wang,

Huangchao Yu, Abdel-Gawad S. and Chen Wang, “On the pseudo-incident wave technique for interacting inhomogeneities in electromechanical problems”, *6th International Conference on Computational Methods for Coupled Problems in Science and Engineering*, May 18-20 2015, Venice, Italy, 440-451, and Huangchao Yu and Xiaodong Wang, “The coupled dynamic behaviour of layered piezoelectric structures”, *24th International congress of theoretical and applied mechanics*, August 21-26, 2016, Montreal, Canada. Dr. Xiaodong Wang is the supervisory author. I was responsible for the modelling of piezoelectric actuator/sensors and cracks, while Abdel-Gawad S. and Chen Wang conducted the modelling of piezoelectric smart fibres and circular inhomogeneities, respectively.

Acknowledgements

I would like to gratefully thank all people who have helped me and all scholarships including the CSC Scholarship, Alberta Innovates Technology Futures (AITF) Top-up Scholarship, FGSR Travel Awards and GSA Academic Travel Award, without the support of which I could not have completed this thesis.

I would like to first express my most sincere appreciation to my supervisor Dr. Xiaodong Wang for his utmost guidance and encouragement. I was admitted into his group from my bachelor degree directly, and it was his guidance that helped me adapt to doctoral research smoothly. From him, I have not only learned valuable academic knowledge and methodology in this field but also obtained insightful advice on life and work. I would love to devote my heartfelt thanks to him for having shared countless hours of time.

I am deeply grateful to my Ph.D. supervisory committee Dr. Zengtao Chen and Dr. Zhigang Tian for their suggestions on my study. Many thanks to my candidacy exam committee members Dr. Donald Raboud and Dr. Mustafa Gul for their suggestions on my research proposal. I would also like to give my special appreciation to Dr. Xun Chen and Dr. Ming J. Zuo for their careful guidance and support during my Ph.D. study.

I am also grateful to all members in our ASML Lab, Reliability Research Lab, etc. for their help, support and friendship. It was a great pleasure and honor to work with them, including but not limited to Zhengwei Li, Huan Hu, Mohamad Molavi Nojumi, Shadi Abdel-Gawad, Dr. Xihui Liang, Dr. Guanghan Bai and Libin Liu, Zhengrong Cheng, Renjie Wang, Lei Zhang. I would like to express my special thanks to Dr. Jikai Liu, Dr. Zhixi Yang and

Chen Wang for their help. They shared with me their scientific knowledge and skills, which I could never have learned from any books.

Finally, I wish to give my deepest gratitude to family members. Thanks a million to my parents, Helin Yu and Shuiping Fan for their selfless love and support all along. My particular thanks to my fiancée, Guangfeng Chen, for her deep love, understanding and accompany which made it possible for me to complete this work today. They inspired and took care of me. Without their support and encourage, I could not have achieved this goal.

Table of Contents

Abstract	ii
Preface	iv
Acknowledgements	vi
List of Tables	xiii
List of Figures	xiv
Chapter 1: Introduction and objectives	1
1.1 Background and motivation.....	1
1.1.1 Damage identification methods	2
1.1.2 Layered piezoelectric smart structures.....	8
1.2 Literature review.....	11
1.2.1 Modelling and simulation of piezoelectric sensors/actuators	11
1.2.2 Elastic wave propagation in layered piezoelectric structures	14
1.2.3 Dynamic interaction and multiple scattering of elastic waves.....	17
1.2.4 Crack identification based on elastic waves	20
1.3 Research objectives and outline	23
Chapter 2: Modelling of piezoelectric thin-sheets with bending effects.....	26
2.1 Introduction	26
2.2 Statement and formulation of the problem	29
2.2.1 The actuator with bending.....	30

2.2.2 The elastic field of the host medium.....	34
2.2.3 Solution of the resulting integral equations	36
2.3 Results and Discussion	40
2.3.1 Comparison with FEM results	40
2.3.2 Single actuator with bending effect	43
2.3.3 Interacting actuators.....	46
2.3.4 Interfacial debonding	47
2.4 Conclusions	51
Chapter 3: Dispersion characteristics of layered piezoelectric structures.....	52
3.1 Introductions.....	52
3.2 Formulation of the problem.....	54
3.2.1 Modelling of the piezoelectric layer	55
3.2.2 Wave in the substrate	57
3.2.3 Dispersion equation	58
3.2.4 Comparison with Rayleigh wave	59
3.3 Comparison with exact solution	60
3.3.1 Governing equations	60
3.3.2 Wave motion equations.....	61
3.3.3 Exact dispersion equations.....	63
3.4 Wave propagation under a harmonic loading.....	64

3.5 Comparison and results	68
3.5.1 Dispersion curves	68
3.5.2 Physical explanation	70
3.5.3 Wave propagation under a harmonic loading	75
3.6 Discussion.....	76
3.6.1 Effect of the piezoelectricity.....	76
3.6.2 Effect of the material combinations	77
3.7 Conclusions	79
Chapter 4: Dynamic interaction between piezoelectric sensors and embedded cracks	81
4.1 Introduction	81
4.2 Problem statement and formulation.....	83
4.3 Dynamic behaviour of the piezoelectric sensor.....	86
4.3.1 Modelling of the piezoelectric smart sensor	87
4.3.2 The elastic field of the host medium.....	88
4.3.3 Governing equations and numerical solutions	92
4.4 Scattered waves of a single crack	94
4.4.1 Elasto-dynamic behaviour of a crack in elastic medium	94
4.4.2 Solution of the resulting integral equations	96
4.5 Dynamic interaction and multiple scattering of elastic waves	100
4.6 Results and discussion.....	105

4.6.1 Comparison with existing results	106
4.6.2 Dynamic interaction between piezoelectric sensors and cracks	110
4.7 Conclusions	115
Chapter 5: A novel crack identification technique using optimization methods	116
5.1 Introduction	116
5.2 Formulation of the problem	118
5.2.1 The direct problem	119
5.2.2 Sensitivity analysis.....	121
5.2.3 The inverse problem	122
5.3 Quantitative crack identification	124
5.4 Results and discussion	129
5.5 Conclusions	136
Chapter 6: Contributions and future work.....	138
6.1 Main contributions.....	138
6.1.1 A new model for piezoelectric sensors/actuators with bending effect.....	138
6.1.2 A new analytical solution for dispersion relation in layered piezoelectric structures.....	139
6.1.3 A new solution for dynamic interaction between piezoelectric sensors and cracks	139
6.1.4 A quantitative technique for quantitative crack identification.....	139

6.2 Future work.....	140
Bibliography.....	142
Appendix	153
Appendix A: The governing equations of piezoelectric materials	153
Appendix B: One dimensional piezoelectric sensor model.....	154
Appendix C: Dynamic interaction of multiple cracks	155

List of Tables

Table 1.1: Major damage identification methods based on the mechanical field.....	5
Table 2.1: Typical material properties of piezoelectric sensors.	41
Table 2.2: Typical material properties of the host structure.	41
Table 5.1: The optimization algorithm for finding the optimal estimated crack parameters from the recorded surface voltage signals of the piezoelectric smart sensor.	129
Table 5.2: Known voltage signals at 12 selected locations along the piezoelectric sensor for case 1.	131
Table 5.3: The estimated crack parameters for case 1.	132
Table 5.4: Known voltage signals at 12 selected locations for case 2.	133
Table 5.5: The estimated crack parameters for case 2.	134
Table A.1: The errors of dynamic SIFs with and without considering the dynamic interaction for different distance d between the centres of two collinear cracks..	156

List of Figures

Fig. 1.1: A typical in-service (online) SHM system	2
Fig. 1.2: (a) Near-field point scans; (b) phase array scans.....	7
Fig. 1.3: Typical examples of flat piezoelectric smart layers	10
Fig. 1.4: Schematics of a piezoelectric smart structure for crack identification.....	24
Fig. 2.1: Schematics of the actuator configuration.	30
Fig. 2.2 The actuator and the host medium.....	31
Fig. 2.3: Debonded actuator and bending deformation.....	34
Fig. 2.4: Comparison with FEM results for a single actuator ($\lambda = 0.5$).	42
Fig. 2.5: Comparison with FEM results for a debonded actuator ($\lambda = 0.5$).	43
Fig. 2.6: Interfacial stress distribution of a single actuator ($c/h=5$).....	45
Fig. 2.7: Interfacial stress distribution of a single actuator ($c/h=10$).....	45
Fig. 2.8: Interfacial stress distribution of interacting actuators ($\lambda = 0.5, \nu = 10$).....	46
Fig. 2.9: Interfacial stress distribution of interacting actuators ($\lambda = 0.1, \nu = 10$).....	47
Fig. 2.10: Interfacial shear stress of debonded actuator ($\lambda = 0.5$).....	48
Fig. 2.11: Interfacial normal stress of debonded layer ($\lambda = 0.5$).....	48
Fig. 2.12: Axial compressive force	50
Fig. 2.13: Bending moment in the debonded part.....	50
Fig. 2.14: Axial displacement of the end of the debonded part	51
Fig. 3.1: A piezoelectric layer surface-bonded to an elastic half-space substrate	54
Fig. 3.2: Stress analysis of the layer	55

Fig. 3.3: The substrate subjected to a harmonic incident wave and interfacial surface stresses	66
Fig. 3.4: Dispersion curves for the PZT4-Aluminum layered structure	69
Fig. 3.5: Dispersion curves for different densities of the piezoelectric layer	71
Fig. 3.6: Dispersion curves of the upper branch approaches the effective longitudinal velocity of the layer c_s	72
Fig. 3.7: Dispersion curve when the inertia of the piezo-layer in z direction is ignored	73
Fig. 3.8: The displacement wave field in y-direction when $k=1040/m$, $c=2000m/s$ and $t=1ms$	74
Fig. 3.9: The displacement wave field in z-direction when $k=1040/m$, $c=2000m/s$ and $t=1ms$	74
Fig. 3.10: Amplitude of strain ratio with different material combinations under different frequencies	76
Fig. 3.11: Comparison of dispersion curves with and without the piezoelectric effect..	77
Fig. 3.12: Effect of the stiffness ratio on the dispersion curve	78
Fig. 3.13: Dispersion curves for different longitudinal velocity ratio c_L/c_s (the higher order branch only exists when $c_L/c_s > 1$)	79
Fig. 4.1: The advanced piezoelectric structures with embedded cracks	84
Fig. 4.2: The pseudo-incident wave method: (a) single piezoelectric sensor problem; (b) single crack problem	85
Fig. 4.3: Superposition of wave propagation in the layered piezoelectric structures	89
Fig. 4.4: The stress components at the sensor-host interface induced by the scattered wave from the j th crack.....	101

Fig. 4.5: The stress components on the surfaces of the i th crack due to the scattered wave from the j th crack.....	103
Fig. 4.6: The amplitude of the dynamic strain ratio along the sensor under different loading frequencies.	108
Fig. 4.7: Variation of normalized dynamic SIFs versus kc for different lengths of a collinear crack induced by a normal incident wave.....	109
Fig. 4.8: Comparison of voltage output along the piezoelectric sensor surface for none crack case and with crack case under a dynamic load ($Ka=1$).	112
Fig. 4.9: Comparison of voltage output along the piezoelectric sensor surface for different loading frequencies.	112
Fig. 4.10: Comparison of voltage output along the piezoelectric sensor surface for one crack configuration and three crack configuration under a dynamic load ($Ka=2$).	114
Fig. 4.11: Variation of normalized dynamic SIFs versus ka for different locations of a parallel crack induced by a normal incident wave.....	114
Fig. 5.1: General schematics of the piezoelectric sensor systems for embedded crack identification.	119
Fig. 5.2: The flow chart for the crack identification process using harmonic wave propagation and optimization method.	125
Fig. 5.3: A two-dimensional schematic diagram to show the iteration principle of the Newton method for finding the minimum.	127
Fig. 5.4: Case 1 of three uniformly distributed collinear cracks parallel to the piezoelectric sensor subjected to a normal incident wave.	130

Fig. 5.5: The objective function vs iteration for case 1. 132

Fig. 5.6: Case 2 of one big crack parallel to the piezoelectric sensor subjected to a normal incident wave..... 133

Fig. 5.7: The objective function vs the iteration number 135

Fig. A.1: Normalized dynamic SIFs versus kc for different distances d between two near collinear cracks induced by a normal incident wave. 157

Fig. A.2: Normalized dynamic SIFs versus kc for different distances d between two collinear cracks induced by a normal incident wave. 157

Fig. A.3: Normalized dynamic SIFs versus normalized wave number kc for different orientation angles induced by a normal incident wave. 158

Chapter 1: Introduction and objectives

This chapter is divided into three sections. Section 1.1 presents the background and motivation of the thesis topic. Section 1.2 provides a comprehensive literature review of multiple scattering of elastic waves and crack identification methods. Section 1.3 introduces the research objectives and summarizes the structure of this thesis.

1.1 Background and motivation

The health monitoring of critical parts of engineering structures plays a significant role in locating the damage position timely, evaluating the reliability and safety effectively as well as preventing catastrophic failures (Boller, 2000; Chang et al., 2011). There were many major accidents due to lacking or poor structure health monitoring (SHM). Clearly, it is of significant social and economic values to study SHM techniques. SHM has attracted considerable interest among scientific research communities. Just taking SHM application in aerospace as an example, NASA has undertaken the program of "Integrated vehicle health management (IVHM)" and Boeing has conducted a project on Airplane Health Management (AHM) system. Other related technologies have been tested and used in DALTA II composite rocket engine box, F-22, F-35 and other aircraft structures. Based on previous studies, it has been established that the goal of SHM is to achieve long-term, real-time, automatic monitoring, and to provide detection results directly. However, most of the traditional monitoring methods involve human intervention, thus not practical for inaccessible cases such as aircraft and buried pipelines. In these cases, the health monitoring

system requires performing on in-service structures in isolated environments without manual interference.

A typical in-service SHM system is shown in Fig. 1.1, which mainly consists of a control centre (computer), a signal generator, a power amplifier, actuators/sensor systems, data acquisition, and damage identification methods, etc. In the scope of mechanical engineering, the efforts mainly focus on two parts: damage identification methods and actuator/sensor systems, specifically, (1) the development of reliable damage identification methods to detect damage features from the recorded signals; (2) the construction of automated health monitoring actuator/sensor systems and the work mechanism to achieve corresponding damage identifications. In the following section 1.1.1, a comprehensive survey of major damage identification methods is presented; and in section 1.1.2, piezoelectric smart sensor systems for SHM are examined.

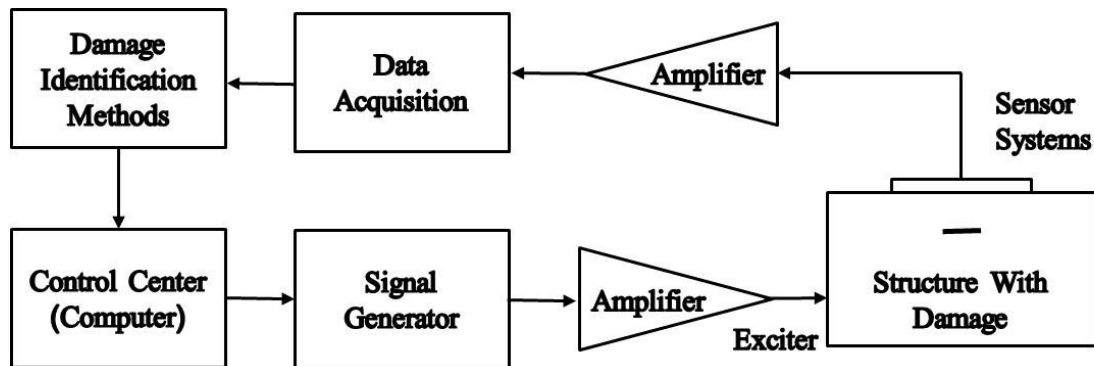


Fig. 1.1: A typical in-service (online) SHM system

1.1.1 Damage identification methods

Damage in materials or structures will change the global or local parameters, such as local stiffness, stress distribution or electro-mechanical impedance and so on. Damage identification methods are the bridge to connect these changes in signals with the structural

health conditions, and the tools to figure out the physical meaning of these changes (Su and Ye, 2009).

After decades of study, various damage identification methods have been developed for the health monitoring of different kinds of materials and structures, e.g. space vehicles and infrastructure. Many wave fields are used as monitoring signals to identify damage. The major fields for damage identification include the electromagnetic field (e.g. eddy current, radiography), thermal field (e.g. thermography), mechanical field (e.g. vibration and ultrasonic) and the combination of them. Each kind of them has its advantages and disadvantages for damage identification and the choice should be made per the sensitivity for the damage or relevant structural parameters among others.

The eddy-current-based detection and radiography-based detection are two of the mostly widely used electromagnetic testing methods. The eddy currents are closed loops of electrical current in materials or structures, which will be distorted if there are damages (Staszewski et al., 2004). Interruptions in the flow of eddy currents and changes in electromagnetic impedance, caused by damages, can be detected with proper equipment. There are many related research works in this area (Banks et al., 2002; Li et al., 2016; Ren et al., 2013; Sodano, 2007). Eddy-current-based damage identification is simple to implement and not expensive. However, it is limited to conductive materials and power-consuming. Besides, the signals are extremely complicated to interpret to identify damage. Radiography is an imaging method based on electromagnetic radiation, such as gamma-Rays or X-Rays. To obtain the image of internal structures and to identify inner damages, EM radiation will be generated and pass through the structure. In this process, a certain amount of radiation will be absorbed, and the absorption rates rely on the composition and density of the structure. Then

a detector will capture the radiation passing through the structure and provide a two-dimensional shadowgraph of the internal structures. Recent research works on radiography-based damage identification can be found in literature (Durão et al., 2015; Shi et al., 2014; Tan et al., 2011). Although radiography-based damage identification can detect surface and internal flaws with high resolution, the safety hazard of radiation to human health limits its application.

Thermography can measure temperature information using infrared radiation, which will be emitted from any object at a temperature higher than absolute zero (Modest, 2013). And it can also be used for damage detection based on the effect of damage on thermal conductivity and emissivity of test objectives (Montesano et al., 2014). Various studies have been conducted on infrared thermography and its applications on temperature measurement and non-destructive testing (Henneke et al., 1979; Munoz et al., 2016). They show that thermography-based damage identification is non-contact, non-invasive and in real time, but it only works well in controlled environments because it relies highly on the working conditions, e.g. the surrounding airflow, temperature and humidity (Usamentiaga et al., 2014). The mechanical field has also been widely used for damage identification. The major mechanic-field-based damage identification methods include vibration-based, acoustic-emission-based (AE-based) and elastic-wave-based, etc., which are summarized in Table 1.1. Different methods have their own advantages and disadvantages. Vibration-based damage identification works effectively in the case of large damages, while it has little sensitivity to small damages as they do not have a significant influence on vibration characteristics.

Table 1.1: Major damage identification methods based on mechanical field (Modified from Table 1.1 in Su and Ye, 2009).

Damage Identification Method	Mechanism	Advantage and Application	Disadvantage and Limitation
Vibration-based	Damages will reduce structural stiffness, shift natural frequencies, change mode shape and curvature, and affect damping properties etc.	<ol style="list-style-type: none"> 1. Easy to implement; 2. Low cost; 3. Particularly effective for detecting large damage¹. 	<ol style="list-style-type: none"> 1. Insensitive to small damage or damage growth; 2. Difficult to excite high frequencies; 3. Hypersensitive to boundary and environmental changes.
Acoustic-Emission-based	Sudden release of strain energy generates transient waves, whereby presence or growth of damage can be evaluated by capturing damage-emitted acoustic waves.	<ol style="list-style-type: none"> 1. Able to detect damages in different modalities (matrix crack, delamination, welding flaw and corrosion etc.); 2. Able to predict damage growth; 3. Surface mountable and good coverage. 	<ol style="list-style-type: none"> 1. Prone to contamination by environmental noise; 2. Only qualitatively detection; complex signal, passive method; 3. High damping ratio of the wave, and therefore suitable for small structures only, also locale damage only.
Elastic-wave-based	Elastic waves will be reflected and scattered by damage, and evaluation of damage can be achieved by scrutinizing the wave signals scattered by damage.	<ol style="list-style-type: none"> 1. Cost-effective, very fast inspection, repeatable; 2. Sensitive to small damage; 3. Able to detect both surface and internal damage. 	<ol style="list-style-type: none"> 1. Difficult to simulate wave propagation in complex structures; 2. Multiple wave modes simultaneously 3. Complicated multiple scattering and dynamic interactions.

¹ Large damage in this table typically refers to that above several millimeters, while small damage is normally hundreds of micrometers to several millimeters.

AE-based damage identification simply ‘listens’ for the acoustic waves induced by the energy released from active features (e.g. crack growth). Unfortunately, AE systems can only qualitatively identify how much damage in a structure, but cannot obtain the quantitative results about damage size and position.

Elastic waves can be reflected and scattered by discontinuities, and the discontinuities can then be detected by scrutinizing the scattered wave signals. Compared to vibration signals, elastic waves are more sensitive to small damages and the change of material parameters because they can be excited in a much higher frequency. Therefore, they have become one of the most popular potential signals in the damage identification (Bakker and Verweij, 2002; Biemans et al., 1999; Glushkov et al., 2016; Wandowski et al., 2015). Elastic-wave-based damage identification is cost-effective, fast and repeatable. Plus, it can detect varieties of damages like cracks, delamination and corrosion etc. embedded in structures under monitoring.

Since only longitudinal waves exist in the air and water, the wave propagation law is simple. Therefore, the medical imaging and acoustic imaging is well developed with extensive applications. However, in the case of solid structures health monitoring, it will be challenging to use the elastic waves because their wave propagation law here is complicated. The wave reflection will induce complicated mode conversion phenomena, which in turn makes signals instinctually interpretable (Achenbach, 2002). In detail, if a simple longitudinal wave propagates to an interface, it will be reflected to a longitudinal wave and a transverse wave. After several reflections in the solids, the wave propagation will become

very complicated. Thus, the mode conversion phenomenon makes it very difficult to detect cracks, especially when the multiple scattering is considered. To avoid the calculation of complex scattering field, mostly the scanning method is used. The scanning method records only two fundamental parameters, echo amplitude and time of flight (pulse transit time of waves). The widely used scanning methods in Non-Destructive Testing (NDT) include near field point scan (A-scan, B-scan, C-scan etc.) and phase array imaging, as shown in Fig. 1.2.

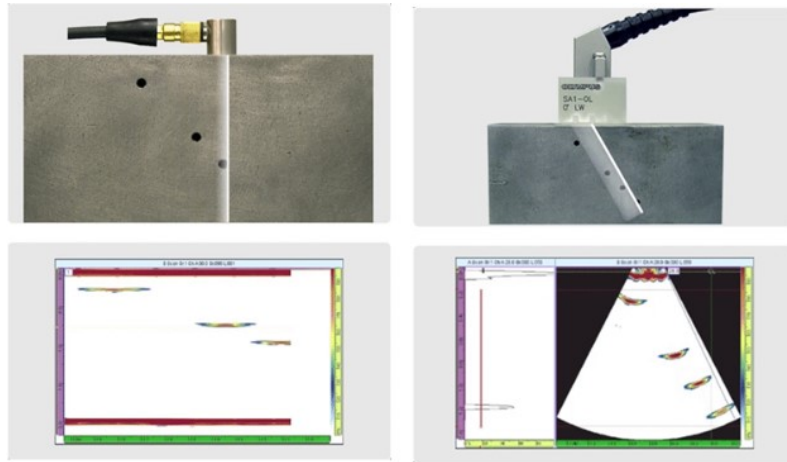


Fig. 1.2: (a) Near-field point scans; (b) phase array scans (Image used with permission from Olympus Corporation)

However, the scanning method has its disadvantages. The point scans (e.g. A-scan, B-scan, C-scan etc.) are not efficient, and cannot monitor the structural health in real time. For the phase array scans, there are blind positions, as the black sections show in the Fig. 1.2(b). Meanwhile, both just obtain qualitative information and rough images of damages. Recently, advanced signal processing techniques have been applied to deal with the ultrasonic scanning data and to further obtain the quantitative results, such as the damage position and size (Hoseini et al., 2013, 2012). Still, the scanning process limits its efficiency, and it cannot work in real time.

With the rapid increase in computer calculation speed and computing power, elastic wave fields can now be simulated and determined quickly through solving the multiple scattering problem of elastic wave induced by the interaction among discontinuities in structures under monitoring. Specifically, Elastic waves can be generated by exciters or transducers and propagate in solid structures. When there are damages, such as cracks in the structures, the wave will be reflected or scattered, and the scattered wave will be reflected again by sensors/actuators or inhomogeneities. Therefore, the dynamic interaction involves multiple scattering of the elastic waves between the damages. By solving the multiple scattering problems, the relation between recorded signals and damage parameters can be identified, and then quantitative damage identification can be realized by extracting the damage size and position information from the received wave signals.

Motivated by this idea, this project will develop a novel quantitative damage identification method based on multiple scattering of elastic waves. Considering that cracks are one of the most common damages in structures, this research will focus on the quantitative identification of crack parameters, including number, position, length and orientation of cracks. The related specific implementation methods are summarized in section 1.2.4 in the literature review.

1.1.2 Layered piezoelectric smart structures

Although there are various sensors available nowadays for in-service SHM systems, piezoelectric sensors have special comparative advantages with their quick response, high linearity, small flexible size, and low price (Li and Wang, 2009). Thus, remarkable academic interest can be noticed in exploring the techniques of using piezoelectric sensors/actuators to construct a self-monitoring smart network for collecting diagnostic elastic wave signals to

realize SHM (Crawley and De Luis, 1987; Giurgiutiu, 2005; Na and Lee, 2013; Norris and Achenbach, 1982; Wang and Huang, 2004a).

Relevant works have mostly focused on organizing sensor arrays with traditional piezoelectric transducers (Ihn and Chang, 2004; Zhu et al., 2013). Nevertheless, these transducers cannot be organized in a high density, and therefore, provide only limited information and monitoring capability of damage. Recent developments in micro-fabrication and microcircuits packaging technologies make it possible to add pre-designed electrodes on the surface of thin-sheet piezoelectrics (Masahiro Inoue et al., 2007; Saadon and Sidek, 2011), which enables the generation of general forms of elastic waves and the collection of wave signals in a much higher density. Piezoelectric smart layers or sensors can be realized in two ways. One is to directly design the active layer by using epoxy medium with bulk ceramic fibres (Horner et al., 2002; Wilkie et al., 2000; Bent et al., 1995), such as active fibre composite (Hagood et al., 1993) and macro fibre composite (Wilkie et al., 2000) etc. More examples of piezoelectric composites and polymers can be found in review papers (Jain et al., 2015; Ramadan et al., 2014; Williams et al., 2002). This way is relatively difficult to manufacture, meanwhile it is very complicated to determine the effect of the active layer on elastic waves. The other way is a continuous piezoelectric layer (e.g. bulk piezoceramic) coated with pre-designed electrode layers, such as continuous silver coating and interdigital electrodes (Hagood et al., 1993) etc. Fig. 1.3 shows typical examples of flat piezoelectric smart layers with pre-designed electrodes. Obviously, the piezoelectric layer with pre-designed electrodes can already realize collecting point signals of elastic waves in a very high density and generate most types of wave modes. The easiest way is to cut the silver coating of common used piezoelectric thin-sheets into the intended shape.

These piezoelectric smart layers can be bonded to the critical parts of solid structures to monitor their health condition. Thus, this thesis proposes a layered piezoelectric smart structure which consists of the structure, the piezoelectric sensor and the pre-designed electrodes. The thin piezoelectric layer with pre-designed electrodes will be used to record elastic wave signals. The relation between resulting signals and crack parameters can be obtained theoretically or numerically by solving the dynamic interaction problems of elastic waves in layered piezoelectric smart structures with cracks. This relation can be integrated into the time-reversal or optimization process to estimate crack parameters with the measured signals recorded by the piezoelectric smart layer.

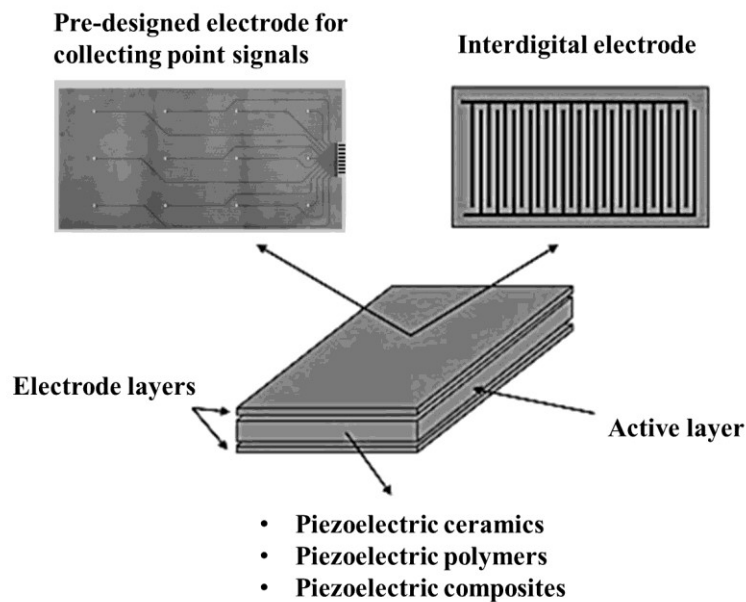


Fig. 1.3: Typical examples of flat piezoelectric smart layers (Deraemaeker and Nasser, 2010; Hurlebaus and Gaul, 2004)

1.2 Literature review

This section provides a comprehensive survey of the state-of-the-art of related works on multiple-scattering-based crack identification, including modelling and simulation of piezoelectric sensors/actuators (section 1.2.1), wave propagation in layered piezoelectric smart structures (section 1.2.2), dynamic interaction and multiple scattering of elastic waves (section 1.2.3), and crack identification based on elastic waves (section 1.2.4).

1.2.1 Modelling and simulation of piezoelectric sensors/actuators

Piezoelectric sensors, which can transform mechanical deformation to voltage signals, have been widely employed to measure deformation magnitude as well as to record elastic waves. Inversely, the piezoelectric actuators under electric field can generate a mechanical deformation and elastic waves in host structures. Various factors can influence the efficiency of actuators and sensors, including material properties of both the piezoelectric sheets and host structure, their structural configuration as well as the applied loads, etc. Developing a model for the piezoelectric elements (sensors/actuators or smart layers) to understand the electromechanical coupled behaviour between the sensors/actuators and the substrate is a prerequisite for achieving the goal of crack identification.

Scholars have extensively studied the modelling and simulation of piezoelectric sensors/actuators, using numerical, analytical and hybrid approaches. For the numerical approaches, finite element method (FEM) is one of the most powerful tools to simulate piezoelectric sensors/actuators behaviour; there are even several commercial handy software and codes such as the popular ANSYS. Despite the convenience, FEM simulation cannot explain well the corresponding physical meaning of the numerical results (Huang et al., 2010). Besides, for the dynamic response of the structures subjected to high-frequency

incident waves, small element size and accurate mesh are required, which results in a big matrix and a large amount of calculations. The shortcomings of FEM can be fixed by combining FEM with analytical approaches: FEM simulation can be applied to the piezoelectric elements and the near areas, while analytical approaches for waves in the rest of the structures (Huang et al., 2010). However, the difficulty of the hybrid method lies in solving the coupled field between their respective solutions along the boundaries, because it is a complicated problem per se to satisfy the continuous boundary between the area of FEM solution and analytical solution. Fortunately, there are many good analytical models for the flat piezoelectric actuators and sensors. The following part reviews and summarizes the analytical approaches for modelling piezoelectric sensors/actuators coupled with the host structure.

There are mainly three kinds of analytical approaches to model the coupled electro-mechanical behaviour of the piezoelectric thin sheets attached to the host structure: the pin-force model, the beam-theory-based model, the elasticity-based model.

The pin-force model was the most simplified actuator model constructed for a piezoelectric layer attached to a cantilever beam based on force balance analysis (BAILEY and UBBARD, 1985). This model assumed that the force between the layer and the beam was constantly proportional to the voltage applied to the layer. The advantage of this model lies in its simplicity and that it works well for thin and soft piezoelectric actuators. However, it is not accurate in other cases.

The beam-theory-based model, which is more elaborated than the pin-force model, was then developed by Crawley and De Luis (1987) for the same piezoelectric structure. The cantilever beam was solved using classical Euler–Bernoulli beam theory and the layer is

simplified as a one-dimensional element with uniform axial stress across its thickness. It is found through this study that the load transfer is mainly achieved by the shear stress near the two ends of the layer. In later works, this model is modified by including the bending deformation of the actuator (Crawley and Anderson, 1990) and the transverse shear force in the beam model (Im and Atluri, 1989). Based on classical beam and plate models, actuators-induced bending and extension of piezoelectric structures have been extensively studied for different geometries and loading conditions (Han and Lee, 1998; Reddy, 1999; Tzou and Tseng, 1991). In a recent study, a simple beam model has been used to evaluate the response of micro-cantilevered layers containing the effects of buffer layers and electrodes (Peng et al., 2012). In these studies, since the integrated structures are modelled as beams or plates, the local deformation near the actuators tips, which dominate the load transfer, are not properly evaluated.

The above approaches are mostly limited to the global response of the structures, where the host structures are modelled as beams, plates or shells. However, the thickness of the common used piezoelectric sheets is always very thin (<1 mm), much thinner than that of the host medium. In this case, the local stress distribution near piezoelectric sensors/actuators plays a crucial role in the load transfer of smart structures. Then the host medium can be modelled as a semi-infinite medium (half space) based on the elasticity theory, while the modelling of thin piezoelectric sensors/actuators can use the simplified models. Such treatment suits for the most commonly used thin-sheet sensors/actuators to simulate their deformation in the smart structures. Integrating the simple actuator model into the structures can provide a relatively simple but accurate prediction of the response of the smart structures. A one-dimensional model of the thin-sheet piezoelectric actuator has been developed by

Wang and Meguid (2000) to investigate the load transfer between surface-bonded/embedded actuators and a half elastic plane, and to examine the effect of interfacial debonding. This article is cited by other 67 papers, and the model is widely used to depict the coupled electro-mechanical behaviour of a piezoelectric sheet attached to structures. A modified model has also been developed to investigate the effect of the adhesive layer between the actuator and the substrate by Jin and Wang (2011). However, in these works, the bending deformation of the layer has been ignored. This project will develop a modified model of thin-sheet piezoelectric actuator bonded to elastic half planes with consideration of the bending deformation of the actuator and partial debonding along the interface to study the effect of the bending deformation and debonding.

1.2.2 Elastic wave propagation in layered piezoelectric structures

The modelling of piezoelectric sensors is one of the most fundamental issues of wave-based crack identification using piezoelectric materials, and the other one to realize the crack detection is to determine how waves propagate in the structures. Here, the works on the eigenvalue solution and general solution of wave propagation in the layered piezoelectric structures will be summarized.

The eigenvalue solution will determine the dispersion relation of wave propagation in the layered piezoelectric structures. “Dispersion is the phenomenon of phase velocity of a wave depending on its frequency” (Elachi and Zyl, 2006). The dispersion can be described using the dispersion curves, which gives the relation of the velocity of a wave to its frequency or wave number. The general solution gives the dynamic response of structures subjected to a given excitation or a specific incident wave. It can be determined following the similar process for dispersion equations. The relation between the eigenvalue solution and

the general solution can be understood by referring to the difference between free vibration and forced vibration.

The anti-plane problem of wave propagation in layered structures has been extensively studied. Typical works include the dispersion characteristics of Love waves in a piezoelectric lamina attached to a half-space (Wang et al., 2001) and the propagation of surface waves in piezoelectric coupled solids (Qian et al., 2010). Although SH waves in such structures are well understood (Jin et al., 2005; Kielczyński et al., 1990; Liu et al., 2001; Pang et al., 2016), because of the complicated mode conversion phenomena induced by reflection and scattering, the works on in-plane wave propagation in piezoelectric layers attached to solid structures are relatively limited.

Long wave propagation in layered elastic structures was first investigated by Bromwich (1898). This work was then modified by Love (1911) who also considered short waves, of which wave lengths were short compared to the thickness of the layer. Achenbach and Keshava (1967) studied the dispersion curves of waves in an isotropic elastic layer coupled by an isotropic elastic half-space. Vinh et al. (2016) derived the exact dispersion equations of Rayleigh waves in an orthotropic elastic layer bonded to an orthotropic elastic semi-infinite structure. These works provided exact models for dispersion characteristics of layered elastic structures. Wave propagation in layered piezoelectric structures has also been studied with the main focus on Lamb wave and surface wave (Datta et al., 1988; Nayfeh, 1995). Lamb wave propagation in a dielectric half-space overlaid by a thin piezoelectric layer has been studied using a simplified numerical solution of the dispersion curve by segmenting the phase velocity spectrum into different ranges (Jin et al., 2002). The Rayleigh waves propagating in a layered pre-stressed piezoelectric layered structure have been numerically

investigated by Mseddi et al. (2016). The dispersion characteristics of surface waves in a piezoelectric layer bonded to a piezo-magnetic semi-infinite host medium (Pang et al., 2008) and the wave propagation in double-layered piezoelectric plates (Cheng and Sun, 1975) have also been studied.

These works provided useful information about the characteristics of elastic waves in layered structures but were mostly from complicated numerical solutions. For cases where the layers are very thin, the approximate dispersion relation for wave in such thin layers bonded to semi-infinite structures have been studied by modelling the layer as a thin plate (Achenbach and Keshava, 1967; Tiersten, 1969), or by expanding the displacements and stresses of the layer into Taylor series along thickness of the layer (Vinh and Linh, 2012; Pham and Vu, 2014). Achenbach and Keshava obtained the approximate dispersion curves of free waves based on the Mindlin's plate theory (Achenbach and Keshava, 1967), but this model was for an elastic layer instead of piezoelectric layer. Vinh et al. developed a third order approximate equation for the dispersion relation of Rayleigh waves (Vinh and Linh, 2012), and then established a modified fourth order model (Pham and Vu, 2014). These two models provided good approximate solutions but can only determine the surface wave mode.

It is, therefore, the objective of the current study to develop a simplified yet accurate dispersion equation of wave propagation in layered structures with an elastic substrate and a surface-bonded piezoelectric layer as sensors, and then study wave propagation in this structure under in-plane harmonic loads with the transverse inertia considered. The thickness of such a piezoelectric layer is usually small (0.1-0.5 mm), and, thus, a simplified theoretical model can be developed by modelling the piezoelectric layer as an electro-elastic film. This assumption reduces the complex problem to the non-trivial solution of binary quadratic

equations. To validate the current model, the dispersion curves of the wave are determined and compared with exact models. Two major wave modes are discussed in detail, and the influence of the material and geometric properties of the structures is studied.

1.2.3 Dynamic interaction and multiple scattering of elastic waves

Elastic wave, which can be generated by actuators or transducers and propagate in solid structures, will interact with obstacles (e.g. cracks, inhomogeneities and sensors), and these dynamic interactions will result in scattered waves. If the objects are far from each other enough or the difference of the material properties is very small, then single scattering is a good approximation for the elasto-dynamic problem. Otherwise, the elastic wave propagates back and forth between two or more scatters; this physical phenomenon is called multiple scattering of elastic waves.

Multiple scattering of elastic waves is a complex and difficult frontier problem to resolve. The main numerical methods are T-matrix methods (Waterman, 1965), boundary element methods (BEM) (Cruse, 1972), and finite difference time domain method (FDTD) (Botteldooren, 1995). The T-matrix method was firstly provided by Waterman (1965) to study the electromagnetic scattering problem. This method is also called null field method (Martin, 2006). The matrix elements can be determined by matching boundary conditions for solutions of governing equations. BEM, also called the boundary integral equation method or boundary integral method (Cruse, 1972; Zhao et al., 2016), is a computational method of determining the associated system of linear partial differential equations through the discretization of an mathematically equivalent “integral equation that is defined on the boundary of the domain and an integral that relates the boundary solution to that in domain” (Ang, 2014, 2007). FDTD is a numerical elasto-dynamic modelling technique to find

approximate solutions of differential equations governing the dynamic behaviour of structures in the time domain (Botteldooren, 1995; Hosokawa, 2015; Sun and Wu, 2007).

These numerical methods have been successfully used to solve dynamic interaction problems of cracks and other inhomogeneities in an elastic medium and multiple scattering of elastic waves in structures. Typical examples include the dynamic interaction between cracks using the integral transform method (Itou, 1980), and BEM (Gross and Zhang, 1988; Zhang, 1992; Zhang and Achenbach, 1989). Examples also include the dynamic interaction between inhomogeneities using the T-matrix approach (Varadan et al., 1978), boundary integral equation method (Lee and Mal, 1995; Schafbuch et al., 1990). These methods are all based primarily on boundary integral equations, result in a system of equations which are highly singular, so they are less accurate and less efficient compared to analytical solutions (Wang et al., 2015).

Analytical or semi-analytical study of multiple scattering of elastic waves is very attractive because it provides reliable and accurate analytical solutions allows by avoiding complicated numerical integrations in BEM, but it is limited to solving only the multiple scattering of inhomogeneities in regular shapes, such as through-thickness cracks, penny-shaped cracks, circular inhomogeneities, and piezoelectric thin-sheet. For the dynamic interaction of these regular shaped scatters, analytical or semi-analytical solutions can be found with solutions of scattered field of a single scatter and pseudo incident wave (PsiW) method. The PsiW method was firstly provided by Wang and Meguid (1997) for solving multiple scattering problems in an infinite elastic medium with a through-thickness crack and an circular fibre subjected to anti-plane loadings. The proposed PsiW method reduces the complicated multiple scattering problem to a self-consistent solution of scattered waves from

a single crack/inhomogeneity problem. Then, this method was used to determine the interactions between piezoelectric actuators (Wang and Huang, 2001, 2006a), wave propagation in an infinite host structure with a crack (Wang and Huang, 2004b), and dynamic interactions among a large number of circular inhomogeneities (Wang and Wang, 2016). From these studies, we can see, instead of simulating the response of such complicated systems using purely numerical or analytical methods, the current technique will take advantage of the accuracy and reliability of analytical solutions and the flexibility of numerical methods. Using this method, the multiple scattering problem is reduced to the coupled solution of scattered waves of single inhomogeneity, for which analytical solutions or simpler numerical solutions could be derived. By considering the consistency condition between different inhomogeneities, the steady state dynamic solution of multiple interaction problems can be formulated in terms of coupled single inhomogeneity solutions (Wang et al., 2015).

However, the pseudo-incident wave technique in these studies was all applied to the dynamic interactions in infinite mediums. For the dynamic interaction problems in layered structures, the scattered waves of cracks will be reflected by interfaces between layers, resulting in complicated displacement and stress components along the interfaces, which cannot be solved by using the pseudo-incident wave technique directly.

Therefore, based on their works, this project will study the dynamic interaction of a surface-bonded piezoelectric smart sensor with embedded cracks in a half-space elastic medium, i.e. the effect of cracks upon the surface wave signals. This problem will be solved by using the pseudo-incident wave technique and proper superposition.

1.2.4 Crack identification based on elastic waves

As summarized in the previous damage identification methods, the sensing technologies for in-service SHM systems using mechanical signals are classified into two major types of approaches: the vibration-based and the wave-based (Su et al., 2006; ZOU et al., 2000). The disadvantage of the vibration-based method lies in its relative insensitivity to local small damage which cannot change its vibration characteristics and its hypersensitivity to environmental and boundary changes. Therefore it lacks reliability and accuracy in estimating small damages (Zhu et al., 2013). However, these shortcomings can be fixed by elastic waves thanks to their sensitivity to small local damages and changes of material properties, and the wave-based method offers special opportunities to identify small local cracks.

The key issue in crack detection using wave-based method is the extraction of health information, such as crack position etc., from the measured signals. With a series of advancements related to material science and other interdisciplinary fields, different diagnosis algorithms have been developed. There are mainly four kinds of approaches to identify cracks from the measured signals.

The preliminary method of interpreting elastic wave signals is to extract the health information by comparing the characteristic parameters or feature indexes of damaged structures with those of corresponding undamaged ones (Ludwig and Lord, 1996; Schulz et al., 1999). These parameters to be used for interpretation could be wave velocity, signal amplitude, time of flights (TOF), mechanical impedance, etc., in time/frequency domain. The limitation of this method is that it requires that we have the results of the undamaged

structure first and that it cannot establish a direct physical connection between the measured sensor signals and the crack parameters.

The second approach is the ultrasonic scan, as introduced in the section 1.1.1. It requires the use of a sensor array to scan the target structures. The working mechanism is simple and can image embedded cracks. However, this method requires scanning every point in the area of interest, so it is not efficient and cannot work for real-time structural health monitoring.

The third method is time-reversal technique. It is built based on the linearity of elastic waves. Through inversion calculation of the measured signals, the back-propagating elastic waves could be determined and then crack characteristics can be identified. This method has been widely used in geological exploration (Meng et al., 2006; Sun and McMechan, 1986). However, the time-reversal technique requires many sensors to obtain the comprehensive profile of the major signals, and cannot get a clear imaging because of the mode conversion of the longitudinal wave and the transverse wave.

The fourth method is to optimize objective functions of measured signals and corresponding empirical or calculation results, which are related to the crack and structural parameters. General used optimization methods are intelligence algorithm e.g. the artificial neural network (ANN), topology optimization e.g. level-set method (Liu et al., 2016; Liu and Yu, 2017) and traditional optimization methods e.g. Broyden–Fletcher–Goldfarb–Shanno (BFGS) algorithm.

Intelligence algorithms, such as the artificial neural network (ANN) and particle swarm optimization (PSO), are typical techniques for extracting health information of structures to be monitored after the algorithm has been well trained (De Fenza et al., 2015; Su et al., 2006).

Topology optimization could identify the irregularly shaped damages. Bellis and Bonnet (2013) provided a qualitative crack identification approach using elasto-dynamic topological derivative and Sun et al. (2013) presented a novel multiple flaw identification method using an enhanced artificial bee colony (EABC) algorithm and extended finite element method (XFEM). However, the intelligence algorithms require a huge amount of training data and cannot give a direct physical meaning between the input and output. Meanwhile, the topology optimization is not efficient and cannot realize the real-time detection. To keep the detection efficiency, as well as to avoid the use of many training data, traditional optimization methods can be applied to identify cracks quantitatively by combining with the theoretical elasto-dynamic solutions. Specifically, the relation between the scattered wave signals and crack parameters can be solved in the associated multiple scattering problems. This relation can be integrated into a traditional optimization algorithm to identify the unknown crack parameters from measured signals at selected locations. Bao and Wang (2009) presented a framework to identify a crack in infinite elastic structures subjected to a longitudinal incident wave using BFGS algorithm with the strain signals around the crack, and then multiple cracks detection was conducted following the same process in their later work (Bao and Wang, 2011).

This project will study the quantitative crack identification method based on traditional optimization technique and multiple scattering of elastic waves. The dynamic response and scattered wave field will be theoretically predicted for given structural and crack parameters and specific external loads by solving the associated multiple scattering problems. Inversely, the position, the length and the orientation of embedded cracks will be estimated through

local optimization of the difference of measured response data and calculated parameter-related data.

1.3 Research objectives and outline

The main objective of the current project is to conduct a systematic investigation of the dynamic behaviour of piezoelectric smart structures and its application on quantitative crack identification in SHM systems. This structure is subjected to a dynamic excitation which will induce elastic wave propagation in it. When the wave encounters cracks, it will be scattered and the scattered waves will be recorded by the piezoelectric smart sensors. The recorded signals contain the signature of the cracks thus can be used to identify the parameters of the cracks.

A typical piezoelectric smart structure is suggested in Fig. 1.4. It consists of homogeneous isotropic elastic structures attached with a thin piezoelectric smart layer with uniform thickness h . It is assumed that the poling direction of the smart layer is along the z -axis, perpendicular to the x - y plane. Since the host substrate is much thicker than the piezoelectric layer, it can be idealized as a half-space (Qian and Hirose, 2012). The thickness of the electrodes is in the scale of micrometer or even nanometer, so the effect of the electrodes can be ignored when we study the wave propagation in the substrate. To describe the structure, a global Cartesian coordinate system (y, z) is illustrated in Fig 1.4., and n local Cartesian systems (y_i, z_i) , $i = 1, 2, \dots, n$ are used to characterize the cracks. The half-lengths and the orientation angles of the cracks are assumed to be c_i and ϕ_i ($i = 1, 2, \dots, n$), respectively.

The centre of the i th crack is assumed to be located at (y_i^c, z_i^c) in the global Cartesian coordinate.

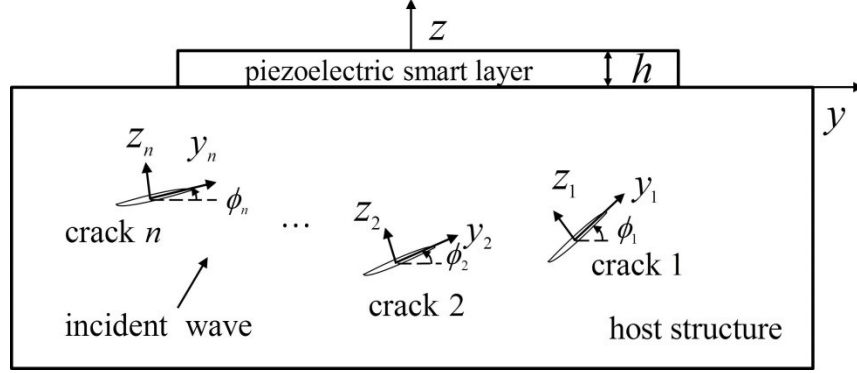


Fig. 1.4: Schematics of a piezoelectric smart structure for crack identification

When the width of the structure is significant compared with the thickness of the piezoelectric layer, there will be stress concentration at two tips of the piezoelectric layer. In this case, the constraint from the surrounding medium will limit the deformation near the tip in the direction perpendicular to y - z plane. In this case, the plane strain problem of the coupled dynamic behaviour of the structure under harmonic in-plane loading of frequency ω will be investigated. Here, the field variables, including displacement, strain and stress, are all in the form of $\bar{A}(x, y, t) = A(x, y)e^{-i\omega t}$. For convenience, $e^{-i\omega t}$ term will be omitted in the following discussion and only the magnitude $A(x, y)$ will be considered.

In this study, theoretical modelling and simulation will be conducted to investigate the load transfer along the piezoelectric-host interface, the dispersion characteristics and the dynamic interaction with cracks. In addition, a novel quantitative crack identification method will be investigated based on optimization of the objective function of the recorded surface signals and solutions of the corresponding multiple scattering problem. In this thesis, the

models are developed for the case of structures with homogeneous isotropic materials. In detail, we carry out the study with the following steps:

1. **Static model:** modelling and simulation of the surface-bonded piezoelectric actuator with bending effect. The coupled electromechanical behaviour and load transfer between the piezoelectric actuator and the host structure will be provided.
2. **Wave modes and propagation:** dispersion characteristics and wave propagation in the layered piezoelectric structure. This step is to determine the low order guided wave modes and how waves propagate under specific harmonic in-plane loading in the structure
3. **Dynamic interaction:** multiple scattering of elastic waves induced by the dynamic interaction between the piezoelectric layer and embedded cracks. The dynamic response of the structure could be predicted theoretically and the effect of the embedded cracks upon the surface signals will be determined.
4. **Crack identification:** crack identification based on the multiple scattering solutions and optimization method. The surface signals will be used to estimate the embedded cracks in the structure through local optimization of the difference of response data and theoretical prediction.

Corresponding to these four steps, this thesis will be organized in the following six chapters. The first chapter and the last chapter are the introductions and the conclusion respectively, while the four chapters in-between (Chapter 2 to Chapter 5) correspond to these four steps presented above respectively.

Chapter 2: Modelling of piezoelectric thin-sheets with bending effects

The current chapter developed a new two-dimensional analytical model for surface bonded thin-sheet piezoelectric actuators, which contains both the axial and bending deformations. The static electromechanical response of the actuator is studied under different mechanical and geometrical conditions to evaluate the effect of bending. An imperfectly bonded interface is proposed to simulate debonding and to study its effect on the actuation process. This chapter starts with a brief introduction, followed by the formulation of the problem, results and discussion, and conclusions.

The results and conclusions on the effect of bending will be used to guide the modelling and simulation of piezoelectric thin sheets surface-bonded to thick host structures in the following chapters. One dimensional model is generally accurate for the perfect-bonding case while this beam-based model (including bending effect) should be adopted when debonding happens or the signals near tips of actuators/sensors are used.

2.1 Introduction

The most commonly used piezoelectric sensors/actuators are in the form of thin-sheets, embedded or bonded to the host structure. In the modelling of thin-sheet piezoelectric actuators the effect of bending of the actuator itself is usually ignored (Banks et al., 1996; Boller, 2000; Gandhi and Thompson, 1992). In the study of such actuators, two fundamental issues need to be evaluated. The first is the electromechanical modelling of the actuator and

the second is the bonding condition at the actuator-host interface. Since the actuation is achieved by the load transfer through the interface, local stress field near the interface is very important in the process, which is significantly affected by the property of the actuators and the bonding condition (Denoyer and Kwak, 1996; Kwak and Sciulli, 1996; Park et al., 2000; Rabinovitch and Vinson, 2002).

The study of the behaviour of piezoelectric actuators bonded to electromechanical structures has received significant attention from the research and industrial communities in the area of smart structures. The literature review of modelling piezoelectric sensors/actuators is summarized in section 1.2.1, in which the methods for modelling piezoelectric sensors/actuators are mainly the pin-force model (Bailey and Ubbard, 1985) and the beam or plate theory based model (Crawley and De Luis, 1987; Peng et al., 2012). In those studies, since the integrated structures are modelled as beams or plates, the local stress fields near the ends of the actuators, which dominate the load transfer, are not properly evaluated.

Another important issue in the modelling of piezoelectric structures is the bonding condition of piezoelectric actuators. Existing studies show that the existence of interfacial debonding at the actuator-host interface can significantly affect the vibration response of laminated beams (Kim and Jones, 1996; Tylikowski, 2001). The effect of actuator bonding condition on the closed-loop vibration control of smart beams has been studied and the result indicates that the efficiency of control can be significantly reduced by interfacial debonding (Sun et al., 2001). The sensitivity of the control process to the existence of interfacial debonding has also been used to detect interfacial damage in piezoelectric structures, based on the observation that small interfacial damage can result in a detectable unstable response

of the control system (Sun and Tong, 2003). Recently, a modified structure model is used to simulate a partially debonded piezoelectric actuator in smart composite laminates by using layer-wise displacement fields (Huang et al., 2015), which indicates a significant reduction in actuation ability of the actuator for both harmonic and transient response of the structure.

Although it is well understood that the local stress distribution near piezoelectric actuators plays a very important role in the load transfer of smart structures, the corresponding study is mostly limited to the global response of the structures, as mentioned above. This is because the complicated geometries of the actuators are difficult to deal with, and therefore, simplified structural models are usually used in the analysis of the problems. Such treatments can reasonably describe the general behaviour of smart structures but cannot provide a precise description of the local stress distribution in the structures, especially when local damage such as interfacial debonding occurs. It should be noted, however, that for the most commonly used thin-sheet actuators, simple models can be used to simulate their deformation in the smart structures. Integrating the simple actuator model into the structures can provide a relatively simple but accurate prediction of the response of the smart structures. A one-dimensional model of thin-sheet piezoelectric actuators has been developed (Wang and Meguid, 2000) to study the load transfer between surface-bonded/embedded actuators and a half elastic plane and the effect of interfacial debonding. A modified model has also been developed to study the effect of the adhesive layer between the actuator and the host (Jin and Wang, 2011). In these works, the bending deformation of the actuator has been ignored.

The objective of the current study is to develop a modified model of thin-sheet piezoelectric actuators bonded to elastic half planes, including the bending deformation of

the actuators and partial debonding along the interface. The current actuator model is an extension of the work given in Wang and Meguid, (2000) with added bending effects. In the previous model, the actuator is simulated by an electro-elastic line subjected to a transverse electric field along its poling direction. In the current model, both the axial and bending deformations of the actuator are considered to study the actuation process and load transfer from the actuator under different conditions. Numerical simulation is conducted to evaluate the effects of the geometry, the material mismatch, and the debonding upon the local stress transfer with the influence of bending deformation of the actuator.

2.2 Statement and formulation of the problem

The problem envisaged is a piezoelectric actuator, in the form of thin sheets, bonded to a homogeneous and isotropic elastic half plane, subjected to plane strain deformation, as illustrated in Fig. 2.1. The host structure is modelled as a semi-infinite plane, which corresponds to the case where the thickness of the host is much larger than that of the actuator. The geometry of the actuator is defined by its length and thickness, denoted as $2c$ and h , respectively. As commonly used the poling direction of the actuator is along the z -axis in the thickness direction. A voltage (V) is applied between the upper and the lower electrodes of the actuator and generates an electric field $E_z = V/h = (V^- - V^+)/h$ across thickness of the actuator with h being the thickness of the actuator. To distinguish the actuator and the host medium, in the following discussion, subscript p and superscript s will be used to represent the piezoelectric actuator and host substrate, respectively. It should be noted that the following formulation of this problem is for structures of unit width.

To evaluate the effect of imperfect bonding conditions, it is assumed that the actuator is debonded in the central part from the host medium in the range of $|y| < b$, where b is the half length of the debonded part. It is further assumed that the debonding will form an interfacial crack, within which the surface traction is zero. This assumption ignores the effect of possible contact of the crack surfaces.

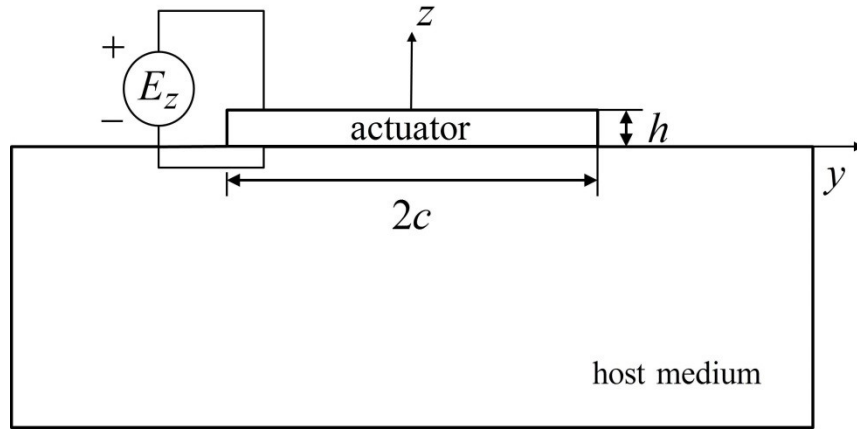


Fig. 2.1: Schematics of the actuator configuration.

2.2.1 The actuator with bending

For a typical thin-sheet actuator, the thickness is usually small compared with its length. As a result, the displacement and stress field in the actuator can be simplified by considering only the low order distribution along the thickness direction. The axial stress and displacement of the actuator can both be assumed to be linear across the thickness, and the transverse stress in the actuator is ignored. The interfacial shear and normal stresses at the actuator-host interface are denoted as τ and σ , as shown in Fig. 2.2.

These assumptions can be represented by using an electro-elastic Bernoulli-Euler beam, subjected to an electric field E_z and distributed axial and transverse

forces, τ/h and σ , as shown in Fig. 2.2. Considering the equilibrium of the actuator results in the following equations

$$d\sigma_y / dy - \tau / h = 0 \quad (2.1)$$

$$d^2M / dy^2 = \sigma \quad (2.2)$$

where σ_y is the average axial stress and M is the bending moment. The shear force Q of the beam satisfies

$$dM / dy + Q = 0, \quad dQ / dy + \sigma = 0. \quad (2.3)$$

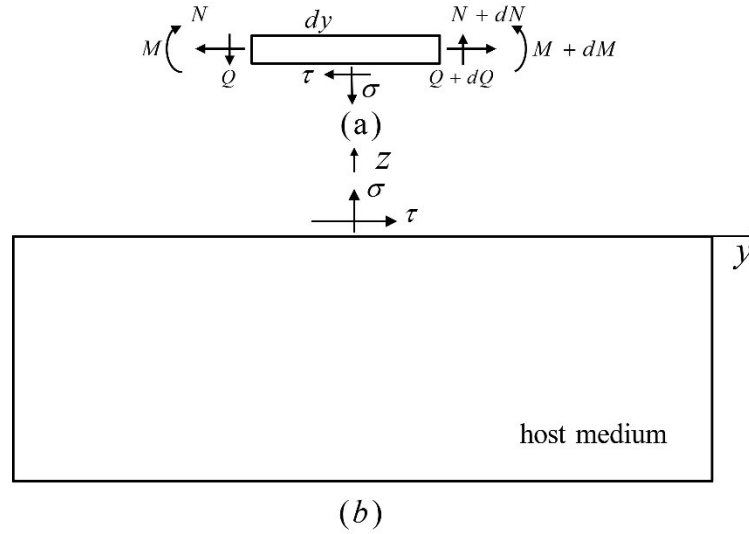


Fig. 2.2 The actuator and the host medium.

For the case where the actuator is debonded in $|y| < b$, the axial boundary conditions of the actuator at $y = b$ and $y = c$ are

$$\sigma_y = 0, |y| = c; \quad \sigma_y = -T/h, |y| = b \quad (2.4)$$

where T is the axial compressive force in the debonded part. The bending moment and the transverse shear force at the tip of the actuator are both zero to satisfy the free boundary

condition. At the ends of the debonding part, the transverse force in the z-direction must be zero to ensure equilibrium. Under the assumption of small deflection, the transverse shear force can then be assumed to be zero at the ends of the debonding part. These boundary conditions can be expressed as

$$M = 0, |y| = c; \quad M = M_b, |y| = b \quad (2.5)$$

$$Q = 0, |y| = c; \quad Q = 0, |y| = b \quad (2.6)$$

where M_b is the unknown bending moment at the end of the debonded part of the actuator, $y = b$. By integrating Equations (2.1) and (2.2), the average axial stress and bending moment in the actuator are determined in terms of the shear stress τ and the normal stress σ as

$$\sigma_y(y) = \int_b^y \frac{\tau(\xi)}{h} d\xi - T/h \quad (2.7)$$

$$M(y) = -\int_b^y \int_b^\eta \sigma(\xi) d\xi d\eta + M_b \quad (2.8)$$

The mechanical and electrical properties of piezoceramic materials can be described fully by the equation of motion

$$\sigma_{ji,j} + f_j = \rho \ddot{u}_j \quad (2.9)$$

Gauss's law

$$D_{i,i} = 0 \quad (2.10)$$

And the constitutive equations

$$\{\sigma\} = [c]\{\varepsilon\} - [e]\{E\}, \quad \{D\} = [e]\{\varepsilon\} + [\lambda]\{E\} \quad (2.11)$$

where

$$\varepsilon_{ij} = \frac{1}{2}(u_{i,j} + u_{j,i}), \quad E_i = -V_{,i} \quad (2.12)$$

In these equations, $\{\sigma\}$, $\{\varepsilon\}$ and $\{u\}$ are the stress, the strain and the mechanical displacement, f_i and ρ are the body force and the mass density, while $\{D\}$, $\{E\}$ and V represent the electric displacement, the electric field intensity and the potential, respectively. $[c]$ are the stiffness parameters for a constant electric potential, $[e]$ are the piezoelectric constants, and $[\lambda]$ are the dielectric constants for zero strains.

According to the electro-elastic line actuator model (Wang and Meguid, 2000), the effective material constants of the actuator model under plane strain condition are given by

$$E = c_{11} - \frac{c_{13}^2}{c_{33}}, \quad e = e_{13} - e_{33} \frac{c_{13}}{c_{33}}, \quad \lambda = \lambda_{33} + \frac{e_{33}^2}{c_{33}}$$

where the direction of polarization is designated as being the z-axis.

Using the constitutive relations of the actuator, its axial stress and the bending moment can be related to the axial strain ε_y , the electric field E_z and the transverse deflection of the layer u_z as

$$\sigma_y(y) = E_p \varepsilon_y(y) - e E_z \quad (2.13)$$

$$M = E_p I \frac{d^2 u_z}{dy^2} \quad (2.14)$$

where E_p and e are effective material constants given in Appendix 2.A, and $E_p I$ is the bending stiffness of the actuator, which is given, for a layer with a uniform thickness h , by

$$E_p I = E_p h^3 / 12 \quad (2.15)$$

Making use of Equations (2.7)-(2.14), the axial strain and the slope of the deflection of the layer can also be determined in terms of τ and σ as

$$\varepsilon_y(y) = \frac{1}{E_p h} \int_b^y \tau(\xi) d\xi - \frac{T}{hE_p} + \frac{eE_z}{E_p}, \quad b < y < c \quad (2.16)$$

$$\frac{du_z}{dy} = \frac{-1}{E_p I} \int_b^y \int_b^\eta \int_b^\xi \sigma(\chi) d\chi d\xi d\eta + \frac{M_b(y-b)}{E_p I} - \theta_b, \quad b < y < c \quad (2.17)$$

where $\theta_b = -du_y/dy|_{y=b}$ is the slope of the layer at $y=b$.

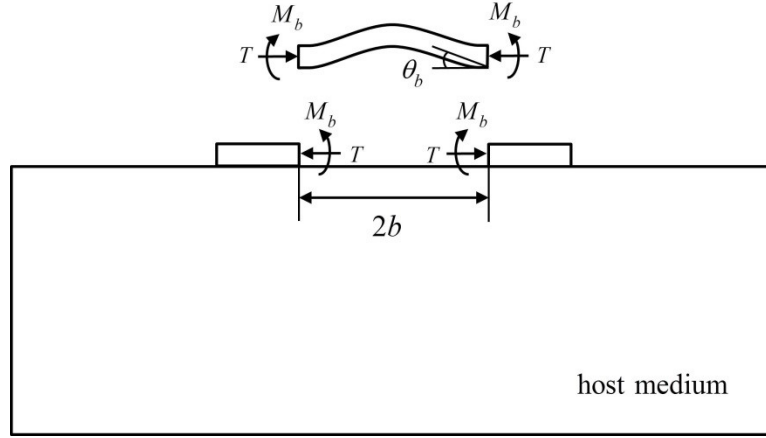


Fig. 2.3: Debonded actuator and bending deformation

2.2.2 The elastic field of the host medium

The host medium is subjected to the normal and shear stresses generated by the layer along the bonding interface. The general boundary conditions can then be expressed as

$$\sigma_{yz}^s(y,0) = \begin{cases} \tau(y) & |y| < c \\ 0 & |y| < b, |y| > c \end{cases}, \quad \sigma_z^s(y,0) = \begin{cases} \sigma^-(y) & |y| < c \\ 0 & |y| < b, |y| > c \end{cases} \quad (2.18)$$

This is a well-established problem in elasticity (Muskhelishvili, 1977). The resulting elastic field by the applied forces given by Equation (2.18), ε_y^s and du_z^s/dy , can be obtained by using the fundamental solutions for concentrated forces and the superposition principle as

$$\varepsilon_y^s(y,0) = \frac{1-2\nu}{1-\nu} \frac{1}{\bar{E}} \sigma(y) - \frac{2}{\pi \bar{E}} \int_{-c}^{-b} \frac{\tau(\xi)}{y-\xi} d\xi - \frac{2}{\pi \bar{E}} \int_b^c \frac{\tau(\xi)}{y-\xi} d\xi, \quad b < y < c \quad (2.19)$$

$$\frac{\partial u_z^s(y,0)}{\partial y} = -\frac{1-2\nu}{1-\nu} \frac{1}{\bar{E}} \tau(y) - \frac{2}{\pi \bar{E}} \int_{-c}^{-b} \frac{\sigma(\xi)}{y-\xi} d\xi - \frac{2}{\pi \bar{E}} \int_b^c \frac{\sigma(\xi)}{y-\xi} d\xi, \quad b < y < c \quad (2.20)$$

where ν is the Poisson's ratio and $\bar{E} = E_s / (1-\nu^2)$ with E_s being Young's modulus of the host medium.

Considering the continuity of the displacements along the actuator-host interface, and using Equations (2.19) and (2.20), following governing equations are obtained

$$\begin{aligned} & -\frac{1-2\nu}{1-\nu} \frac{1}{\bar{E}} \sigma(y) + \frac{2}{\pi \bar{E}} \int_{-c}^{-b} \frac{\tau(\xi)}{y-\xi} d\xi + \frac{2}{\pi \bar{E}} \int_b^c \frac{\tau(\xi)}{y-\xi} d\xi \\ & + \frac{1}{hE_p} \int_b^y \tau(\xi) d\xi - \frac{T}{hE_p} + \frac{eE_z}{E_p} = 0, \quad b < y < c \end{aligned} \quad (2.21)$$

$$\begin{aligned} & \frac{1-2\nu}{1-\nu} \frac{1}{\bar{E}} \tau(y) + \frac{2}{\pi \bar{E}} \int_{-c}^{-b} \frac{\sigma(\xi)}{y-\xi} d\xi + \frac{2}{\pi \bar{E}} \int_b^c \frac{\sigma(\xi)}{y-\xi} d\xi \\ & - \frac{1}{E_p I} \int_b^y \int_b^\eta \int_b^\xi \sigma(\chi) d\chi d\xi d\eta + \frac{M_b(y-b)}{E_p I} - \theta_b = 0, \quad b < y < c \end{aligned} \quad (2.22)$$

Making use of Equations (2.7), (2.8) and the boundary conditions (2.4) and (2.5), T and M can be expressed in terms of τ and σ as

$$T = \int_b^c \tau(\xi) d\xi \quad (2.23)$$

$$M_b = \int_b^c \int_b^y \sigma(\xi) d\xi dy \quad (2.24)$$

and

$$\int_b^c \sigma(\xi) d\xi = 0. \quad (2.25)$$

By analyzing the debonded part of the actuator deformation θ_b can be determined in terms of the bending moment M_b at $y = b$ as

$$\theta_b = \frac{M_b}{E_p I} b . \quad (2.26)$$

The axial force T is related to the axial displacement of the actuator in the debonded part

$$\Delta u = \frac{\sigma_b - T/h}{E_p} b, \quad (2.27)$$

where $\sigma_b = eE_z$ is the block stress of the actuator. The axial deformation of the actuator should be the same as the corresponding horizontal relative displacement of the host medium between the two ends of the debonding part. This condition results in the following additional equation, associated with the unknown force T ,

$$\frac{2}{\pi \bar{E}} \left[\int_{-c}^{-b} \ln \left| \frac{b-\xi}{\xi} \right| \tau(\xi) d\xi + \int_b^c \ln \left| \frac{b-\xi}{\xi} \right| \tau(\xi) d\xi \right] + \frac{\sigma_b - T/h}{E_p} b = 0 . \quad (2.28)$$

2.2.3 Solution of the resulting integral equations

The electromechanical behaviour of the actuator system is governed by the obtained singular integral Equations (2.21), (2.22) and (2.28) under the conditions defined by (2.23), (2.24) and (2.25).

The stresses and the bending moment are normalized by

$$\tau^* = \tau / p, \quad \sigma^* = \sigma / p, \quad M_b^* = M_b / M_0, \quad \theta_b^* = \theta_b / (\sigma_b / E_p) \quad (2.29)$$

with

$$p = \frac{\pi \bar{E}}{2 E_p} \sigma_b = \frac{\pi e E_z \bar{E}}{2 E_p}, \quad M_0 = \frac{I \sigma_b}{b}. \quad (2.30)$$

The governing equation of the problem can then be expressed as

$$\int_{-c}^{-b} \frac{\tau^*(\xi)}{y-\xi} d\xi + \int_b^c \frac{\tau^*(\xi)}{y-\xi} d\xi - \frac{\pi \bar{E}}{2E_p h} \int_y^c \tau^*(\xi) d\xi - \frac{1-2\nu}{1-\nu} \frac{\pi}{2} \sigma^* = -1, \quad b < y < c \quad (2.31)$$

$$\int_{-c}^{-b} \frac{\sigma^*(\xi)}{y-\xi} d\xi + \int_b^c \frac{\sigma^*(\xi)}{y-\xi} d\xi - \frac{\pi \bar{E}}{4E_p h} \int_b^y (y-\xi)^2 \sigma^* d\xi + \frac{1-2\nu}{1-\nu} \frac{\pi}{2} \tau^* + M_b^* \frac{y-b}{b} + \theta_b^* = 0, \quad b < y < c \quad (2.32)$$

$$\int_{-c}^{-b} \ln \left| \frac{b-\xi}{\xi} \right| \tau^*(\xi) d\xi + \int_b^c \ln \left| \frac{b-\xi}{\xi} \right| \tau^*(\xi) d\xi - \frac{Tb}{h\sigma_b} = -b \quad (2.33)$$

$$\int_b^c \tau^*(\xi) d\xi = \frac{2E_p T}{\pi \bar{E} \sigma_b}, \quad \int_b^c \sigma^*(\xi) d\xi = 0, \quad \int_b^c \sigma^*(\xi) \xi d\xi = -\frac{2E_p M_b}{\pi \bar{E} \sigma_b} \quad (2.34)$$

From these governing equations the shear and normal stresses τ and σ , the axial force T in the actuator, and the bending moment M_b can be determined from the applied electric field.

The resulting governing equations are singular integral equations (Wang and Meguid, 2000), for which the solution involves a square-root singularity at the two tips of the debonding part and the two ends of the actuators (Muskhelishvili, 1977). To solve these governing equations, two local coordinate systems for the two bonded parts of the actuator will be introduced. For the first local coordinate system the origin is at the centre of the left bonded part of the actuator ($-c < y < -b$) with a new coordinate η_1 , and for the second the origin is at the centre of the left bonded part of the actuator ($b < y < c$) with a new coordinate η_2 , with η_1 and η_2 being given by

$$\eta^{(1)} = \left(y + \frac{c+b}{2} \right) / \left(\frac{c-b}{2} \right), \quad \eta^{(2)} = \left(y - \frac{c+b}{2} \right) / \left(\frac{c-b}{2} \right) \quad (2.35)$$

As a result, the left and right ends of the two bonded parts correspond to -1 and +1, respectively, in the local coordinate systems. The problem considered here is symmetric in

the horizontal direction, and therefore, only the right bonded part of the actuator $b < y < c$ need to be considered in the following discussion. For simplicity, the superscript "2" referring to this part of the actuator will be omitted.

To solve these governing equations, the shear and normal stresses τ^* and σ^* can be expressed in the local coordinate ($\eta = \eta^{(2)}$) in terms of Chebyshev polynomials

$$\begin{aligned}\tau^*(\eta) &= \frac{1}{\sqrt{1-\eta^2}} \sum_{i=0}^{\infty} d_i T_i(\eta), \\ \sigma^*(\eta) &= \frac{1}{\sqrt{1-\eta^2}} \sum_{i=0}^{\infty} e_i T_i(\eta)\end{aligned}\tag{2.36}$$

where T_i are Chebyshev polynomials of the first kind with $T_i(\eta) = \cos(i\theta)$ and $\cos\theta = \eta$. To provide a solution to the problem, the Chebyshev polynomial will be truncated to the $(N-2)$ th term. The equations for the boundary conditions will be satisfied at the selected collocation points given by

$$\eta_i = \cos \frac{j-1}{N-1} \pi, \quad j=2,3, \dots, N-1\tag{2.37}$$

Equations (2.31) and (2.32) lead to

$$\begin{aligned}-\pi \sum_{i=0}^{N-2} d_i \left\{ \frac{\sin\left(i \frac{j-1}{N-1} \pi\right)}{\sin\left(\frac{j-1}{N-1} \pi\right)} + \frac{\lambda\alpha}{\pi i} \sin\left(i \frac{j-1}{N-1} \pi\right) + \left[\sqrt{y_{1j}^{*2} - 1} - y_{1j}^* \right]^i / \sqrt{y_{1j}^{*2} - 1} \right\} \\ - \frac{1-2\nu}{1-\nu} \frac{\pi}{2} \sum_{i=1}^{N-2} e_i \left\{ \frac{\cos\left(i \frac{j-1}{N-1} \pi\right)}{\sin\left(\frac{j-1}{N-1} \pi\right)} \right\} = -1,\end{aligned}\tag{2.38}$$

$$j=2,3, \dots, N-1$$

$$\begin{aligned}
& -\frac{1-2\nu}{1-\nu} \frac{\pi}{2} \sum_{i=1}^{N-2} d_i \left\{ \frac{\cos\left(i \frac{j-1}{N-1} \pi\right)}{\sin\left(\frac{j-1}{N-1} \pi\right)} \right\} - \pi \sum_{i=1}^{N-2} e_i \left\{ \frac{\sin\left(i \frac{j-1}{N-1} \pi\right)}{\sin\left(\frac{j-1}{N-1} \pi\right)} - \left[\sqrt{y_{1j}^{*2} - 1} - y_{1j}^* \right]^i / \sqrt{y_{1j}^{*2} - 1} \right\} \\
& - \frac{\pi \bar{E}}{4E_p I} \bar{c}^3 \sum_{i=1}^{N-2} e_i \int_{-1}^{\eta_j} (\eta_j - \bar{\xi})^2 \frac{T_i(\bar{\xi})}{\sqrt{1-\bar{\xi}^2}} d\bar{\xi} + (\eta_j + 1) \frac{\bar{c}}{b} M_b^* + M_b^* = 0,
\end{aligned} \tag{2.39}$$

with

$$\bar{c} = \frac{c-b}{c}, \quad \lambda = \pi \bar{E} / (2E_p). \tag{2.40}$$

Only the corresponding equations for the right bonded part of the actuator are given in Equations (2.38) and (2.39). For the current symmetric problem, these equations are sufficient for solving the problem since the shear and normal stresses in the left bonded part of the actuator can be directly determined from the symmetry. In these equations, y_{1j}^* is the coordinate of collocation point j in the first coordinate system (the left bonded part of the actuator), with

$$y_{1j}^* = \eta_j + 2 \frac{c+b}{c-b}. \tag{2.41}$$

The additional equation given by Equation (2.33) becomes

$$\sum_{i=0}^{N-2} d_i \left[\int_1^{\xi_1} \frac{[\sqrt{y_1^2 - 1} - y_1]^i}{\sqrt{y_1^2 - 1}} dy_1 + \int_{\xi_2}^{-1} \frac{[\sqrt{y_2^2 - 1} + y_2]^i}{\sqrt{y_1^2 - 1}} dy_2 \right] + 2\lambda \frac{b}{c} d_0 = \frac{2b}{\pi c} \tag{2.42}$$

where

$$\xi_1 = 2 \frac{\alpha_0}{\alpha} - 3, \quad \xi_2 = -\xi_1 = -2 \frac{\alpha_0}{\alpha} + 3, \quad \alpha = \frac{\bar{c}}{h}, \quad \alpha_0 = \frac{c}{h}. \tag{2.43}$$

The unknown coefficients d_i and e_i , which represents the interfacial stresses, can then be determined by using Equations (2.38), (2.39) and (2.42). In these equations, d_0 is related

to the axial force in the debonded part, $e_0 = 0$ and e_1 is related to the bending moment at the tip of the debonded part, i.e.

$$d_0 = \frac{T}{\pi h p \alpha}, \quad e_0 = 0, \quad e_1 = -\frac{4}{\pi^2} \frac{E_p I}{\bar{E} b^2 c} M_b^*. \quad (2.44)$$

In the numerical solution, $N - 2$ collocation points are used for each bonded part of the actuator, with $j = 2, 3, \dots, N - 1$, which provide $2N - 4$ equations. Combined with Equation (2.42), $2N - 3$ equations are obtained for $2N - 3$ unknowns $d_i, i = 1, 2, \dots, N - 2$; $e_i, i = 1, 2, \dots, N - 2$.

2.3 Results and Discussion

The electromechanical behaviour of the integrated actuator-host structure is dominated by the interfacial normal and shear stresses transferred from the actuator to the host medium. These stresses can be determined by solving Equations (2.38), (2.39) and (2.42). The numerical results of the interfacial stresses will be presented in this section to evaluate the effects of geometry, material mismatch and interface debonding. In the solution of the problem, based on careful evaluation of the convergence of Chebyshev polynomial expansion, 40 terms of Chebyshev polynomials are used in the calculation, which ensures that the current results considered are convergent. The force and deformation of the debonded part of the actuator are also discussed to study the effect of debonding upon the local response of the structure.

2.3.1 Comparison with FEM results

To verify the current actuator model, finite element analysis (FEA) is conducted to determine the stress distribution along the actuator-host interface for both perfectly bonded and partially debonded actuators. The results are then compared to that of the current model.

The commercially available software ANSYS is used in the simulation with the piezoelectric material and the elastic host medium being modelled by a coupled field element PLANE13 and a plane element PLANE182, respectively. The thickness of the piezoelectric sensor is 0.1mm and the half-length of the sensor is 0.5mm or 1.0mm for two different cases corresponding to $c/h=5$ and $c/h=10$, respectively. The length and thickness of the host structure are selected as 100 times of the thickness of the sensor to simulate the semi-infinite plane. After the convergence analysis, the typical element size for both the actuator and the host structure is chosen as 1/20 of the thickness of the actuator to ensure the accuracy of the simulation with around 4,000,000 elements. The material constants used are shown in Table 2.1 and 2.2 with Young's modulus of the host being adjusted so that $\lambda = 0.5$.

Table 2.1: Typical material properties of piezoelectric sensors.

Elastic stiffness parameters	c_{11}	c_{12}	c_{13}	c_{33}	c_{44}
($\times 10^{10} Pa$)	13.9	6.78	7.43	11.5	2.56
Piezoelectric constants	e_{31}	e_{33}	e_{15}		
(c / m^2)	-5.2	15.1	12.7		
Dielectric constants	ϵ_{11}	ϵ_{33}			
$\times 10^{-9} C / Vm$	6.45	5.62			

Table 2.2: Typical material properties of the host structure.

Young's modulus E	Poisson ratio ν
$5.27 \times 10^{10} Pa$	0.3

The interfacial stresses determined from the current model and from the FEA for a perfectly bonded actuator for $\lambda = 0.5$ and $c/h = 5.0$ are shown in Fig. 2.4. To illustrate the effect of bending deformation, the corresponding results with bending being ignored has also been included in the figure. The shear stresses determined from the current model and FEM show very good agreement, while the shear stresses from the model without bending effect and FEM show relative larger error. The resulting normal stresses along the interface from the current model and the FEA show a similar variation along the interface, which, however, cannot be captured when the bending effect is ignored since in this case zero interfacial normal stress is always predicted.

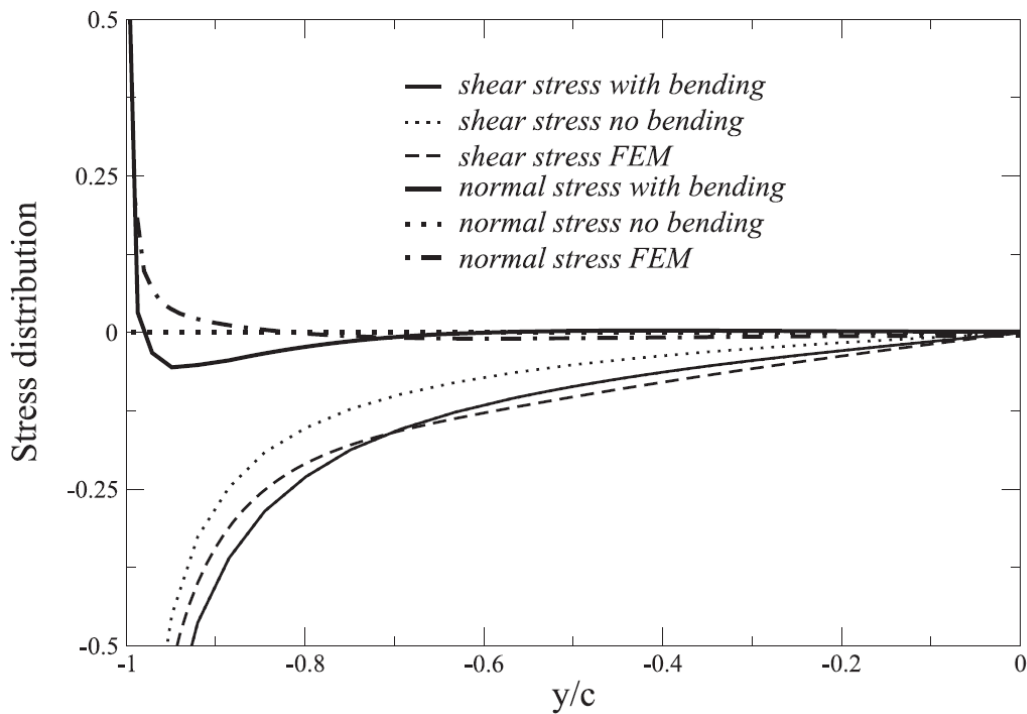


Fig. 2.4: Comparison with FEM results for a single actuator ($\lambda = 0.5$).

The corresponding results and comparison for a debonded actuator are shown in Fig. 2.5 for $\lambda = 0.5$, $c/h = 10.0$ and $b/c = 0.5$. Similarly, the shear stresses from the current model

and FEA show very good agreement. The current model can reasonably predict the variation of the interfacial normal stress, which cannot be predicted using a model with ignored bending effect, which predicts zero interfacial normal stress. There is a limited discrepancy for the stress distribution, especially the normal stress, near the tips of the actuator. This discrepancy is mainly caused by the singularity of the stress field at the tips.

2.3.2 Single actuator with bending effect

Let's consider first the electromechanical behaviour of a perfectly bonded piezoelectric layer. Obviously, the material combination or the stiffness ratio between the layer and the host medium will play a significant role in the load transfer. This effect can be described by a parameter $\lambda = \pi \bar{E} / (2E_p)$. Another important parameter affecting the behaviour of the layer is the length-to-thickness ratio $\nu = c/h$.

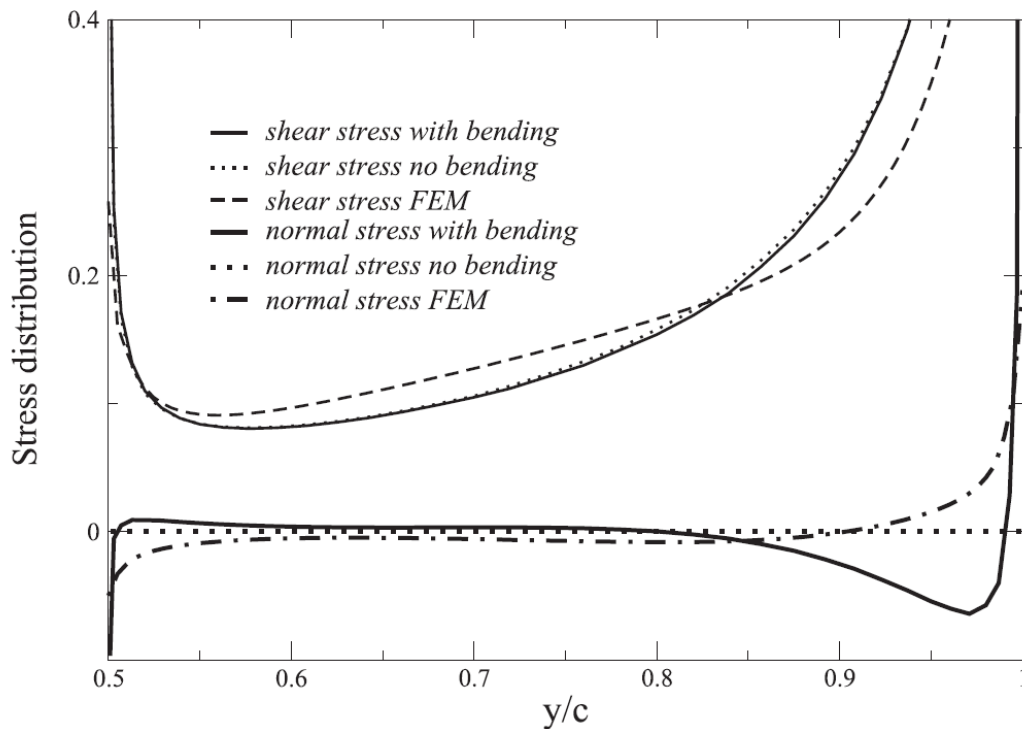


Fig. 2.5: Comparison with FEM results for a debonded actuator ($\lambda = 0.5$).

Carefully examining the governing equations of the problem indicates that the normalized interfacial shear stress and normal stress are governed by these two parameters (λ and ν). Table 2.1 and 2.2 (Pak, 1990) shows the typical property of piezo-ceramics and the host medium, with which the material combination gives that $\lambda = 1.0$. The typical thickness of commonly used piezoelectric thin-sheets is in the range of 0.1mm to 0.5mm. So for a layer of 10mm in length, the length-to-thickness ratio is $c/h = 10 - 50$. Based on these reference data, parameters λ and ν will be varied in the following discussion to evaluate the effects of the material property and the geometry of the structure.

The normalized interfacial shear stress τ^* and normal stress σ^* are important indicators of the actuation process. Comparing with previous actuator models where the bending effect is ignored, the level of the transverse normal stress σ represents the importance of the bending deformation. The results for shear and normal stress distributions along the interface for $\nu = c/h = 5.0$ for different λ values are shown in Fig. 2.6. The thicker curves represent the shear stress, and the thinner ones represent the normal stress. For stiff actuators, i.e. low λ values, the normal stress is quite significant. When the actuator becomes softer the effect of the normal stress is mostly near the actuator tips. The corresponding stress for the case where $\nu = c/h = 1.0$ is shown in Fig.2.7. Compared with Fig. 2.6 the increase in ν value shows more effect on the stress distribution for low λ values, but has limited influence on the stress for higher λ values, since the stress near the tips of a soft actuator will be insensitive to its length increase.

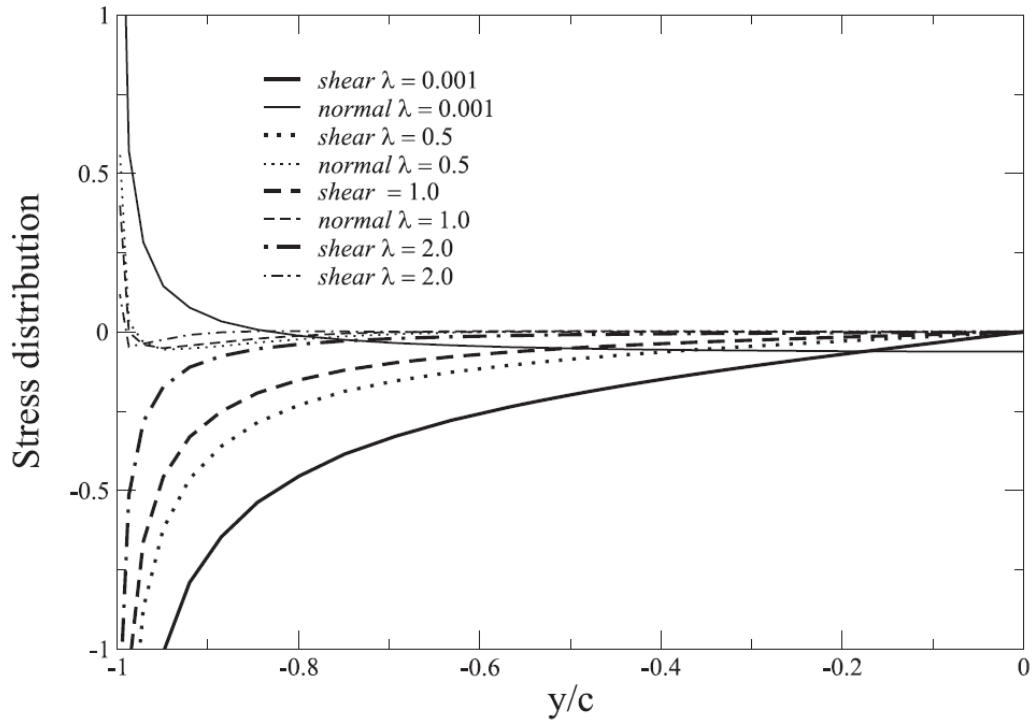


Fig. 2.6: Interfacial stress distribution of a single actuator ($c/h=5$)

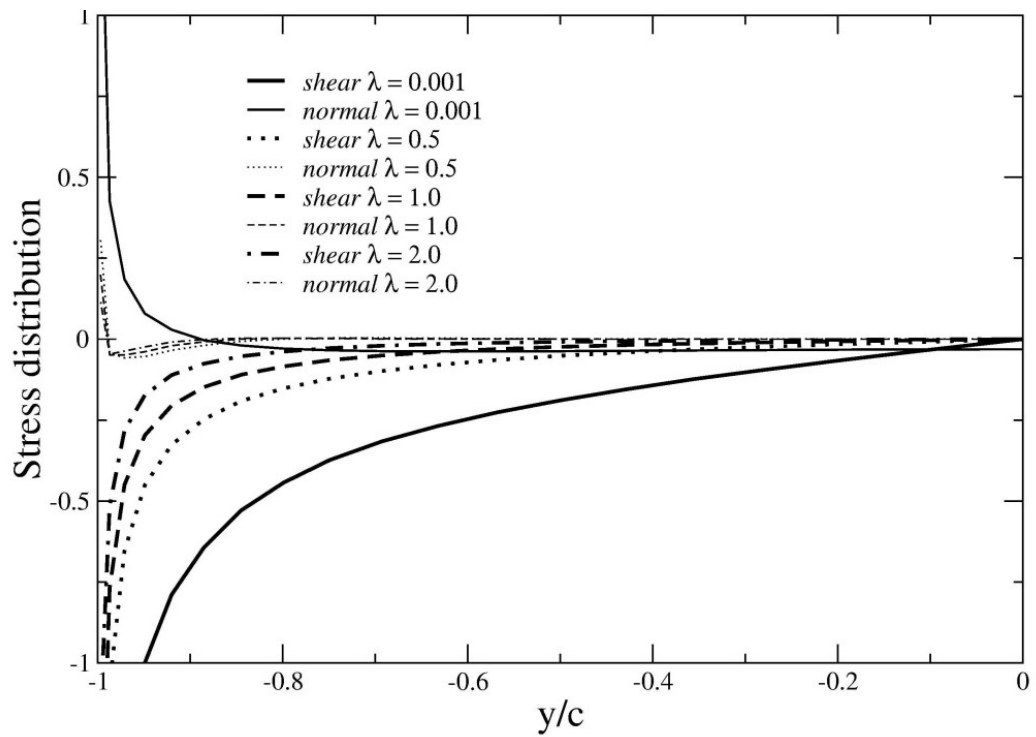


Fig. 2.7: Interfacial stress distribution of a single actuator ($c/h=10$)

2.3.3 Interacting actuators

If the debonded part of the actuator is removed, the two bonded parts of the actuator become two identical interacting actuators. Fig. 2.8 shows the shear and normal stress distributions of the right actuator along the interface for $\lambda = 0.5$ and $\nu = 10$ for different distances between the actuators, where c is the half length of the actuators and $d = b/h$ with $2b$ being the distance between the actuators. When the actuators are very close to each other the interaction results in asymmetric stress distribution for both τ and σ .

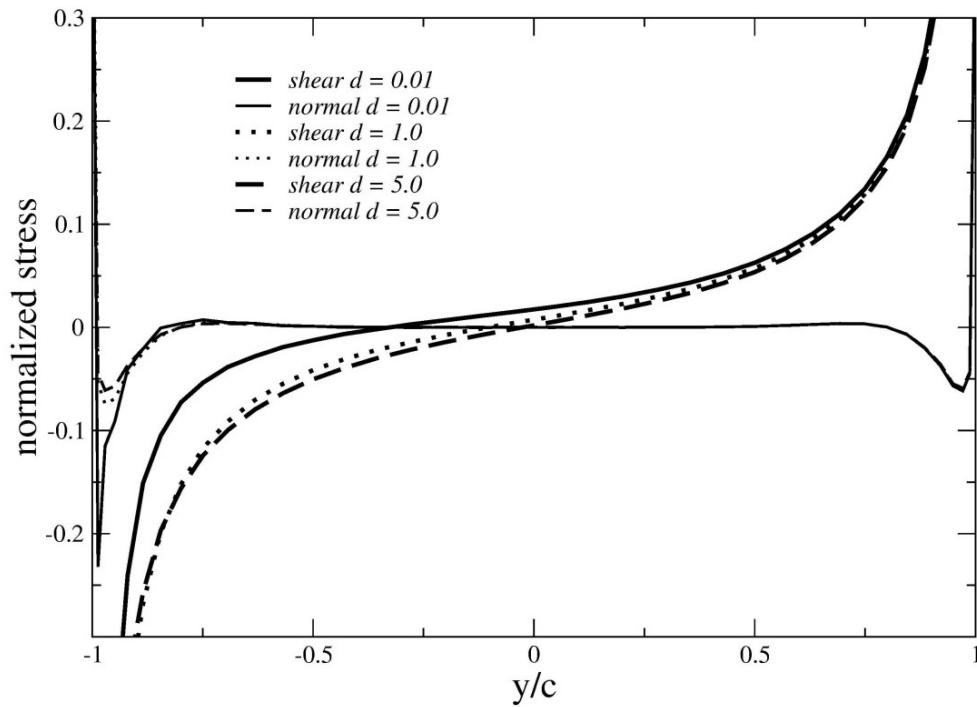


Fig. 2.8: Interfacial stress distribution of interacting actuators ($\lambda = 0.5, \nu = 10$).

The results of interacting actuators for $\lambda = 0.1$ are shown in Fig. 2.9. In this case the host medium is softer so the distributions of the stresses, both shear and normal, are less concentrated to the tips of the actuators. Significant asymmetry of shear stress distribution indicates the effect of interaction between the actuators. For both Fig. 2.8 and 2.9 the right tip of the actuator shown is almost unaffected, which corresponds to that of the single actuator.

The left tip, which is close to the other actuator, shows more significant shear and normal stresses because of the interaction effect.

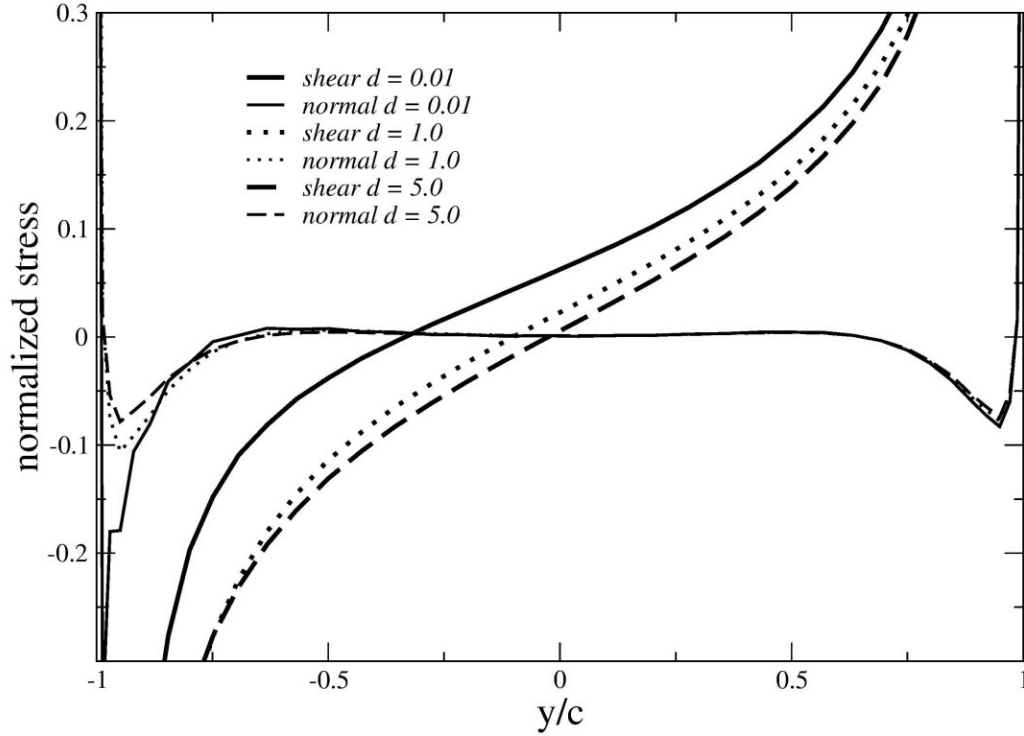


Fig. 2.9: Interfacial stress distribution of interacting actuators ($\lambda = 0.1, \nu = 10$).

2.3.4 Interfacial debonding

Interfacial debonding may occur because of the initial flaws at the interface or interfacial damage during service. The existence of such interfacial debonding will significantly alter the local stress distribution. Shear and normal stresses caused by an actuator partially debonded in $-b < y < b$ along the interface are shown in Fig. 2.10 and 2.11, respectively, for $\lambda = 0.5$. The results show that both the shear stress and the normal stress concentrate near the ends of the debonding part, particularly for larger debonding lengths. Fig. 2.10 also shows that the debonding mainly affect the stress distribution near the debonding area, and its effect on points away from debonding is insignificant, such as the points near the right tip of the

actuator as shown. Compared with shear stress, normal stress distribution is more affected by the debonding, as shown in Fig. 2.11.

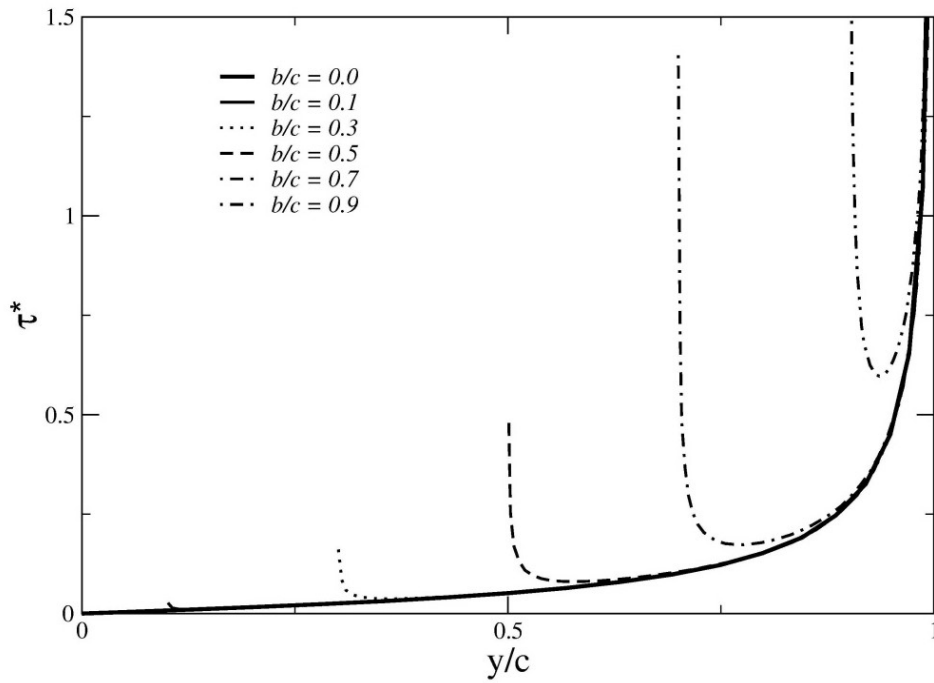


Fig. 2.10: Interfacial shear stress of debonded actuator ($\lambda = 0.5$)

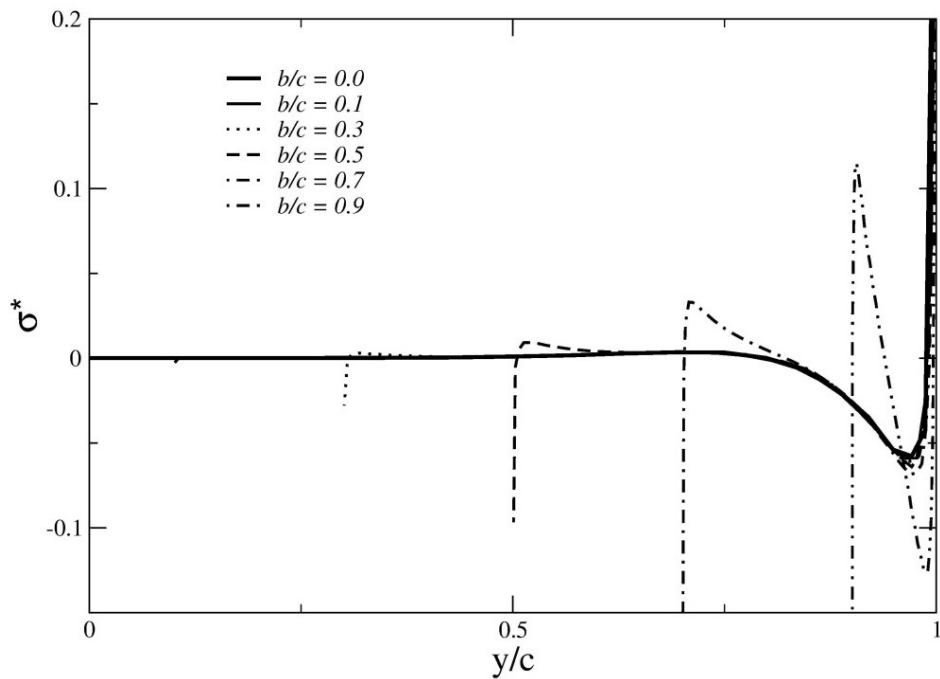


Fig. 2.11: Interfacial normal stress of debonded layer ($\lambda = 0.5$)

The debonded part of the actuator will not perform load transfer through interfacial stresses but the axial force T and bending moment M_b inside this part will affect the stress distribution and the load transfer of the system. The normalized axial force $T^* = T / (h\sigma_b)$ in the debonded part of the actuator is shown in Fig. 2.12 as a function of the length of the debonding b/c . The axial force is significantly affected by the material combination (λ). It should be mentioned that the debonding length b/c shows a very limited effect on the axial force until the debonding becomes rather long, approaching the tip of the actuator, even when the actuator is relatively stiff.

The normalized bending moment in the debonded part of the actuator is given in Fig. 2.13, which shows a significant increase with increasing debonding length. As expected, for a stiffer actuator, such as $\lambda = 0.1, 0.5$, the bending deformation is more significant than the case for a softer actuator. It is interesting to mention that if debonding is limited, then bending deformation, as represented by the bending moment, is insignificant in this case. The result indicates that the bending deformation will play an important role when debonding is the concern, but when no debonding occurs, the effect of bending of actuators is much less important.

Fig. 2.14 shows the normalized horizontal displacement of the end of the debonding part, $u^* = u_y / u_0$ with u_0 being the free horizontal displacement generated by the electric field at $y = b$ of the actuator when there is no restraint to the deformation of the actuator. Near linear relation between u^* and the debonding length is observed even for large debonding, indicating that the axial force in the debonded part is almost a constant with the increase of the length of the debonding, consistent with the results of the axial force shown in Fig. 2.12.

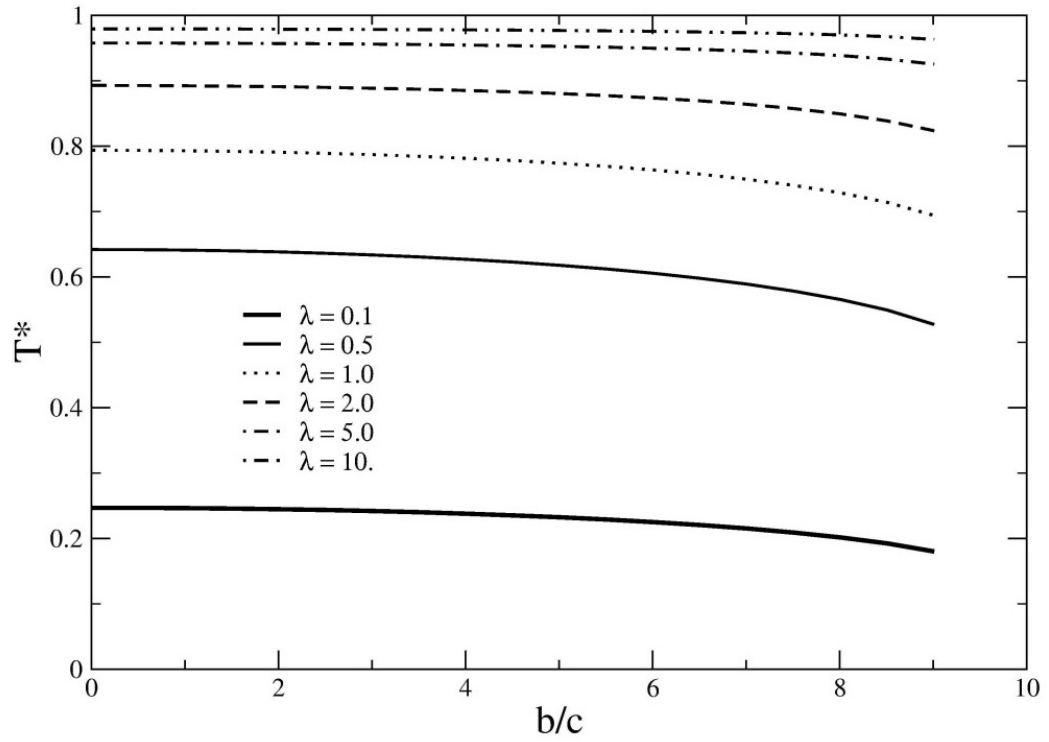


Fig. 2.12: Axial compressive force

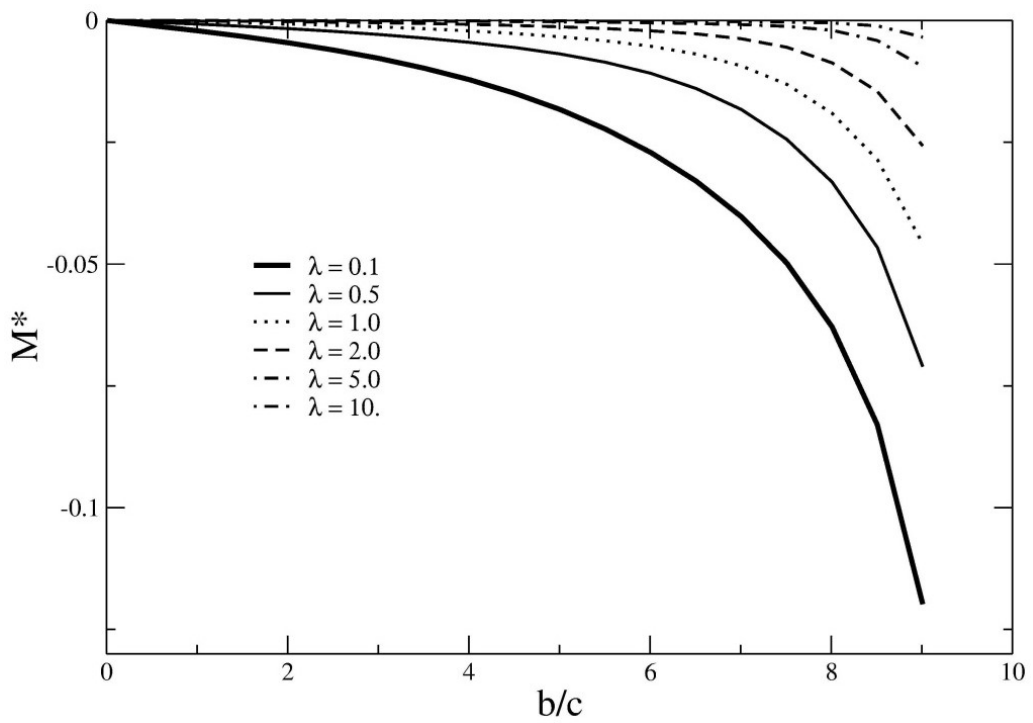


Fig. 2.13: Bending moment in the debonded part

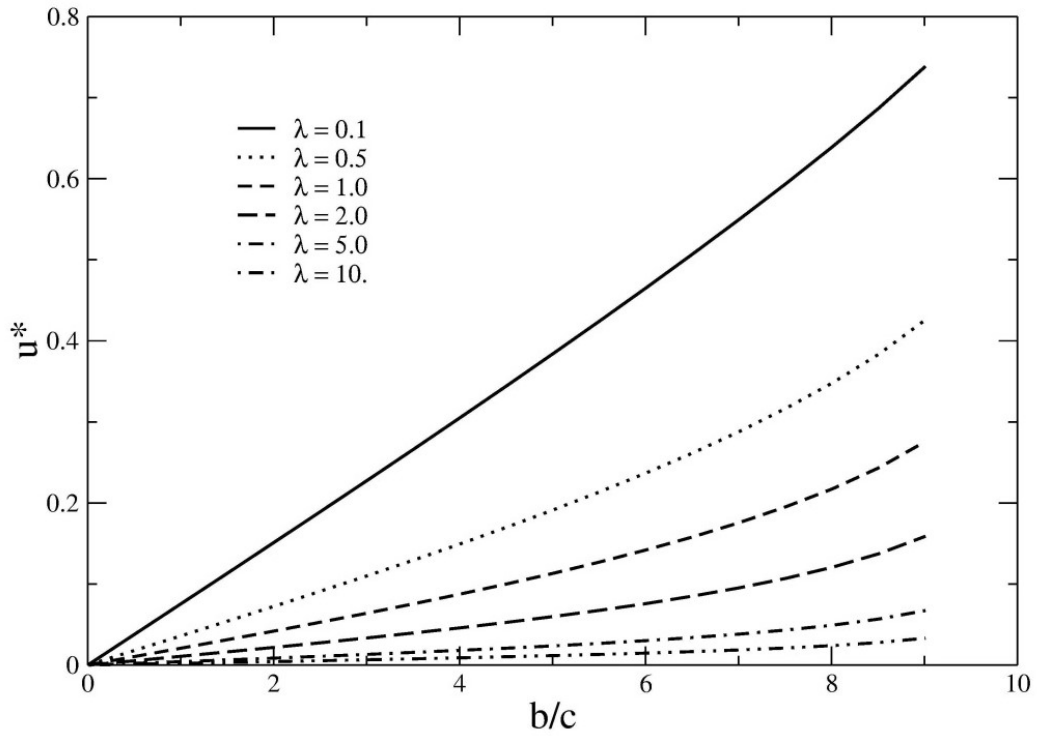


Fig. 2.14: Axial displacement of the end of the debonded part

2.4 Conclusions

This chapter provides a generalized model for surface bonded thin-sheet piezoelectric actuator, which contains both the axial and bending deformation. The formulation of the model is established and the solution of the resulting integral equations is presented using Chebyshev polynomials. Based on this model the electromechanical behaviour of a partially bonded piezoelectric actuator is studied. The model is used to evaluate the effects of the material property and the geometry on the load transfer from the actuator, through specific examples. The effects of debonding on the stress redistribution and load transfer in the integrated structure are studied. It is observed that the bending deformation may play a significant role in the electromechanical behaviour of this type of integrated systems, especially when debonding occurs.

Chapter 3: Dispersion characteristics of layered piezoelectric structures

This chapter presents a theoretical study of the coupled dynamic behaviour of layered piezoelectric structures, including the dispersion characteristics and wave propagation under in-plane mechanical loadings. Based on the results of the previous chapter, the piezoelectric layer is modelled as an electro-elastic film, which reduces the complex eigen-value problem into the non-trivial solution of binary quadratic equations. Typical numerical examples are given to illustrate the wave modes, wave propagation and the effects of the piezoelectricity, geometry and material properties. This chapter starts with a brief introduction to the dynamic behaviour of layered piezoelectric structures as section 3.1, followed by the formulation of the problem (section 3.2), comparison with exact dispersion solutions (section 3.3) and wave propagation under a harmonic loading (section 3.4). Sections 3.5-3.7 are the numerical results, discussion and conclusions, respectively. The results in this chapter will be used in Chapter 4 to guide the modelling and simulation of the dynamic behaviour of piezoelectric sensors.

3.1 Introductions

When piezoelectric sensors are used for SHM, wave guides are formed by the layered piezoelectric structures. The fundamental issue for waves in such structures is their dispersion characteristics (eigen-value solution) and the steady state response (general solution) of the piezoelectric structure. The relation between the eigen-value solution and the

general solution can be understood by referring to the difference between free vibration and forced vibration.

Section 1.2.2 has summarized the methods for dispersion characteristics of elastic wave propagation in layered piezoelectric structures, including exact solutions and approximate solutions. The exact dispersion equations of wave propagation in layered piezoelectric structures have been studied with the main focus on Lamb wave and surface wave (Datta et al., 1988; Nayfeh, 1995). Lamb wave propagation in a dielectric half-space overlaid by a thin piezoelectric layer has been studied using a simplified numerical solution of the dispersion curve by segmenting the phase velocity spectrum into different ranges (Jin et al., 2002). The dispersion characteristics of surface waves in a piezoelectric layer bonded to a piezo-magnetic semi-infinite host medium (Pang et al., 2008) and the wave propagation in double-layered piezoelectric plates (Cheng and Sun, 1975) have also been studied.

These works provided useful information about the characteristics of elastic waves in layered structures but were mostly from complicated numerical solutions. For cases where the layers are very thin, the approximate dispersion relation for wave in such thin layers bonded to semi-infinite structures have been studied by modelling the layer as a thin plate (Achenbach and Keshava, 1967; Tiersten, 1969), or by expanding the displacements and stresses of the layer into Taylor series along thickness of the layer (Vinh and Linh, 2012; Pham and Vu, 2014). These two models provided good approximate solutions but can only determine the surface wave mode.

The objective of this chapter is to develop an analytical solution for approximate yet accurate dispersion equation of wave propagation in the layered piezoelectric structures. The current model is simple yet captures the two lowest modes of the wave propagation. To

validate the current model, the dispersion curves of the wave are determined and compared with exact models. Two major wave modes are discussed in detail, and the influence of the material and geometric properties of the piezoelectric layer is studied. Then, the dynamic behaviour of the structure under a longitudinal harmonic loading is further studied to evaluate the dynamic load transfer from the substrate to the surface-bonded layer.

3.2 Formulation of the problem

The problem envisaged is the wave propagation in a layered piezoelectric structure, as shown in Fig. 3.1, which consists of a thin piezoelectric layer with the uniform thickness h , as the sensors, and a homogeneous and isotropic elastic insulator under plane strain condition. It is assumed that the poling direction of the piezoelectric layer is along the z -axis, perpendicular to the x - y plane. Since the thickness of the piezoelectric layer is very thin, much smaller than that of the substrate, the substrate can be treated as a half-space (Qian and Hirose, 2012). Harmonic in-plane waves of frequency ω will be considered.

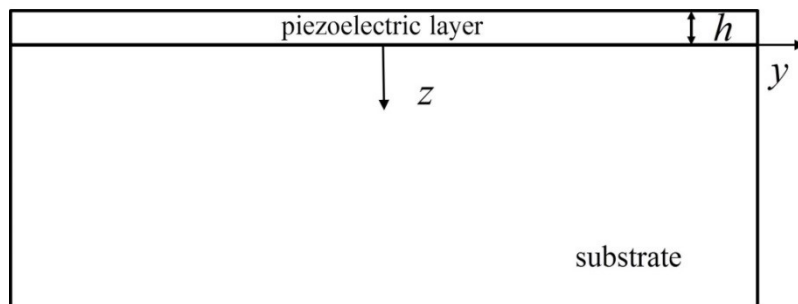


Fig. 3.1: A piezoelectric layer surface-bonded to an elastic half-space substrate

In this case, the field variables, displacement, stress and strain, are all in the form of

$$\bar{A}(y, z, t) = A(y, z)e^{-i\omega t}. \quad (3.1)$$

For convenience, $e^{-i\omega t}$ term will be omitted in the following discussion and only the magnitude $A(y, z)$ will be considered.

3.2.1 Modelling of the piezoelectric layer

For a thin piezoelectric layer bonded to an elastic half-space, its axial stiffness along the layer will play a more important role than its flexural stiffness. As a result, the piezoelectric layer can be modelled as a thin film with no bending stiffness (Yu and Wang, 2016). The interfacial shear stress (τ) transferred between the piezoelectric layer and the substrate can be treated as a distributed body force along the layer (Wang and Meguid, 2000). Therefore, the layer can be modelled as an electro-elastic thin film subjected to a distributed axial body force τ/h and normal force $\sigma_z = \sigma$, as shown in Fig. 3.2.

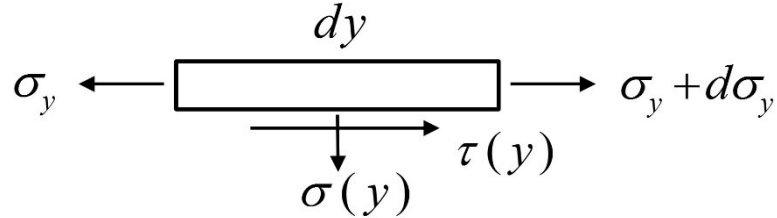


Fig. 3.2: Stress analysis of the layer

The equation of motion of the layer can be expressed as

$$\frac{d\sigma_y}{dy} + \frac{\tau(y)}{h} + \rho\omega^2 u_y = 0 \quad (3.2)$$

$$\sigma_z + \rho h\omega^2 u_z = 0 \quad (3.3)$$

where σ_y is the axial stress, u_y and u_z are the axial and transverse displacements, and ρ is the mass density.

The constitutive relation of the piezoelectric layer under plane strain and open-loop conditions can be described as shown in Appendix B:

$$\sigma_y = E_{eff} \frac{\partial u_y}{\partial y}, \quad E_{eff} = E + \frac{e^2}{\lambda} \quad (3.4)$$

with $E = c_{11} - \frac{c_{13}^2}{c_{33}}$, $e = e_{13} - e_{33} \frac{c_{13}}{c_{33}}$, $\lambda = \lambda_{33} + \frac{e_{33}^2}{c_{33}}$. c_{ij} are the stiffness parameters, e_{ij} are the piezoelectric constants, and λ_{ij} are the dielectric constants.

The piezoelectric layer can be treated as a waveguide. For a free wave propagates along the positive y-axis with a velocity c , the displacement can be described as

$$u_y = \bar{u}_y e^{iky}, \quad k > 0 \quad (3.5)$$

where $k = \omega / c$ is the wave number and \bar{u}_y is the amplitude of the displacement.

Substituting Equations (3.4) and (3.5) into (3.2), the interfacial shear stress can then be related to the displacement u_y as

$$\tau = (k^2 - \frac{\omega^2}{c_s^2}) E_{eff} h u_y \quad (3.6)$$

Where $c_s = \sqrt{E_{eff} / \rho}$. And the interfacial normal stress can be determined as

$$\sigma_z = -\rho h \omega^2 u_z. \quad (3.7)$$

3.2.2 Wave in the substrate

The wave propagation in the substrate is governed by equations of motion given by Achenbach (1973, P59),

$$\mu_s u_{\alpha,\beta\beta} + (\lambda_s + \mu_s) u_{\beta,\beta\alpha} = \rho_s \partial^2 u_\alpha / \partial t^2, \quad \alpha, \beta = y, z \quad (3.8)$$

where μ_s, λ_s are the Lamé's elastic constants of the substrate, and ρ_s is the mass density of the substrate.

The general solution of displacements of a surface wave of velocity c in the substrate can be written in the following form

$$u_y^s = (A_1 e^{-b_1 z} + A_2 e^{-b_2 z}) e^{iky} \quad (3.9)$$

$$u_z^s = \left(-\frac{b_1}{ik} A_1 e^{-b_1 z} + \frac{ik}{b_2} A_2 e^{-b_2 z} \right) e^{iky} \quad (3.10)$$

where

$$b_1 = k(1 - c^2 / c_L^2)^{1/2}, \quad b_2 = k(1 - c^2 / c_T^2)^{1/2}, \quad (3.11)$$

in which, c_L and c_T denote the velocities of longitudinal and transverse waves in the substrate, respectively, with $c_L = \sqrt{(\lambda_s + 2\mu_s) / \rho_s}$ and $c_T = \sqrt{\mu_s / \rho_s}$. A_1 and A_2 are two unknown parameters to be determined by the boundary conditions.

The stresses in the substrate can then be determined as

$$\sigma_z^s = E^* (\varepsilon_z + \nu^* \varepsilon_y) \quad (3.12)$$

$$\sigma_{yz}^s = \mu_s \gamma_{yz}^s \quad (3.13)$$

where

$$\varepsilon_y^s = \frac{\partial u_y^s}{\partial y} = ik(A_1 + A_2) e^{iky} \quad (3.14)$$

$$\varepsilon_z^s = \frac{\partial u_z^s}{\partial z} = \left(\frac{b_1^2}{ik} A_1 - ik A_2 \right) e^{iky} \quad (3.15)$$

$$\gamma_{yz}^s = \frac{\partial u_y^s}{\partial z} + \frac{\partial u_z^s}{\partial y} = (A_1 b_1 e^{-b_1 z} + A_2 b_2 e^{-b_2 z}) e^{iky} + ik \left(-\frac{b_1}{ik} A_1 e^{-b_1 z} + \frac{ik}{b_2} A_2 e^{-b_2 z} \right) e^{iky} \quad (3.16)$$

and $E^* = \lambda_s + 2\mu_s$, $\nu^* = \lambda_s / (\lambda_s + 2\mu_s)$.

The shear and normal stress at the interface of the substrate are

$$\tau_{yz}^s \Big|_{z=0} = -\mu_s (2A_1 b_1 + A_2 b_2 + \frac{k^2}{b_2} A_2) e^{iky} \quad (3.17)$$

$$\sigma_z^s \Big|_{z=0} = E^* \left[\left(\frac{b_1^2}{ik} A_1 - ik A_2 \right) + \nu^* ik (A_1 + A_2) \right] e^{iky} . \quad (3.18)$$

3.2.3 Dispersion equation

The continuity of displacements and stresses at the interface $z = 0$ are

$$u_y^s \Big|_{z=0} = (A_1 + A_2) e^{iky} \quad (3.19)$$

$$u_z^s \Big|_{z=0} = \left(-\frac{b_1}{ik} A_1 + \frac{ik}{b_2} A_2 \right) e^{iky} \quad (3.20)$$

$$\tau_{yz}^s \Big|_{z=0} = \tau, \quad \sigma_z^s \Big|_{z=0} = \sigma_z . \quad (3.21)$$

By substituting (3.6), (3.7), (3.17), (3.18), (3.19) and (3.20) into (3.21), the boundary conditions can be expressed as

$$\left[2\mu b_1 + \left(k^2 - \frac{\omega^2}{c_s^2} \right) E_{eff} h \right] A_1 + \left[\mu \left(b_2 + \frac{k^2}{b_2} \right) + \left(k^2 - \frac{\omega^2}{c_s^2} \right) E_{eff} h \right] A_2 = 0 \quad (3.22)$$

$$\left[\frac{b_1^2}{ik} + \nu^* ik - \frac{\rho h \omega^2}{E^*} \left(\frac{b_1}{ik} \right) \right] A_1 + \left[-ik(1 - \nu^*) + \frac{\rho h \omega^2}{E^*} \left(\frac{ik}{b_2} \right) \right] A_2 = 0 . \quad (3.23)$$

Equations (3.22) and (3.23) can be reorganized in matrix form. The two equations for A_1 and A_2 have a non-zero solution when and only when the determinant of the coefficient matrix vanishes. The dispersion equation can then be obtained from the condition that the coefficient matrix is singular, i.e.

$$\begin{vmatrix} 2\mu b_1 + (k^2 - \frac{\omega^2}{c_s^2})E_{eff}h & \mu(b_2 + \frac{k^2}{b_2}) + (k^2 - \frac{\omega^2}{c_s^2})E_{eff}h \\ \frac{b_1^2}{k} - \nu^*k - \frac{\rho h \omega^2}{E^*}(\frac{b_1}{k}) & k(1 - \nu^*) - \frac{\rho h \omega^2}{E^*}(\frac{k}{b_2}) \end{vmatrix} = 0 \quad (3.24)$$

3.2.4 Comparison with Rayleigh wave

If piezoelectric layers disappear ($E_{eff} = 0, \rho = 0$), the problem is degenerated into wave propagation along the free surface of an elastic half-space, which is Rayleigh wave. In this case, Equation (3.24) can be simplified to

$$\begin{vmatrix} 2\mu_s b_1 & \mu_s(b_2 + \frac{k^2}{b_2}) \\ \frac{b_1^2}{k} - \nu^*k & k(1 - \nu^*) \end{vmatrix} = 0, \quad (3.25)$$

which can be expressed as

$$2(1 - \frac{c^2}{c_L^2})^{1/2}(1 - \frac{c^2}{c_T^2})^{1/2} - (2 - \frac{c^2}{c_T^2})(1 - \frac{c^2}{c_L^2} \frac{1-2\nu}{1-\nu}) = 0. \quad (3.26)$$

Substituting the ratio of the transverse and longitudinal velocities, $c_L^2 / c_T^2 = 2(1 - \nu) / (1 - 2\nu)$,

into Equation (3.26), the dispersion equation can be simplified as

$$4(1 - \frac{c^2}{c_L^2})^{1/2}(1 - \frac{c^2}{c_T^2})^{1/2} - (2 - \frac{c^2}{c_T^2})^2 = 0 \quad (3.27)$$

which is exactly the dispersion equation of Rayleigh wave (Achenbach, 1973).

3.3 Comparison with exact solution

3.3.1 Governing equations

The governing equations of piezoelectric materials are determined and given in Appendix A. For the current problem, the thin-sheet piezoelectric layer will operate in an open-loop mode without external charge supplied to it. Therefore, the electric displacement in z -direction in the piezoelectric layer will be zero, i.e. $D_z = 0$. And also considering the plane strain condition (y - z plane), the governing equations can be reduced to

$$\begin{aligned} c_{11}^* \frac{\partial^2 u_y}{\partial y^2} + c_{44}^* \frac{\partial^2 u_y}{\partial z^2} + (c_{13}^* + c_{44}^*) \frac{\partial^2 u_z}{\partial y \partial z} &= -\rho \omega^2 u_y \\ c_{44}^* \frac{\partial^2 u_z}{\partial y^2} + c_{33}^* \frac{\partial^2 u_z}{\partial z^2} + (c_{13}^* + c_{44}^*) \frac{\partial^2 u_y}{\partial y \partial z} &= -\rho \omega^2 u_z \end{aligned} \quad (3.28)$$

with

$$\begin{aligned} c_{11}^* &= c_{11} + e_{31}^2 / \lambda_{33} \\ c_{13}^* &= c_{13} + e_{31} e_{33} / \lambda_{33} \\ c_{33}^* &= c_{33} + e_{33}^2 / \lambda_{33} \\ c_{44}^* &= c_{44} + e_{15}^2 / \lambda_{11} \end{aligned}$$

In these equations, u_y and u_z are the displacements in y and z -direction, respectively. c_{ij} are the stiffness parameters for a constant electric potential, e_{ij} are the piezoelectric constants, λ_{ij} are the dielectric constants for zero strains, and ρ is the mass density.

The governing equations for the elastic substrate can be obtained by setting the piezoelectric, dielectric constants in Equation (3.28) to zero and $c_{11} = c_{33} = \lambda_s + 2\mu_s$, $c_{12} = c_{13} = \lambda_s$, $c_{44} = \mu_s$, giving

$$\begin{aligned}
c_T^2 \left(\frac{\partial^2 u_y}{\partial y^2} + \frac{\partial^2 u_y}{\partial z^2} \right) + (c_L^2 - c_T^2) \left(\frac{\partial^2 u_y}{\partial y^2} + \frac{\partial^2 u_z}{\partial y \partial z} \right) &= -\omega^2 u_y, \\
c_T^2 \left(\frac{\partial^2 u_z}{\partial y^2} + \frac{\partial^2 u_z}{\partial z^2} \right) + (c_L^2 - c_T^2) \left(\frac{\partial^2 u_z}{\partial z^2} + \frac{\partial^2 u_y}{\partial y \partial z} \right) &= -\omega^2 u_z
\end{aligned} \tag{3.29}$$

where c_L and c_T denote the velocities of longitudinal and transverse waves in the substrate, respectively, with $c_L = \sqrt{(\lambda_s + 2\mu_s) / \rho_s}$ and $c_T = \sqrt{\mu_s / \rho_s}$, in which μ_s, λ_s are the Lamé's elastic constants, and ρ_s is the mass density of the substrate. Equation (3.29) is the same as the governing equation of elastic structure obtained in (Achenbach and Keshava, 1967).

3.3.2 Wave motion equations

Consider free wave propagating in y direction in the piezoelectric layer, which can be expressed in the form (Achenbach, 1973)

$$\begin{aligned}
u_y &= A e^{-az} e^{ik(y-ct)} \\
u_z &= B e^{-az} e^{ik(y-ct)},
\end{aligned} \tag{3.30}$$

where k is the wave number, c is the phase velocity with $c = \omega / k$, A and B are unknown constants, a is a parameter to be determined.

In the substrate,

$$\begin{aligned}
u_y^s &= A^s e^{-bz} e^{ik(y-ct)} \\
u_z^s &= B^s e^{-bz} e^{ik(y-ct)},
\end{aligned} \tag{3.31}$$

where A^s and B^s are unknown constants, b is a parameter to be determined. The real part of a and b is supposed to be positive, so that the displacements decrease with increasing y and tend to zero as y increases beyond bounds.

Substituting Equation (3.30) into Equation (3.28) yields two homogeneous equations for constants A and B

$$\begin{aligned} (c_{44}^*a^2 - c_{11}^*k^2 + \rho k^2c^2)A - i(c_{13}^* + c_{44}^*)akB &= 0 \\ -i(c_{13}^* + c_{44}^*)akA + (c_{33}^*a^2 - c_{44}^*k^2 + \rho k^2c^2)B &= 0 \end{aligned} \quad (3.32)$$

A nontrivial solution of this system of equations exists if and only if the determinant of the coefficients vanishes, which leads to the following eigenequation

$$(c_{44}^*a^2 - c_{11}^*k^2 + \rho k^2c^2)(c_{33}^*a^2 - c_{44}^*k^2 + \rho k^2c^2) + (c_{13}^* + c_{44}^*)^2 k^2a^2 = 0 \quad (3.33)$$

The four roots of Equation (3.33) are denoted as a_i ($i = 1, 2, 3, 4$). Therefore, the general solution of wave propagation in the piezoelectric layer can be expressed in the form

$$\begin{aligned} u_y &= \sum_{i=1}^4 A_i e^{-a_i z} e^{ik(y-ct)} \\ u_z &= \sum_{i=1}^4 \alpha_i A_i e^{-a_i z} e^{ik(y-ct)} \end{aligned} \quad (3.34)$$

where A_i ($i = 1, 2, 3, 4$) are unknown constants corresponding to a_i ($i = 1, 2, 3, 4$) and

$$\alpha_i = (B/A)_i, \quad (i = 1, 2, 3, 4) \quad (3.35)$$

In the substrate, by substituting Equation (3.31) into Equation (3.29), two homogenous equations for A^s and B^s can be obtained as

$$\begin{aligned} [c_T^2 b^2 + k^2(c^2 - c_L^2)]A^s - ikb(c_L^2 - c_T^2)B^s &= 0 \\ -ikb(c_L^2 - c_T^2)A^s + [c_L^2 b^2 + k^2(c^2 - c_T^2)]B^s &= 0 \end{aligned} \quad (3.36)$$

A nontrivial solution of this system of equations exists if and only if the determinant of the coefficients vanishes, and parameter b can be obtained as

$$b_1 = k(1 - c^2/c_L^2)^{1/2}, \quad b_2 = k(1 - c^2/c_T^2)^{1/2} \quad (3.37)$$

Correspondingly, the general solution of the displacement equations of motion in the elastic substrate can be written in the form

$$\begin{aligned}
u_y^s &= (A_1 e^{-b_1 z} + A_2 e^{-b_2 z}) e^{iky} \\
u_z^s &= \left(-\frac{b_1}{ik} A_1 e^{-b_1 z} + \frac{ik}{b_2} A_2 e^{-b_2 z}\right) e^{iky}
\end{aligned} \tag{3.38}$$

3.3.3 Exact dispersion equations

The exact dispersion equations will be obtained here for comparison purpose.

The top surface of the piezoelectric layer is traction free, and the displacements and stresses along the interface between the piezoelectric layer and the substrate are continuing, so the boundary conditions are as follows,

At $z = -h$

$$\sigma_{zz} = \tau_{yz} = 0 \tag{3.39}$$

At $z = 0$

$$\begin{aligned}
u_y^s - u_y &= 0, \quad u_z^s - u_z = 0, \\
\sigma_{zz}^s - \sigma_{zz} &= 0, \quad \tau_{yz}^s - \tau_{yz} = 0.
\end{aligned} \tag{3.40}$$

The general solutions given by Equations (3.34) and (3.38) are required satisfying the boundary conditions, and the resulting equations are

$$\sum_{i=1}^4 (ikc_{13}^* - a_i \alpha_i c_{33}^*) A_i e^{a_i h} = 0 \tag{3.41}$$

$$\sum_{i=1}^4 c_{44}^* (ik\alpha_i - a_i) A_i e^{a_i h} = 0 \tag{3.42}$$

$$A_1^s + A_2^s - \sum_{i=1}^4 A_i = 0 \tag{3.43}$$

$$-\frac{b_1}{ik} A_1^s + \frac{ik}{b_2} A_2^s - \sum_{i=1}^4 \alpha_i A_i = 0 \tag{3.44}$$

$$(\lambda_s + 2\mu_s) \left[\left(\frac{b_1^2}{ik} A_1^s - ikA_2^s \right) + \frac{\lambda_s}{\lambda_s + 2\mu_s} ik(A_1^s + A_2^s) \right] - \sum_{i=1}^4 (ikc_{13}^* - a_i \alpha_i c_{33}^*) A_i = 0 \quad (3.45)$$

$$-\mu_s \left(2A_1^s b_1 + A_2^s b_2 + \frac{k^2}{b_2} A_2^s \right) - \sum_{i=1}^4 c_{44}^* (ik\alpha_i - a_i) A_i = 0. \quad (3.46)$$

Equations (3.41)-(3.46) are a system of 6 homogeneous equations for A_1^s, A_2^s and $A_i (i=1,2,3,4)$. The dispersion equation can be obtained from the condition that the coefficient matrix $[K_{jk}] (j,k=1,2, \dots, 6)$ of the system of equations is singular, or equivalently

$$|K_{jk}|_{6 \times 6} = 0 \quad (3.47)$$

which is the exact dispersion equation of the problem, i.e. for a given value of wave number k , the phase velocity c can be solved through Equation (3.47).

3.4 Wave propagation under a harmonic loading

The steady state response of the structure under an oblique incident harmonic wave will be studied. The displacement wave in the layer is described by Equation (3.6) and (3.7). By using the following spatial Fourier transform,

$$\begin{aligned} \bar{f}(s) &= \frac{1}{2\pi} \int_{-\infty}^{\infty} f(y) e^{isy} dy, \\ f(y) &= \int_{-\infty}^{\infty} \bar{f}(s) e^{-isy} ds \end{aligned} \quad (3.48)$$

the displacement field in the layer can be expressed in terms of the unknown interfacial shear and normal stress as

$$\begin{cases} \bar{u}_y = \frac{\bar{\tau}}{(s^2 - \omega^2 / c_p^2) E_p h} \\ \bar{u}_z = \frac{\bar{\sigma}_z}{-\rho h \omega^2} \end{cases} \quad (3.49)$$

The substrate is subjected to a harmonic incident wave and interfacial surface stresses, as shown in configuration (a) of Fig. 3.3. The incident wave will be reflected and the surface stresses will generate a dynamic field in the substrate. Therefore, the wave field inside the substrate can be expressed by superimposing the configuration (b) and (c),

$$\begin{cases} u_y^s = u_y^I + u_y^c \\ u_z^s = u_z^I + u_z^c \end{cases} \quad (3.50).$$

where the variables with superscript s, I and c represent the field in the substrate, configuration (b) and (c), respectively. In particular, u_y^I and u_z^I are the real displacement in configuration (b), i.e. the superposition of the incident wave and the reflected wave.

In Fig. 3.3(b), the displacement along the interfacial surface can be obtained as

$$\begin{cases} u_y^I|_{z=0} = A_y^I e^{ik_I y} \\ u_z^I|_{z=0} = A_z^I e^{ik_I y} \end{cases} \quad (3.51),$$

where A_y^I , A_z^I and k_I are functions of the amplitude, angle and wave number of the incident wave, given in Appendix B.

In Fig. 3.3(c), the dynamic plane strain displacement field in the homogeneous isotropic elastic host medium is governed by (Achenbach, 1973),

$$u_y^c = \frac{\partial \phi}{\partial y} + \frac{\partial \psi}{\partial z}, \quad u_z^c = \frac{\partial \phi}{\partial z} - \frac{\partial \psi}{\partial y} \quad (3.52)$$

where ϕ and ψ are two displacement potentials which satisfy

$$(\nabla^2 + k_L^2)\phi = 0, \quad (\nabla^2 + k_T^2)\psi = 0, \quad (3.53)$$

with

$$\nabla^2 = \partial^2 / \partial y^2 + \partial^2 / \partial z^2$$

$$k_L = \omega / c_L, \quad k_T = \omega / c_T$$

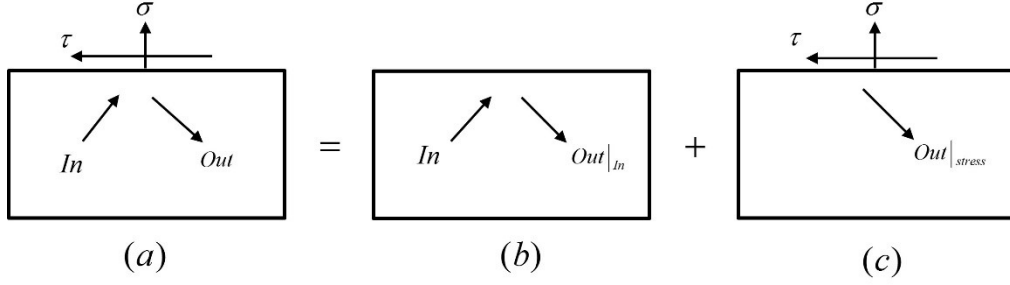


Fig. 3.3: The substrate subjected to a harmonic incident wave and interfacial surface stresses

The general solution of Equation (3.53) can be determined by using the Fourier transform defined by Equation (3.48), which can be expressed as

$$\bar{\phi}(s, z) = A(s)e^{\alpha z}, \quad \bar{\psi}(s, z) = B(s)e^{\beta z} \quad (3.54)$$

where $A(s)$ and $B(s)$ are two unknown functions of s with

$$\alpha = \begin{cases} \sqrt{s^2 - k_L^2} & |s| > k_L \\ -i\sqrt{k_L^2 - s^2} & |s| < k_L \end{cases}, \quad \beta = \begin{cases} \sqrt{s^2 - k_T^2} & |s| > k_T \\ -i\sqrt{k_T^2 - s^2} & |s| < k_T \end{cases} \quad (3.55)$$

which ensure that the induced stress field satisfies the radiation condition of the problem at infinity.

The outgoing wave in the substrate should satisfy the following boundary conditions along the surface,

$$\sigma_{yz}^c = \tau, \quad \sigma_z^c = \sigma \quad \text{at } z = 0$$

Then the unknown parameters $A(s)$ and $B(s)$ can be determined as

$$\begin{cases} A(s) = \frac{1}{\mu_s \Delta} [2is\beta\tau - (2s^2 - k_T^2)\sigma] \\ B(s) = \frac{1}{\mu_s \Delta} [-(2s^2 - k_T^2)\tau - 2is\alpha\sigma] \end{cases} \quad (3.56)$$

where $\Delta = (2s^2 - k^2)^2 - 4s^2\alpha\beta$.

From Equation (3.52), the Fourier transform of the displacement field components can be determined as

$$\begin{cases} \bar{u}_y^c = -isA(s)e^{\alpha z} + \beta B(s)e^{\beta z} \\ \bar{u}_z^c = \alpha A(s)e^{\alpha z} + isB(s)e^{\beta z} \end{cases} \quad (3.57)$$

and the Fourier transform of the dynamic stress field components caused by the surface stresses can be obtained as

$$\begin{cases} \bar{\sigma}_y^c = \mu_s [-(k_T^2 + 2\alpha^2)A(s)e^{\alpha z} - 2is\beta B(s)e^{\beta z}] \\ \bar{\sigma}_z^c = \mu_s [(2s^2 - k_T^2)A(s)e^{\alpha z} + 2is\beta B(s)e^{\beta z}] \\ \bar{\sigma}_{yz}^c = \mu_s [-2is\alpha A(s)e^{\alpha z} + (2s^2 - k_T^2)B(s)e^{\beta z}] \end{cases} \quad (3.58)$$

If the piezoelectric layer is perfectly bonded to the substrate, the displacement should be continuous at the upper surface of the substrate and the lower surface of the sensor,

$$\begin{cases} \bar{u}_y = \bar{u}_y^I + \bar{u}_y^c \\ \bar{u}_z = \bar{u}_z^I + \bar{u}_z^c \end{cases} \quad (3.59)$$

By substituting Equation (3.49) and (3.57) into Equation (3.59), the Fourier transform of the interfacial shear and normal stress can be determined as

$$\begin{cases} \bar{\tau} = \frac{m_{22}(s)\bar{u}_y^I - m_{12}(s)\bar{u}_z^I}{m_{11}(s)m_{22}(s) - m_{12}(s)m_{21}(s)} \\ \bar{\sigma} = \frac{m_{11}(s)\bar{u}_z^I - m_{21}(s)\bar{u}_y^I}{m_{11}(s)m_{22}(s) - m_{12}(s)m_{21}(s)} \end{cases} \quad (3.60)$$

with

$$\begin{aligned}
m_{11}(s) &= \frac{1}{E_p h (s^2 - \omega^2 / c_p^2)} - \frac{k_T^2 \beta}{\mu \Delta} \\
m_{12}(s) &= -\frac{is}{\mu \Delta} (2s^2 - k_T^2 - 2\alpha\beta) \\
m_{21}(s) &= -m_{12}(s) \\
m_{22}(s) &= -\frac{\alpha k_T^2}{\mu \Delta} - \frac{1}{\rho h \omega^2}
\end{aligned} \tag{3.61}$$

Therefore, by substituting Equation (3.60) into (3.49), and applying the inverse Fourier transform, the displacement field along the piezoelectric layer can be obtained as

$$\begin{cases} u_y = \frac{m_{22}(k_I)u_y^I - m_{12}(k_I)u_z^I}{E_p h (k_I^2 - \omega^2 / c_p^2) [m_{11}(k_I)m_{22}(k_I) - m_{12}(k_I)m_{21}(k_I)]} \\ u_z = \frac{m_{21}(k_I)u_y^I - m_{11}(k_I)u_z^I}{\rho h \omega^2 [m_{11}(k_I)m_{22}(k_I) - m_{12}(k_I)m_{21}(k_I)]} \end{cases} \tag{3.62}$$

Then all stress wave field in the substrate can also be obtained by substituting Equation (3.56) and (3.60) into (3.58).

3.5 Comparison and results

3.5.1 Dispersion curves

The dispersion curves of propagating waves can be determined by solving the dispersion equations obtained. Wave propagation in structures with a PZT-4 layer is studied. The material properties of PZT-4 used are $c_{11}=132 \text{ Gpa}$, $c_{12}=71 \text{ Gpa}$, $c_{13}=73 \text{ Gpa}$, $c_{33}=115 \text{ Gpa}$, $c_{44}=26 \text{ Gpa}$, $e_{31}=-4.1 \text{ C/m}^2$, $e_{33}=14.1 \text{ C/m}^2$, $e_{15}=10.5 \text{ C/m}^2$, $\rho=7500 \text{ Kg/m}^3$. For the substrate, Young's modulus, Poisson's ratio and mass density are 77.5 Gpa , 0.33 and 2700 Kg/m^3 respectively. The resulting dispersion curves from both simplified and exact models are shown in Fig. 3.4. The simplified model can determine the two lowest modes of wave

propagation in these layered structures. The lower branch mode starts from a velocity of 2884m/s when the wave number is 0. The Rayleigh wave velocity for the substrate, the aluminum half space, can be determined from Equation (3.27) to be 2889m/s. Therefore, this is a generalized Rayleigh mode, which starts from the Rayleigh wave of the substrate at $k=0$ and decreases with the increase of wave number. On the other hand, the dispersion curves of the upper mode also decrease with the increase of wave number.

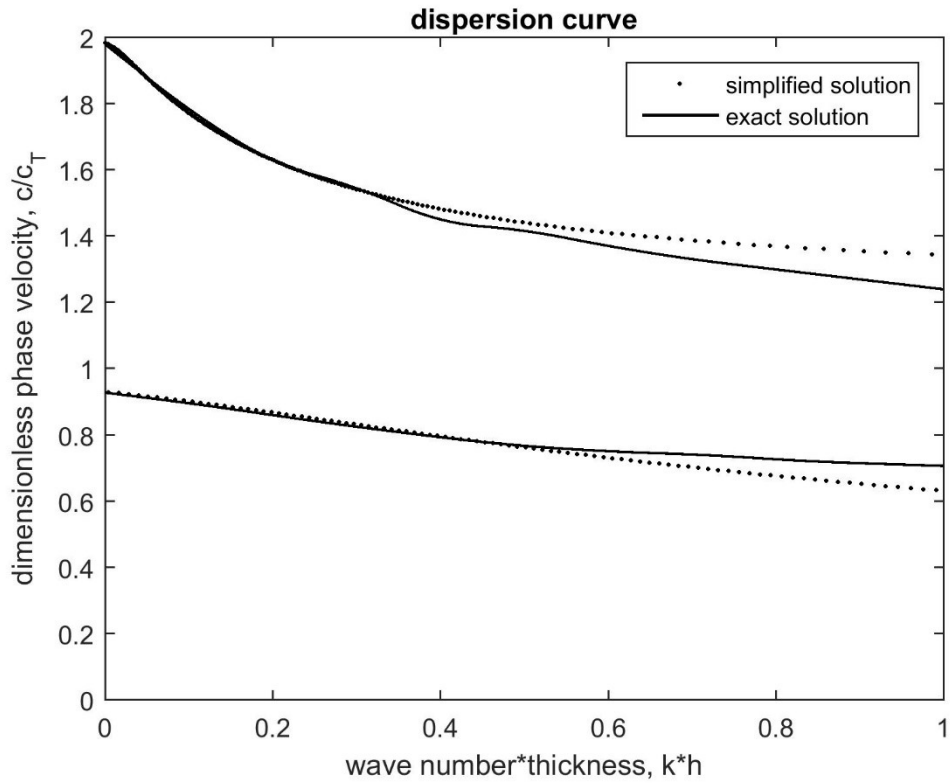


Fig. 3.4: Dispersion curves for the PZT4-Aluminum layered structure

The dispersion curves determined from the simplified model are compared with those from the exact model. The results of the simplified model are more accurate when the thickness of the layer is small compatible to the wavelength ($kh < 1$), while the error between the current results and the exact solutions will become bigger with the increase of the

thickness of the layer. As expected, this model is suitable for cases where a thin layer is bonded to an elastic substrate, which is consistent with the assumption of the current model.

Typical thickness of commonly used piezoelectric thin-sheets is in the range of 0.1mm to 0.5mm (Yu and Wang, 2016). Therefore, to guarantee the accuracy of the result ($kh < 1$), the corresponding longest wavelength the current simplified model can handle (when $kh = 1$) is about 0.6mm to 3.1mm, which will provide reasonable detection resolution for structural health monitoring.

3.5.2 Physical explanation

To understand the physical meaning of the two branches of the dispersion relation, the effect of the mass density and the transverse inertia of the piezoelectric layer will be studied in detail.

Based on the current analytical model, the dispersion curves of PZT-Aluminum layered structure for piezoelectric layers with different densities can be obtained, as demonstrated in Fig. 3.5. The density of piezoelectric layer has a significant influence on the dispersion curves, i.e. the phase velocity will increase with the decrease of the density of the piezoelectric layer. When the density approaches zero, the lower branch approaches that of Rayleigh wave. Therefore, the wave of the lower branch represents a generalized Rayleigh wave. When the piezoelectric layer is ignored, it will degenerate to Rayleigh wave, as discussed before. The upper branch disappears when the density approaches zero. Fig. 3.6 shows that the upper branch of dispersion curves will approach the effective longitudinal velocity of the piezoelectric layer $c_s = \sqrt{E_{eff} / \rho}$ when $k * h \rightarrow \infty$. This indicates that the upper branch apparently degenerate into longitudinal waves in the layer along the y -axis when $h \rightarrow \infty$.

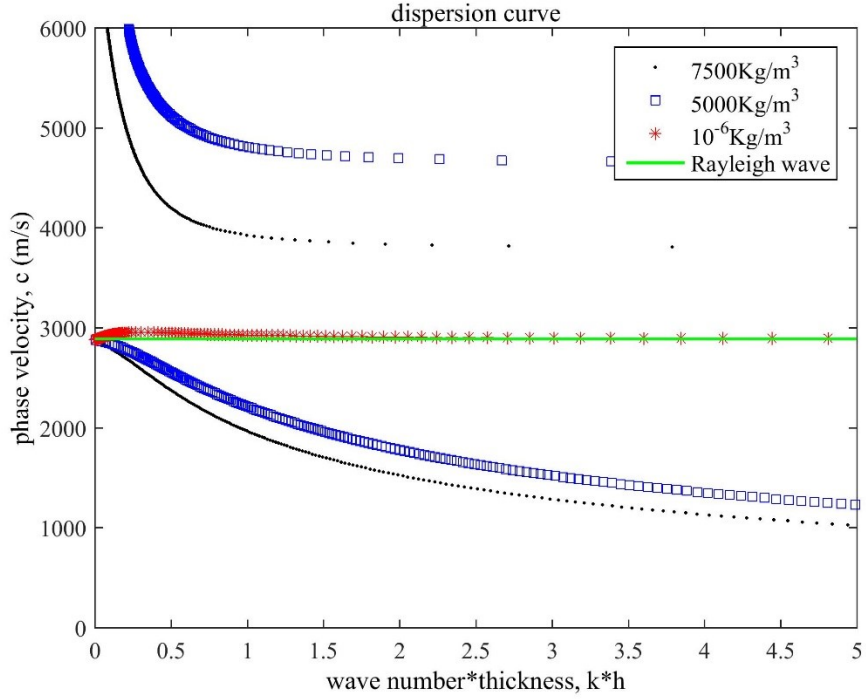


Fig. 3.5: Dispersion curves for different densities of the piezoelectric layer

To further evaluate the upper branch, the transverse inertia of the piezoelectric layer is ignored in the dispersion equation. In this case, the only non-zero stress component in the layer is σ_y , and $\sigma_z^s = \sigma_z = 0$, which results in

$$\left(\frac{b_1^2}{ik} + v^* ik\right)A_1 - ik(1 - v^*)A_2 = 0. \quad (3.63)$$

Equations (3.22) and (3.63) can be reorganized in a matrix form, from which, the dispersion equation can be determined and simplified to the following dispersion equation

$$\left(2\mu_s B_1 k + E_{eff} h \gamma\right)(1 - v^*) + \left[\mu_s k \left(B_2 + \frac{1}{B_2}\right) + E_{eff} h \gamma\right](v^* - B_1^2) = 0 \quad (3.64)$$

where $B_1 = \left(1 - c^2 / c_l^2\right)^{1/2}$, $B_2 = \left(1 - c^2 / c_r^2\right)^{1/2}$, $\gamma = k^2 - \frac{\omega^2}{c_s^2}$.

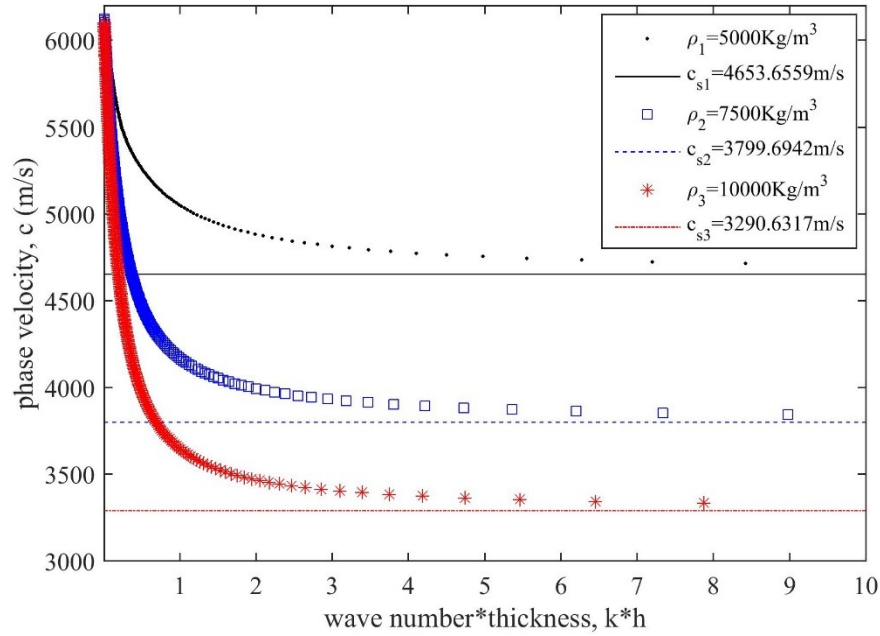


Fig. 3.6: Dispersion curves of the upper branch approaches the effective longitudinal velocity of the layer c_s

It can be observed that removing transverse inertia did not change the upper branch significantly, as shown in Fig. 3.7, indicating that the upper branch represents only a longitudinal mode wave along y -direction, while the lower branch represents a Rayleigh-like mode.

To show the generalized Rayleigh wave in the substrate, the displacement field is illustrated for a specific point at the dispersion curve of our solution, $c = 2000m/s$, $k = 1040/m$. In this case, when the amplitude of u_y is assumed to be unity, the real part of the displacement field in the substrate at $t = 1ms$ can be expressed as

$$\text{real}(u_y^s) = 26.3(e^{-984.4z} - 0.962e^{-794.6z})\cos[1040(y-2)] \quad (3.65)$$

$$\text{real}(u_z^s) = -26.3(0.9465e^{-984.4z} - 1.2591e^{-794.6z})\sin[1040(y-2)] \quad (3.66)$$

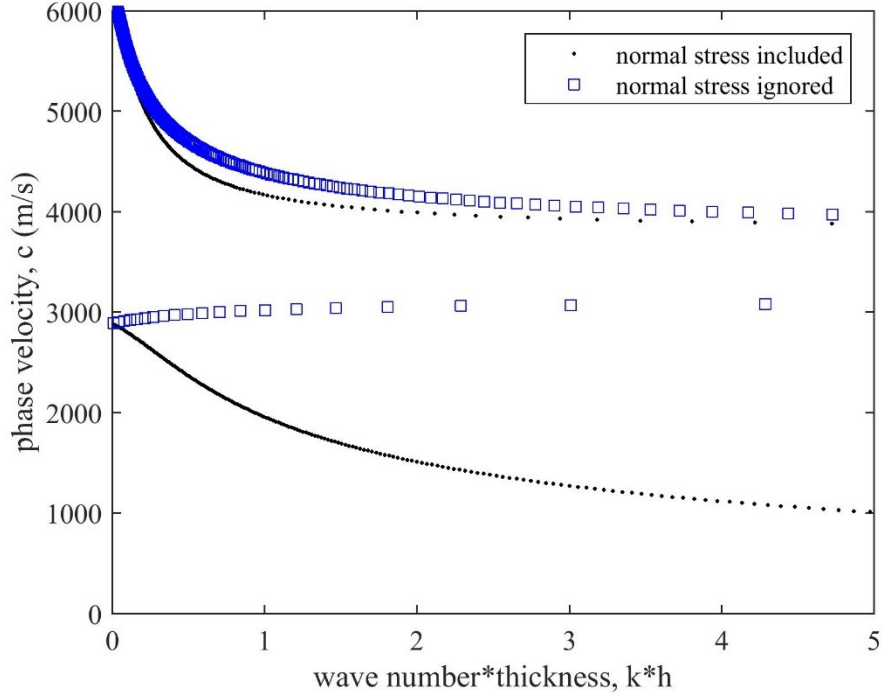


Fig. 3.7: Dispersion curve when the inertia of the piezo-layer in z-direction is ignored

The displacement fields (u_y^s and u_z^s) in the substrate are plotted in Fig. 3.8 and Fig. 3.9. At the interface, the displacements are the same to these in the piezoelectric layer. In the substrate, the wave shows clearly similar properties to that of Rayleigh wave with the amplitudes decaying exponentially with the increase of depth.

In summary, the current simplified model can determine the two lowest modes of wave propagation in the layered piezoelectric structure. The first mode is a generalized Rayleigh wave propagating in the layered structure, while the second mode is the generalized longitudinal wave, which is mainly propagating along the layer and affected by the supported substrate.

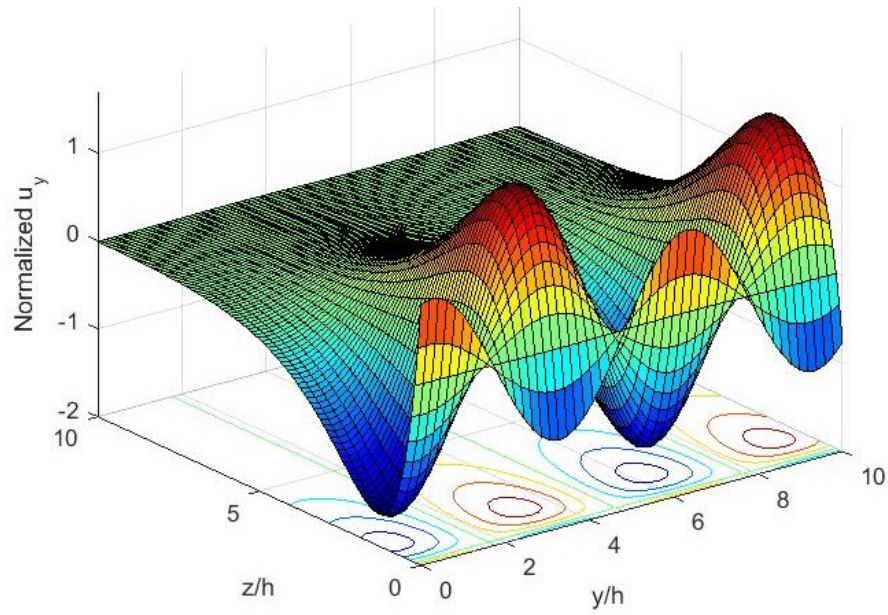


Fig. 3.8: The displacement wave field in y -direction when $k=1040/m$, $c=2000m/s$ and $t=1ms$

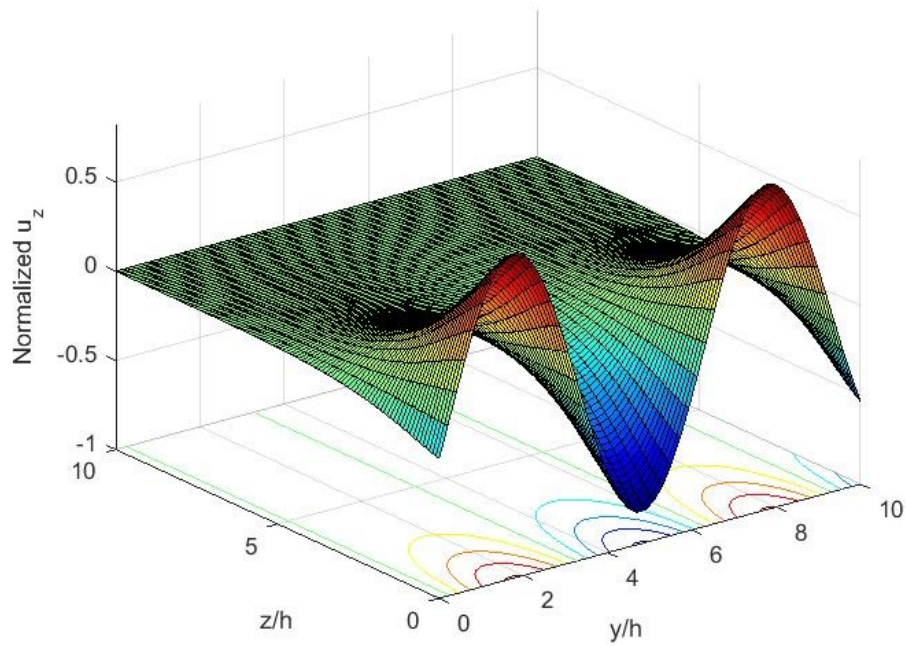


Fig. 3.9: The displacement wave field in z -direction when $k=1040/m$, $c=2000m/s$ and $t=1ms$

3.5.3 Wave propagation under a harmonic loading

Wave propagation in PZT4-Aluminum layered structure is studied. The analysis will focus on the dynamic load transfer from the substrate to the surface-bonded layer under different material combinations and loading frequencies.

The dynamic strain ratio (DSR) represents the percentage of deformation transferred from the host medium to the sensor, given by

$$\begin{aligned} DSR_y(y) &= \varepsilon_y(y) / \varepsilon_y^I(y), \\ DSR_z(y) &= \varepsilon_z(y) / \varepsilon_z^I(y). \end{aligned} \quad (3.67)$$

It is an index of the sensing characteristics of the piezoelectric layer. The dynamic strain ratio can be determined from

$$\begin{cases} DSR_y = \frac{m_{22}(k_I) - m_{12}(k_I)A_z^I / A_y^I}{E_p h(k_I^2 - \omega^2 / c_p^2)[m_{11}(k_I)m_{22}(k_I) - m_{12}(k_I)m_{21}(k_I)]} \\ DSR_z = \frac{m_{21}(k_I)A_y^I / A_z^I - m_{11}(k_I)}{\rho h \omega^2 [m_{11}(k_I)m_{22}(k_I) - m_{12}(k_I)m_{21}(k_I)]} \end{cases}. \quad (3.68)$$

Fig. 3.10 shows the amplitude of the dynamic strain ratio with different material combinations under different loading frequencies. The strain ratio will increase gradually with the decrease of the loading frequency and the increase of the material combination, which is defined as the ratio of Young's modulus of the substrate and that of the piezoelectric layer. Therefore, to gain a good dynamic strain ratio, high levels of loading frequency should be avoided and the stiffness of layers should not exceed that of the substrate too much.

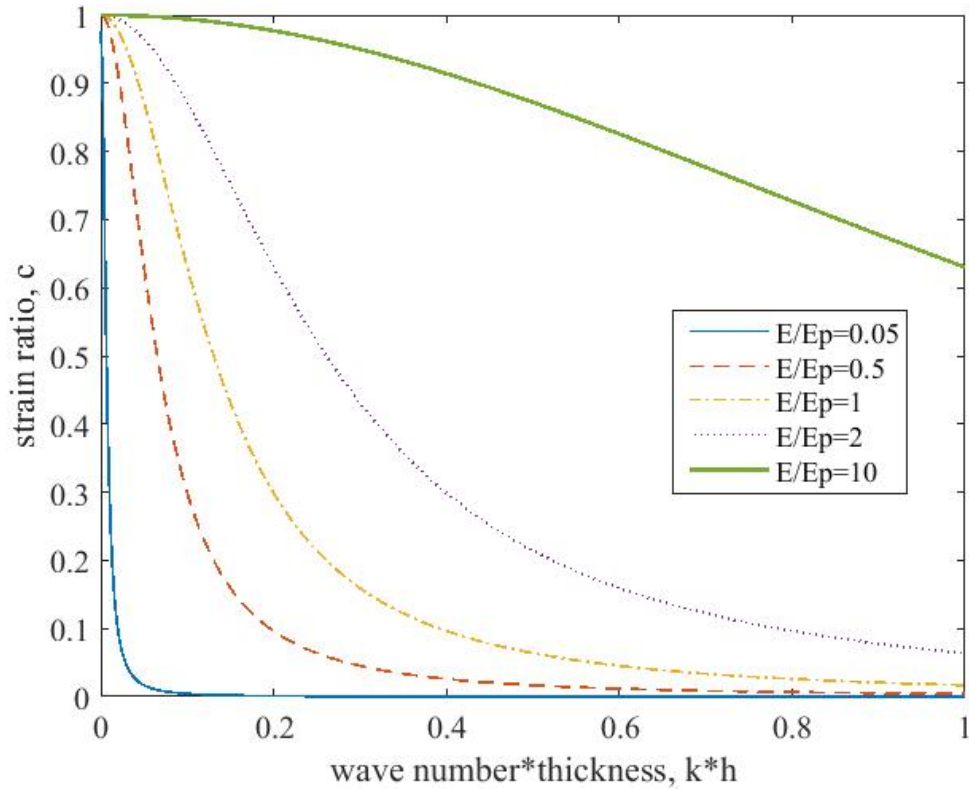


Fig. 3.10: Amplitude of strain ratio with different material combinations under different frequencies

3.6 Discussion

The present simplified model can reasonably predict the two lowest wave modes in the layered structure. Because it is analytical in nature, the model is useful and convenient to use to analyze the complicated wave phenomena, such as the effects of the piezoelectricity and the material combinations.

3.6.1 Effect of the piezoelectricity

Dispersion curves for the PZT4-Aluminum structure with and without the piezoelectric effect are plotted in Fig. 3.11. The piezoelectric effect shows a significant influence on the

generalized longitudinal wave but insignificant effect on the generalized Rayleigh wave propagation.

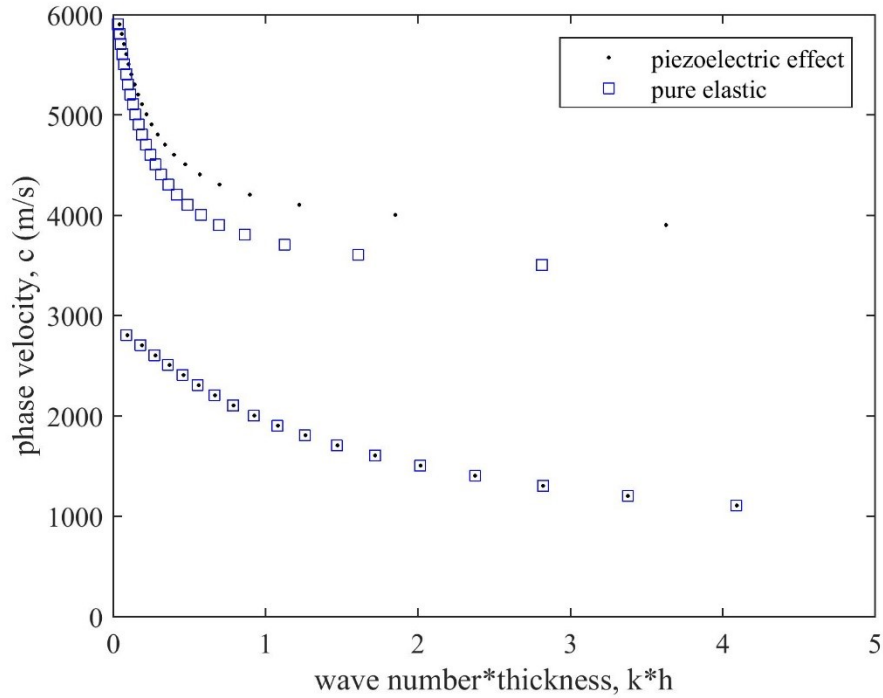


Fig. 3.11: Comparison of dispersion curves with and without the piezoelectric effect

3.6.2 Effect of the material combinations

The dispersion curves for different mass densities are studied and given in Fig. 3.5, from which the physical meaning of each mode was clearly shown. According to previous analysis in (Achenbach and Keshava, 1967), the dispersion curves will be affected by the stiffness ratio, which is defined as the ratio of Young's modulus of the substrate (E_s) to the effective Young's modulus of the piezoelectric layer (E_{eff}). When the material properties of the layer are given and fixed, the dispersion curves for different Young's moduli of the substrate can be obtained, which are shown in Fig. 3.12.

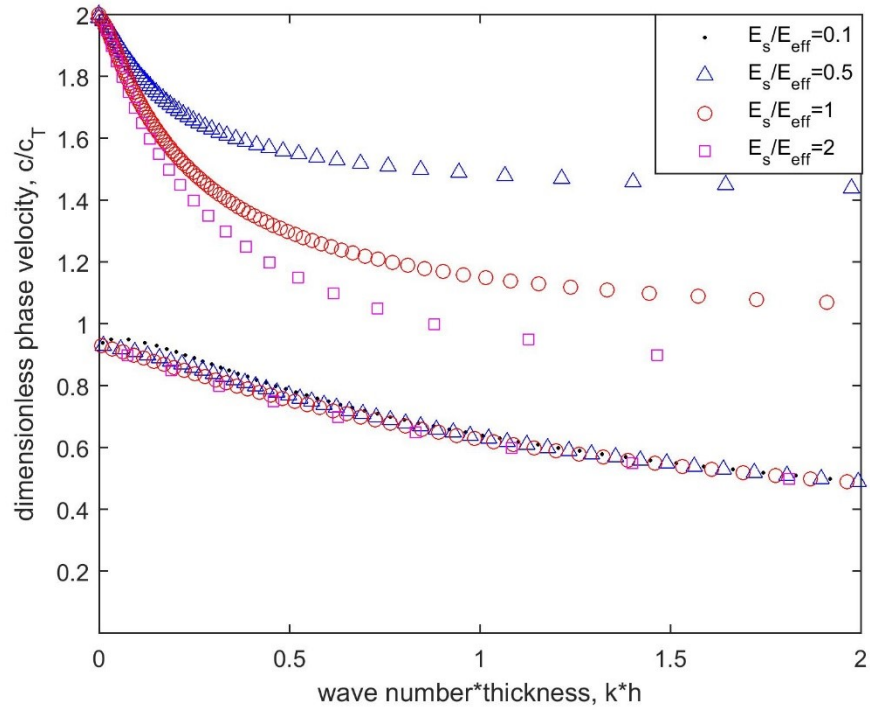


Fig. 3.12: Effect of the stiffness ratio on the dispersion curve

For the generalized Rayleigh mode wave, there is only limit effect of the stiffness ratio. For the generalized longitudinal mode wave, the phase velocity will increase significantly with the decrease of the stiffness ratio. When the substrate is much softer than the layer, there will be only one mode exists, and the upper mode will disappear. The critical value for the existence of the upper mode is determined by the ratio of the longitudinal velocity of the layer, $c_s = \sqrt{E_{eff} / \rho}$, to that of the substrate, $c_L = \sqrt{(\lambda_s + 2\mu_s) / \rho_s}$. As shown in Fig. 3.13, when $c_L / c_s > 1$, the upper mode exists, while it will disappear and only the lower mode exists when $c_s > c_L$.

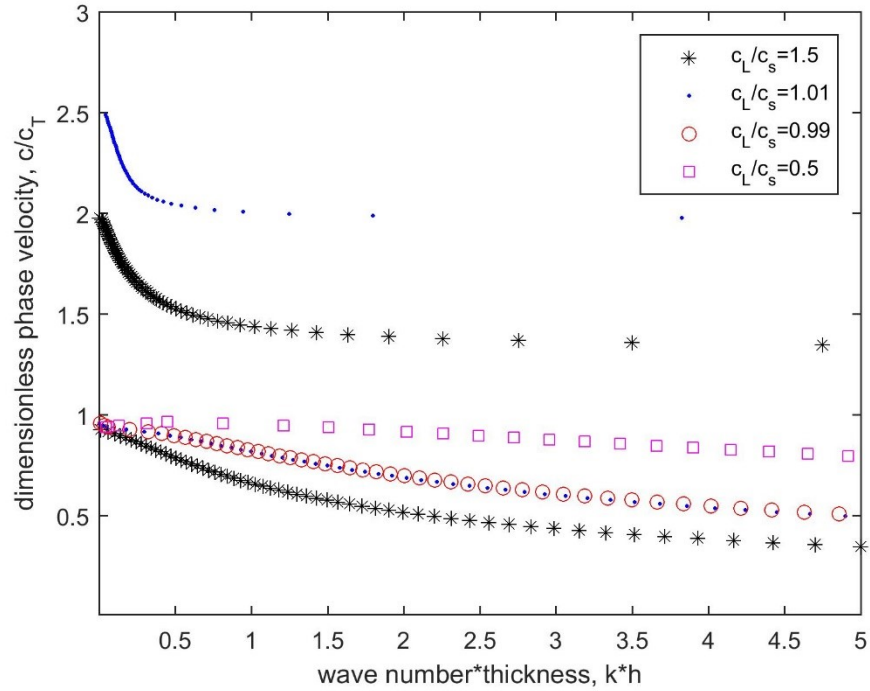


Fig. 3.13: Dispersion curves for different longitudinal velocity ratio c_L/c_s (the higher order branch only exists when $c_L/c_s > 1$)

3.7 Conclusions

A simplified model is developed and compared to describe how waves propagate in a semi-infinite elastic substrate with a surface-bonded piezoelectric layer. The current model assumes that the piezoelectric layer can be modelled as an electro-elastic film, which reduces the complex problem to the non-trivial solution of binary quadratic equations. This model is validated by comparing with exact results, indicating that the model is reliable when the thickness of the layer is smaller or comparable to the typical wavelength. For specific examples, the dispersion curves are presented and analyzed. The physical meanings of the two branches of the dispersion curve are examined by analyzing the effect of the transverse inertia and the density of the piezoelectric layer. The influence of the piezoelectric effect and

the material combination is also examined and discussed. The piezoelectric effect shows much more significant influence on the generalized longitudinal wave than that on the generalized Rayleigh wave and the upper mode only exists when the longitudinal wave of the substrate is bigger than that of the layer. Also, the in-plane dynamic behaviour of the layered piezoelectric structure is studied to evaluate the dynamic load transfer from the substrate to the layer under different loading frequencies and material combinations. Lower loading frequency and lower ratio between the stiffness of the piezoelectric layer and that of the substrate will result in higher dynamic strain ratio, which is desirable for the smart structures. The current model can be used as a benchmark for the study of wave propagation in this type of piezoelectric coupled structures.

Chapter 4: Dynamic interaction between piezoelectric sensors and embedded cracks

This chapter provides a new semi-analytical solution to simulate the complicated dynamic interaction between piezoelectric sensors and cracks under plane elastic wave loading. The solution is obtained using proper superposition and the pseudo incident wave (PsIW) method, which takes the advantages of the reliability of analytical solutions and the flexibility of numerical methods. The explicit forms of the voltage output of the piezoelectric sensor and dynamic stress intensity factors (SIFs) of embedded cracks are determined. Numerical examples are given to illustrate the effect of embedded cracks upon voltage output of the piezoelectric sensor due to the interaction between them. In this chapter, problem statement and formulation is presented firstly. Secondly, the dynamic behaviour of the piezoelectric sensor is modelled based on the results in Chapter 2 and 3. Thirdly, the scattered waves from a single crack are summarized, followed by dynamic interaction between the sensor and cracks. Lastly, the results, discussion and conclusions are given.

This chapter determines the voltage output of the piezoelectric sensor in response to crack parameters by solving the complicated dynamic interaction. The voltage output will be integrated into an optimization process into the next Chapter to estimate crack parameters quantitatively.

4.1 Introduction

In typical advanced piezoelectric based SHM systems for crack detection, elastic waves will be reflected between the attached piezoelectric sensors/actuators and embedded cracks. The

interaction between these sensors and cracks will cause the redistribution of the local stress and electric fields. Because of the complexity of the problem, when dynamic loads are applied, the simulation of the dynamic response of such coupled systems possesses a significant challenge, due to the multiple scattering among these sensors/cracks.

The methods for multiple scattering of elastic waves are summarized in Section 1.2.3. The main numerical methods are T-matrix methods (Waterman, 1965), boundary element methods (BEM) (Cruse, 1972), and finite difference time domain method (FDTD) (Botteldooren, 1995). These numerical methods can be used to conduct the dynamic simulation of these problems under certain conditions but have their own limitations when multiple interactions are involved, because of the computing resource needed to obtain reliable results. Besides, most of these problems are governed by highly singular boundary integral equations, so they are less accurate and less efficient compared to analytical solutions (Wang et al., 2015).

Analytical or semi-analytical study of interacting inhomogeneities under dynamic loads is very attractive because of its high reliability and accuracy but is limited to only simple cases of single inhomogeneity of certain types. For the dynamic interaction of these regular shaped scatters, analytical or semi-analytical solutions can be found with solutions of scattered field from a single scatter and pseudo incident wave (PsIW) method. The PsIW method was firstly provided by Wang and Meguid (1997) for solving multiple scattering problems in an infinite elastic medium with a through-thickness crack and a circular fibre subjected to anti-plane loadings. Then, this method was used to determine the interactions between piezoelectric actuators (Wang and Huang, 2001, 2006a) and dynamic interactions among a large number of circular inhomogeneities (Wang and Wang, 2016). However, the

PsiIW method in these studies was all applied to the dynamic interactions in infinite mediums. For the interaction problems in layered structures, the scattered waves of cracks will be reflected by interfaces between layers, resulting in complicated displacement and stress distribution near the interfaces, which cannot be solved by using the pseudo-incident wave technique directly. Besides, to the best of authors' knowledge, the dynamic interaction between surface bonded piezoelectric sensors and embedded cracks has not been studied.

The objective of this chapter is to investigate the multiple scattering of elastic waves in advanced piezoelectric based SHM systems and the effect of embedded cracks upon the voltage output of a piezoelectric smart sensor. The PsiIW method and proper superposition will be used to solve the dynamic interaction between sensors and cracks theoretically. By using this method, the dynamic interaction problem is reduced to the coupled solution of single crack problems and single piezoelectric sensor problems, for which analytical solutions or simpler numerical solutions could be derived. By considering the consistency condition between different cracks/sensors, the steady state dynamic solution of multiple interaction problems can be formulated as a system of coupled single crack/sensor solutions. Numerical examples are presented to show the effectiveness of the PsiIW method in simulating dynamic interaction problems of electromechanical structures under complicated geometries.

4.2 Problem statement and formulation

A piezoelectric smart sensor with uniform thickness h is surface-bonded to a homogeneous isotropic elastic solid structure, in which multiple cracks are embedded, as shown in Fig. 4.1.

It is assumed that the poling direction of the piezoelectric sensor is along the z -axis, perpendicular to the x - y plane. Since the host structure is much thicker than the piezoelectric sensor, it can be modelled as a semi-infinite plane (Qian and Hirose, 2012). The effect of the thin electrodes is ignored. To describe the structure, a global Cartesian coordinate (y, z) is used, shown in Fig. 4.1, and n local Cartesian systems (y_i, z_i) , $i=1,2,\dots,n$ are used to characterize the cracks. The half-lengths and the orientation angles of the cracks are assumed to be c_i and ϕ_i ($i=1,2,\dots,n$), respectively. The centre of the i th crack is assumed to be located at (y_i^c, z_i^c) in the global Cartesian coordinate.

The problem investigated is the dynamic interaction of surface bonded piezoelectric smart sensor with embedded cracks under a harmonic plane strain loading. In this case, the field variables, displacement, stress and strain, are all in the form of $\bar{A}(y, z, t) = A(y, z)e^{-i\omega t}$. For convenience, $e^{-i\omega t}$ term will be omitted in the following discussion and only the magnitude $A(y, z)$ will be considered.

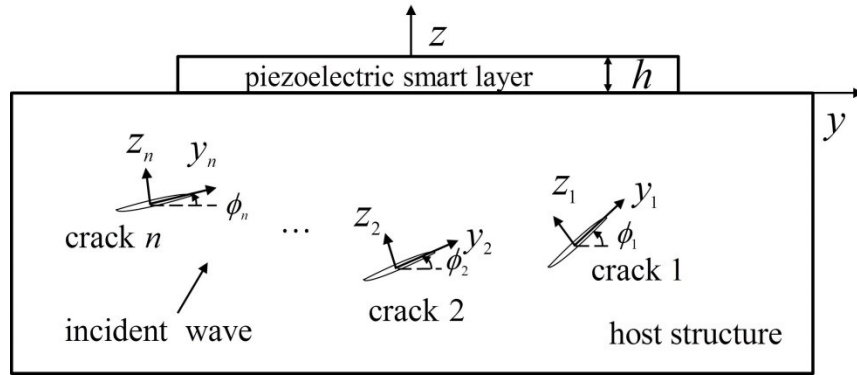


Fig. 4.1: The advanced piezoelectric structures with embedded cracks

The current dynamic interaction problem involves complex boundary conditions and interfacial conditions which result in multiple scattering of elastic waves among the

piezoelectric smart sensors and cracks. To overcome this difficulty, instead of dealing with the original problem directly, this problem will be solved using the pseudo-incident wave method and proper superposition, which reduce the original interaction problem to the solution of coupled single piezoelectric sensor and single crack problems, as shown in Fig. 4.2.

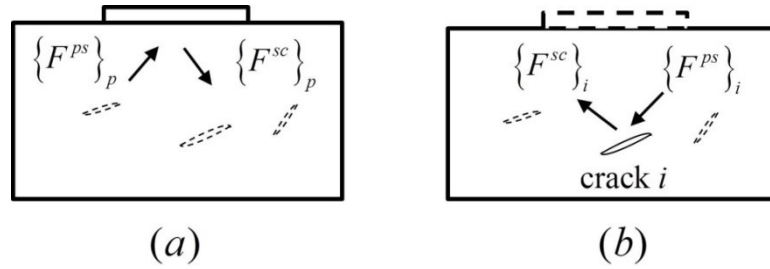


Fig. 4.2: The pseudo-incident wave method: (a) single piezoelectric sensor problem; (b) single crack problem

In the single piezoelectric sensor problem (Fig. 4.2(a)), the effects of cracks and the original incident wave upon the sensor are represented by a pseudo incident wave $\{F^{ps}\}_p$, which can be expressed as

$$\{F^{ps}\}_p = \sum_{j=1}^n \{F^{sc}\}_{pj} + \{F^0\}_p \quad (4.1)$$

where $\{F^0\}_p$ and $\{F^{sc}\}_{pj}$ are the resulting stress components along the host-sensor interface induced by the original incident wave and the scattered wave from the j th crack, respectively. In this problem, the piezoelectric sensor is subjected to the pseudo incident wave $\{F^{ps}\}_p$ and a scattered wave will be generated, which is assumed to be $\{F^{sc}\}_p$.

For the crack problem (Fig. 4.2(b)), every crack is subjected to the original incident wave and scattered waves from the piezoelectric sensor and all other cracks. Therefore, the pseudo incident wave for crack i is

$$\{F^{ps}\}_i = \{F^p\}_i + \sum_{\substack{j=1 \\ j \neq i}}^n \{F^{sc}\}_{ij} + \{F^0\}_i \quad (4.2)$$

where $\{F^0\}_i$, $\{F^p\}_i$ and $\{F^{sc}\}_{ij}$ are the resulting stresses along the surface of the i th crack ($z_i = 0$) induced by the original incident wave, the reflected wave from the piezoelectric sensor and the scattered wave from the j th crack, respectively. In this problem, crack i is subjected to the pseudo incident wave $\{F^{ps}\}_i$ and a scattered wave $\{F^{sc}\}_i$ will be generated.

In this thesis, the superscript ‘0’, ‘sc’ and ‘ps’ representing the original incident wave, the scattered wave and the unknown pseudo-incident wave field, respectively, and the subscript ‘p’, ‘s’ and ‘i’ indicate the piezoelectric sensor, substrate (i.e. host structure) and the i th crack, respectively.

4.3 Dynamic behaviour of the piezoelectric sensor

Consider first a piezoelectric sensor is perfectly bonded to a semi-infinite elastic host structure, under a general pseudo incident wave, as discussed in the previous section, and then a scattered wave will be generated from the reflection of the sensor-host interface and free surface of the semi-infinite medium, as shown in Fig. 4.2(a).

4.3.1 Modelling of the piezoelectric smart sensor

Per the piezoelectric thin-sheet modelling as presented in Chapter 2, the axial stress can be assumed to be consistent across the thickness. The accuracy of this assumption has been validated for both static (Wang and Meguid, 2000) and dynamic cases (Wang and Huang, 2006b). The result from Chapter 1 indicates that the axial stiffness along the sensor will play a much more important role than its flexural stiffness. Therefore, the piezoelectric sensor can be modelled as an electro-elastic thin layer (thin film) subjected to a distributed axial stress τ/h .

The equation of motion of the piezoelectric sensor is

$$\frac{d\sigma_y}{dy} + \frac{\tau(y)}{h} + \rho\omega^2 u_y = 0 \quad (4.3)$$

where σ_y is the average axial stress, u_y is the average axial displacement, and ρ is the mass density of the piezoelectric sensor.

Because the two tips of the surface-bonded piezoelectric sensor are traction free, the axial boundary conditions can be expressed as

$$\sigma_y(y) = 0 \quad \text{at } |y| = a \quad (4.4)$$

The constitutive relation of the piezoelectric layer under the plane strain and open-loop condition can be described as (Wang and Huang, 2006b):

$$\sigma_y = E_p \frac{\partial u_y}{\partial y}, \quad E_p = E + \frac{e^2}{\lambda} \quad (4.5)$$

with $E = c_{11} - \frac{c_{13}^2}{c_{33}}$, $e = e_{13} - e_{33} \frac{c_{13}}{c_{33}}$, $\lambda = \lambda_{33} + \frac{e_{33}^2}{c_{33}}$. c_{ij} are the stiffness parameters, e_{ij} are the piezoelectric constants, and λ_{ij} are the dielectric constants, as shown in the appendix.

Substituting Equation (4.5) into Equation (4.3) results in

$$\frac{\partial^2 u_y(y)}{\partial y^2} + k_p^2 u_y(y) + \frac{\tau(y)}{E_p h} = 0 \quad (4.6)$$

where k_p and c_p being the wave number and the actual wave velocity of the axial wave in the piezoelectric sensor, with $k_p = \omega / c_p$ and $c_p = \sqrt{E_p / \rho}$.

The general solution of the displacement $u(y)$ can be determined by solving Equation (4.4) and (4.6) as

$$u_y(y) = A_p \sin k_p y + B_p \cos k_p y + \int_{-a}^y \sin k_p (\zeta - y) \frac{\tau(\zeta)}{h k_p E_p} d\zeta \quad (4.7)$$

with

$$A_p = \frac{\sin k_p a}{h k_p E_p \sin 2k_p a} \int_{-a}^a \cos k_p (\zeta - a) \tau(\zeta) d\zeta$$

$$B_p = -\frac{\cos k_p a}{h k_p E_p \sin 2k_p a} \int_{-a}^a \cos k_p (\zeta - a) \tau(\zeta) d\zeta,$$

then, the axial strain of the piezoelectric layer can be obtained as

$$\varepsilon_y(y) = \frac{\sin k_p (a + y)}{h E_p \sin 2k_p a} \int_{-a}^a \cos k_p (\zeta - a) \tau(\zeta) d\zeta$$

$$- \int_{-a}^y \cos k_p (\zeta - y) \frac{\tau(\zeta)}{h E_p} d\zeta, \quad |y| < a \quad (4.8)$$

4.3.2 The elastic field of the host medium

The host structure is subjected to the pseudo-incident wave and interfacial stresses induced by the piezoelectric sensor, as indicated in Fig. 4.3(a). The wave field inside the host structure can be expressed by superimposing the two sub-problems, as illustrated in Fig. 4.3(b) and Fig. 4.3(c). Sub-problem (b) represents the pseudo incident wave (original incident wave plus the scattered wave from the cracks) propagating in an infinite elastic medium, and sub-problem (c) represents the dynamic response of the semi-infinite host structure subjected to the following surface loading:

$$\begin{cases} \tau_{yz}^s(y,0) = -\tau - \tau_2 & |y| < a \\ \tau_{yz}^s(y,0) = -\tau_2 & |y| > a \end{cases}, \quad \sigma_z^s(y,0) = -\sigma_2 \quad (4.9).$$

where τ_{yz}^s and σ_z^s represent the shear and normal stresses of the scattered wave in the substrate, and τ_2, σ_2 are the shear and normal stresses at the sensor-host interface induced by the pseudo incident wave in sub-problem 4(b).

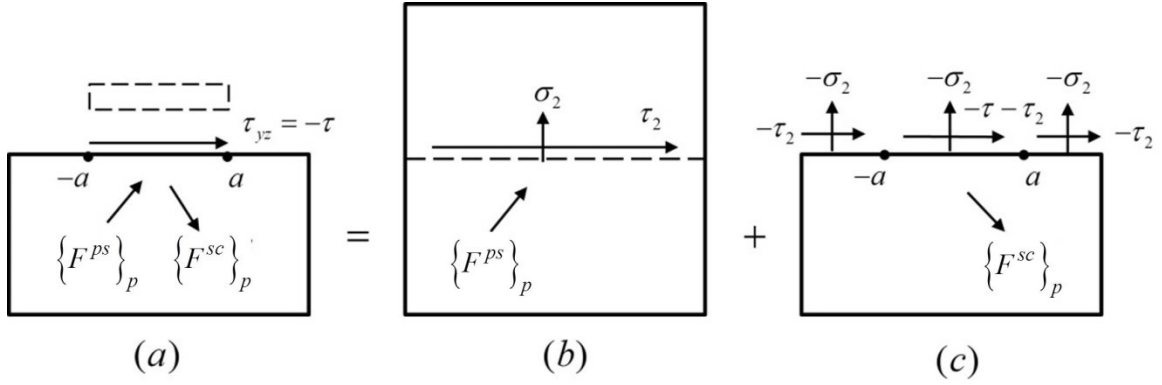


Fig. 4.3: Superposition of wave propagation in the layered piezoelectric structures

The host medium is homogeneous isotropic and under steady state plane strain loading. The dynamic behaviour is governed by the following Helmholtz equations of two displacement potentials ϕ and ψ (Achenbach, 1973, p291)

$$(\nabla^2 + K^2)\phi = 0, \quad (\nabla^2 + k^2)\psi = 0 \quad (4.10)$$

where $\nabla^2 = (\partial^2 / \partial y^2) + (\partial^2 / \partial z^2)$ is the Laplacian operator, and $K = \omega / c_L$, $k = \omega / c_T$ are longitudinal and transverse wave numbers respectively, with ω , c_L , c_T being the circular frequency of the loading, the longitudinal velocity and transverse velocity in the host structure, respectively.

Equation (4.10) can be solved by applying the following Fourier transform over y ,

$$\bar{f}(s) = \frac{1}{2\pi} \int_{-\infty}^{+\infty} f(y) e^{isy} dy, \quad f(y) = \int_{-\infty}^{+\infty} \bar{f}(s) e^{-isy} ds, \quad (4.11)$$

from which the general solution of the two displacement potentials of the scattered field can be expressed in the Fourier domain as

$$\begin{aligned} \bar{\phi}(s, z) &= \begin{cases} A_1(s) e^{-\alpha z}, & z > 0 \\ A_2(s) e^{\alpha z}, & z < 0 \end{cases} \\ \bar{\psi}(s, z) &= \begin{cases} A_3(s) e^{-\alpha z}, & z > 0 \\ A_4(s) e^{\alpha z}, & z < 0 \end{cases}, \end{aligned} \quad (4.12)$$

where $A_i(s)$, $i = 1, 2, 3, 4$ are four unknown functions of s , and α , β are

$$\alpha = \begin{cases} \sqrt{s^2 - K^2}, & |s| > K \\ -i\sqrt{K^2 - s^2}, & |s| < K \end{cases} \quad (4.13)$$

$$\beta = \begin{cases} \sqrt{s^2 - k^2}, & |s| > k \\ -i\sqrt{k^2 - s^2}, & |s| < k \end{cases} \quad (4.14)$$

which guarantee that the stress components of the solution will level off to zero at infinity.

The non-vanishing displacement components can be expressed by $A_i(s)$, $i = 1, 2, 3, 4$ as

$$\begin{aligned} u_y &= \frac{\partial \phi}{\partial y} + \frac{\partial \psi}{\partial z} = \begin{cases} \int_{-\infty}^{+\infty} [-isA_1(s) e^{-\alpha z} - \beta A_3(s) e^{-\beta z}] e^{-isy} ds, & z > 0 \\ \int_{-\infty}^{+\infty} [-isA_2(s) e^{\alpha z} + \beta A_4(s) e^{\beta z}] e^{-isy} ds, & z < 0 \end{cases} \\ u_z &= \frac{\partial \phi}{\partial z} - \frac{\partial \psi}{\partial y} = \begin{cases} \int_{-\infty}^{+\infty} [-\alpha A_1(s) e^{-\alpha z} + isA_3(s) e^{-\beta z}] e^{-isy} ds, & z > 0 \\ \int_{-\infty}^{+\infty} [\alpha A_2(s) e^{\alpha z} + isA_4(s) e^{\beta z}] e^{-isy} ds, & z < 0 \end{cases}. \end{aligned} \quad (4.15)$$

The corresponding strain components are

$$\varepsilon_y = \frac{\partial u_y}{\partial y}, \quad \varepsilon_z = \frac{\partial u_z}{\partial z}, \quad \varepsilon_{yz} = \frac{1}{2} \left(\frac{\partial u_y}{\partial z} + \frac{\partial u_z}{\partial y} \right) \quad (4.16)$$

and the stress components can be determined through Hooke's law as

$$\begin{aligned}
\sigma_y &= \frac{E_s(1-\nu_s)}{(1-2\nu_s)(1+\nu_s)} \left\{ \begin{aligned} &\int_{-\infty}^{+\infty} \left[\left(-s^2 + \frac{\nu_s}{1-\nu_s} \alpha^2 \right) A_1(s) e^{-\alpha z} + is\beta \frac{1-2\nu_s}{1-\nu_s} A_3(s) e^{-\beta z} \right] e^{-isy} ds, \quad z > 0 \\ &\int_{-\infty}^{+\infty} \left[\left(-s^2 + \frac{\nu_s}{1-\nu_s} \alpha^2 \right) A_2(s) e^{\alpha z} - is\beta \frac{1-2\nu_s}{1-\nu_s} A_4(s) e^{\beta z} \right] e^{-isy} ds, \quad z < 0 \end{aligned} \right. \\
\sigma_z &= \frac{E_s(1-\nu_s)}{(1-2\nu_s)(1+\nu_s)} \left\{ \begin{aligned} &\int_{-\infty}^{+\infty} \left[\left(\alpha^2 - \frac{\nu_s}{1-\nu_s} s^2 \right) A_1(s) e^{-\alpha z} - is\beta \frac{1-2\nu_s}{1-\nu_s} A_3(s) e^{-\beta z} \right] e^{-isy} ds, \quad z > 0 \\ &\int_{-\infty}^{+\infty} \left[\left(\alpha^2 - \frac{\nu_s}{1-\nu_s} s^2 \right) A_2(s) e^{\alpha z} + is\beta \frac{1-2\nu_s}{1-\nu_s} A_4(s) e^{\beta z} \right] e^{-isy} ds, \quad z < 0 \end{aligned} \right. \quad (4.17) \\
\tau_{yz} &= \mu_s \left\{ \begin{aligned} &\int_{-\infty}^{+\infty} \left[2is\alpha A_1(s) e^{-\alpha z} + (\beta^2 + s^2) A_3(s) e^{-\beta z} \right] e^{-isy} ds, \quad z > 0 \\ &\int_{-\infty}^{+\infty} \left[-2is\alpha A_2(s) e^{\alpha z} + (\beta^2 + s^2) A_4(s) e^{\beta z} \right] e^{-isy} ds, \quad z < 0 \end{aligned} \right.
\end{aligned}$$

where E_s , ν_s and μ_s are the Young's modulus, Poisson's ratio and shear modulus of the host structure with $\mu_s = \frac{E_s}{2(1+\nu_s)}$.

The dynamic response of a half space is a well-established problem in elasticity (Muskhelishvili, 1977; Wang and Huang, 2006b). If the stress boundary conditions at the surface ($z=0$) are given, the unknown parameters $A_2(s)$ and $A_4(s)$ can be determined by substituting Equations (4.17) into the boundary conditions. The resulting dynamic strain along the interface between the piezoelectric layer and the host structure in Fig. 4.3(c) can be obtained as

$$\begin{aligned}
\varepsilon_y^s(y, 0) &= \\
&\frac{2}{\pi \bar{E}_s} \left[\int_{-a}^a \frac{\tau(\zeta)}{y-\zeta} d\zeta - \int_{-a}^a \tau(\zeta) \int_0^\infty \left[\frac{k_T^2 s \beta}{(1-\nu_s) \Delta} + 1 \right] \sin[s(y-\zeta)] ds d\zeta \right] + \varepsilon_y^B(y), \quad |y| < a \quad (4.18)
\end{aligned}$$

where ε_y^B is the outgoing strain wave induced by the surface loading $-\tau_2$ and $-\sigma_2$, with

$$\begin{aligned}\varepsilon_y^B(y) &= \frac{-ik_T^2}{2\pi\mu_s} \int_{-\infty}^{\infty} \tau_2(\zeta) \int_{-\infty}^{\infty} \frac{s\beta}{\Delta} e^{-is(y-\zeta)} ds d\zeta \\ &\quad - \frac{1}{2\pi\mu_s} \int_{-\infty}^{\infty} \sigma_2(\zeta) \int_{-\infty}^{\infty} \frac{s^2}{\Delta} (2\alpha\beta - 2s^2 + k_T^2) e^{-is(y-\zeta)} ds d\zeta\end{aligned}\quad (4.19)$$

and

$$\Delta = (2s^2 - k_T^2)^2 - 4s^2\alpha\beta, \quad \bar{E}_s = E_s / (1 - \nu_s^2). \quad (4.20)$$

4.3.3 Governing equations and numerical solutions

Considering the continuity of the strain along the layer-host interface, and using equations (4.8) and (4.18), the following governing equation for the piezoelectric structure is obtained

$$\begin{aligned}& -\int_{-a}^a \frac{\tau(\zeta)}{y-\zeta} d\zeta + \int_{-a}^a \tau(\zeta) \int_0^{\infty} \left[\frac{k_T^2 s \beta}{(1-\nu_s)\Delta} + 1 \right] \sin[s(y-\zeta)] ds d\zeta \\ & + \lambda \frac{\sin k_p(a+y)}{h \sin 2k_p a} \int_{-a}^a \cos k_p(\zeta-a) \tau(\zeta) d\zeta - \frac{\lambda}{h} \int_{-a}^y \cos k_p(\zeta-y) \tau(\zeta) d\zeta \\ & = \frac{\pi \bar{E}_s}{2} \varepsilon_y^B(y), \quad |y| < a\end{aligned}\quad (4.21)$$

where $\lambda = \pi \bar{E}_s / (2E_p)$ is the material mismatch between the piezoelectric sensor and the host structure.

The resulting governing integral equation contains a square-root singularity solution of τ at the two tips of the piezoelectric sensor. This equation can be solved by expressing the interfacial shear stress in terms of Chebyshev polynomials

$$\tau(y) = \sum_{j=0}^{\infty} d_j T_j(y/a) / \sqrt{1 - y^2/a^2}$$

where T_j is the Chebyshev polynomial of the first kind of j th order with $T_j(\cos \theta) = \cos(j\theta)$.

To provide a solution to the problem, the Chebyshev polynomial will be truncated to N th term, and Equation (4.21) will be satisfied at the selected collocation points given by

$$\eta^l = y^l / a = \cos\left(\frac{l-1}{N-1}\pi\right), \quad l=1,2, \dots, N \quad (4.22)$$

The governing equation can be reduced to N linear algebraic equations in terms of

$\{d\}_p = \{d_1, d_2, \dots, d_N\}^T$ as

$$[B]_p \{d\}_p = \{F^{sc}\}_p \quad (4.23)$$

where $[B]_p$ is a known matrix given by

$$B_{lj} = -\pi \frac{\sin\left[j \cos^{-1} \eta^l\right]}{\sin\left[\cos^{-1} \eta^l\right]} + \lambda \nu \int_{\cos^{-1} \eta^l}^{\pi} \cos\left[\bar{k}_p (\cos \theta - \eta^l)\right] \cos(j\theta) d\theta$$

$$+ \pi \begin{cases} \int_0^{\infty} (-1)^n J_j(\bar{s}) \cos(\bar{s} \eta^l) \left[\frac{\bar{k}^2 \bar{s} \bar{\beta}}{(1-\nu_s) \bar{\Delta}} + 1 \right] d\bar{s} - \lambda \nu \frac{\sin\left[\bar{k}_p (\eta^l + 1)\right]}{\sin(2\bar{k}_p)} (-1)^n J_j(\bar{k}_p) \sin(\bar{k}_p), & j = 2n+1 \\ \int_0^{\infty} (-1)^{n+1} J_j(\bar{s}) \sin(\bar{s} \eta^l) \left[\frac{\bar{k}^2 \bar{s} \bar{\beta}}{(1-\nu_s) \bar{\Delta}} + 1 \right] d\bar{s} - \lambda \nu \frac{\sin\left[\bar{k}_p (\eta^l + 1)\right]}{\sin(2\bar{k}_p)} (-1)^n J_j(\bar{k}_p) \cos(\bar{k}_p), & j = 2n \end{cases}$$

$$l=1,2, \dots, N; j=1,2, \dots, N. \quad (4.24)$$

In above equations

$$\eta^l = y^l / a, \quad \bar{k} = ka, \quad \bar{k}_p = k_p a, \quad \bar{s} = sa, \quad \nu = a / h$$

with J_j being the Bessel functions of the first kind. $\bar{\alpha}$, $\bar{\beta}$ and $\bar{\Delta}$ can be obtained from

Equations (4.13), (4.14) and (4.20) directly with s , K and k being replaced by \bar{s} , \bar{K} and

\bar{k} , respectively.

The matrix $\{F^{sc}\}_p = \{F_1, F_2, \dots, F_N\}_p^T$ of Equation (4.23) can be expressed as

$$F_i = -\frac{\pi \bar{E}}{2} \varepsilon_y^B(\eta_i) \quad (4.25)$$

The solution for c can be determined from these linear algebraic equations. Once they are solved, the dynamic stress distribution caused by the layered piezoelectric structure can be determined as

$$\begin{Bmatrix} \sigma_y^{sc}(y, z) \\ \sigma_z^{sc}(y, z) \\ \tau_{yz}^{sc}(y, z) \end{Bmatrix} = [R]_p \{d\}_p \quad (4.26)$$

where $[R]_p$ is given by

$$\begin{aligned} R_{1j}(y, z) &= \int_0^\infty \frac{2s\beta}{\Delta} \left[(k^2 + 2\alpha^2) e^{-\alpha z} - (2s^2 - k^2) e^{-\beta z} \right] p_j^a(y) ds \\ R_{2j}(y, z) &= \int_0^\infty \frac{2s\beta}{\Delta} (2s^2 - k^2) (e^{-\beta z} - e^{-\alpha z}) p_j^a(y) ds \\ R_{3j}(y, z) &= \int_0^\infty \frac{4s^2\alpha\beta e^{-\alpha z} - (2s^2 - k^2)^2 e^{-\beta z}}{\Delta} q_j^a(y) ds \end{aligned} \quad (4.27)$$

with

$$\begin{aligned} p_j^a(y) &= (-1)^n J_j(sa) \begin{cases} \cos(sy) & j = 2n + 1 \\ (-1)\sin(sy) & j = 2n \end{cases} \\ q_j^a(y) &= (-1)^n J_j(sa) \begin{cases} \sin(sy) & j = 2n + 1 \\ \cos(sy) & j = 2n \end{cases} \end{aligned} \quad (4.28)$$

4.4 Scattered waves of a single crack

4.4.1 Elasto-dynamic behaviour of a crack in elastic medium

The i th crack is subjected to a pseudo incident wave, as discussed in section 4.2, and then a scattered wave will be generated, as shown in Fig. 4.2(b). The scattered wave can then be

obtained through solving the elasto-dynamic behaviour of the crack. The elasto-dynamic behaviour of a single crack in an elastic medium is well studied. We will use the Fourier transform and the dislocation density functions to solve the single crack problem. The main formulation for single crack modelling is summarized as follows.

The dynamic behaviour of the i th crack in the local coordinate system (y_i, z_i) can be described by the following dislocation density functions (Meguid and Wang, 1995).

$$\begin{aligned}\xi(y_i) &= \frac{\partial}{\partial y_i} \left[u_y(y_i, 0^+) - u_y(y_i, 0^-) \right], \\ \eta(y_i) &= \frac{\partial}{\partial y_i} \left[u_z(y_i, 0^+) - u_z(y_i, 0^-) \right].\end{aligned}\tag{4.29}$$

After using the continuity condition of σ_{zz} and τ_{yz} at $z_i = 0$, $A_r(s)$, $r=1,2,3,4$ can be determined and expressed in terms of the Fourier transform of dislocation density functions

$$\begin{aligned}A_1(s_i) &= -\frac{1}{k^2} \left(\bar{\xi} + \frac{\gamma}{2is_i\alpha} \bar{\eta} \right) \\ A_2(s_i) &= \frac{1}{k^2} \left(\bar{\xi} - \frac{\gamma}{2is_i\alpha} \bar{\eta} \right) \\ A_3(s_i) &= \frac{1}{k^2} \left(\bar{\eta} - \frac{\gamma}{2is_i\beta} \bar{\xi} \right) \\ A_4(s_i) &= -\frac{1}{k^2} \left(\bar{\eta} + \frac{\gamma}{2is_i\beta} \bar{\xi} \right)\end{aligned}\tag{4.30}$$

where $\gamma = 2s^2 - k^2$ and $\bar{\xi}(s_i)$, $\bar{\eta}(s_i)$ are the Fourier transform of $\xi(y_i)$, $\eta(y_i)$.

The dynamic displacement, strain and stress components can then be obtained and expressed as functions of $\bar{\xi}(s_i)$ and $\bar{\eta}(s_i)$ by substituting Equation (4.30) into Equations (4.15) to (4.17), respectively.

Without considering the contact of crack surfaces, the boundary conditions along the crack surface for a crack under an incident wave are

$$\begin{aligned}
\tau_{yz}(y_i,0)+\tau^I(y_i)=0, \quad \sigma_{zz}(y_i,0)+\sigma^I(y_i)=0, \quad |y_i|<c \\
u_y(y_i,0^+)-u_y(y_i,0^-)=0, \quad u_z(y_i,0^+)-u_z(y_i,0^-)=0, \quad |y_i|\geq c
\end{aligned}
\tag{4.31}$$

where $\tau^I(y_i)$, $\sigma^I(y_i)$ represent the shear and normal stress components along the crack surface induced by the incident wave, and $u_y(y_i,0^+)$, $u_y(y_i,0^-)$, $u_z(y_i,0^+)$, $u_z(y_i,0^-)$ are displacements of the scattered field in y and z directions on the upper and lower surfaces of the through-thickness of the crack.

By substituting Equations (4.15), (4.17) and (4.30) into (4.31), the governing equations for dynamic behaviour of a crack in elastic medium can be obtained as

$$\begin{aligned}
\int_{-c}^c \frac{\xi(w)}{w-y_i} dw + \int_{-c}^c \xi(w) \int_0^\infty \left[\frac{\gamma^2 - 4s^2\alpha\beta}{2(K^2 - k^2)s\beta} - 1 \right] \sin[s(w-y_i)] ds dw = -\frac{4\pi(1-\nu_s^2)}{E_s} \tau^I(y_i) \\
\int_{-c}^c \frac{\eta(w)}{w-y_i} dw + \int_{-c}^c \eta(w) \int_0^\infty \left[\frac{\gamma^2 - 4s^2\alpha\beta}{2(K^2 - k^2)s\alpha} - 1 \right] \sin[s(w-y_i)] ds dw = -\frac{4\pi(1-\nu_s^2)}{E_s} \sigma^I(y_i)
\end{aligned}
\tag{4.32}$$

and

$$\begin{aligned}
\int_{-c}^c \xi(w) dw = 0 \\
\int_{-c}^c \eta(w) dw = 0,
\end{aligned}
\tag{4.33}$$

from which the displacements of the crack surface can be determined.

4.4.2 Solution of the resulting integral equations

Since the resulting governing equation solutions involve square root singularity, these equations can be solved by expanding the dislocation density functions ξ and η in terms of Chebyshev polynomials as

$$\xi(w) = \sum_{j=0}^{\infty} d_j^1 \frac{T_j(w/c_i)}{\sqrt{1-w^2/c_i^2}}, \quad \eta(w) = \sum_{j=0}^{\infty} d_j^2 \frac{T_j(w/c_i)}{\sqrt{1-w^2/c_i^2}} \quad (4.34)$$

where T_j is the Chebyshev polynomial of the first kind with $T_j(\cos(\theta)) = \cos(j\theta)$ and d_j^1, d_j^2 are unknown constants to be determined. Equation (4.33) gives $d_0^1 = 0$ and $d_0^2 = 0$ according to the orthogonality conditions of the Chebyshev polynomials. By substituting Equation (4.34) into Equations (4.32) and (4.33), the governing equations will be transferred to algebraic equations for d_j^1 and d_j^2 .

An efficient way to determine the induced scattered wave (d_j^1, d_j^2) is to truncate the Chebyshev polynomials to the N th term, and to satisfy the resulting algebraic equations at N selected collocation points along the crack surfaces given by

$$y_l^l = c \cos\left(\frac{l-1}{N-1}\pi\right), \quad l=1,2, \dots, N \quad (4.35)$$

Then, the governing Equations (4.32) will be reduced to the following $2N$ linear algebraic equations, as organized in the matrix format as

$$[B]_{(2N \times 2N)} \{d\}_{(2N \times 1)} = \{F\}_{(2N \times 1)} \quad (4.36)$$

where

$$\{d\} = \{d_1^1, d_2^1, \dots, d_N^1, d_1^2, d_2^2, \dots, d_N^2\}^T \quad (4.37)$$

is a vector of coefficients of Chebyshev polynomials, and

$$\{F\} = \{\tau^l(y_i^1), \tau^l(y_i^2), \dots, \tau^l(y_i^N), \sigma^l(y_i^1), \sigma^l(y_i^2), \dots, \sigma^l(y_i^N)\}^T \quad (4.38)$$

is a vector of the stress components at the collocation points on crack surfaces induced by the incident wave, and

$$[B_{ij}]_{(2N \times 2N)} = \begin{bmatrix} f_j(y_i') & 0 \\ 0 & g_j(y_i') \end{bmatrix} \quad (4.39)$$

with

$$f_j(y_i') = -\frac{E_s}{4\pi(1-\nu_s^2)} \left\{ \frac{\sin[j \cos^{-1}(y_i')]}{\sin[\cos^{-1}(y_i')]} + c \int_0^\infty \left[\frac{\gamma^2 - 4s^2\alpha\beta}{2(k_L^2 - k_T^2)s\beta} - 1 \right] p_j^c(y_i') ds \right\}$$

$$g_j(y_i') = -\frac{E_s}{4\pi(1-\nu_s^2)} \left\{ \frac{\sin[j \cos^{-1}(y_i')]}{\sin[\cos^{-1}(y_i')]} + c \int_0^\infty \left[\frac{\gamma^2 - 4s^2\alpha\beta}{2(k_L^2 - k_T^2)s\alpha} - 1 \right] p_j^c(y_i') ds \right\}$$

and

$$p_j^c(y_i') = (-1)^n J_j(sc) \begin{cases} \cos(sy_i') & j = 2n + 1 \\ (-1)\sin(sy_i') & j = 2n \end{cases} \quad (4.40)$$

The $2N$ unknown coefficients $\{d\}$ can be found from the $2N$ linear algebraic equations in Equation (4.36). The scattered wave from a through-thickness crack can then be expressed in terms of constants $\{d\}$ by substituting solution of d_j^1 and d_j^2 into Equation (4.16), (4.17), (4.30) and (4.34),

$$\begin{bmatrix} \sigma_y^{sc}(y_i, z_i) \\ \sigma_z^{sc}(y_i, z_i) \\ \tau_{yz}^{sc}(y_i, z_i) \\ \varepsilon_y^{sc}(y_i, z_i) \\ \varepsilon_z^{sc}(y_i, z_i) \\ \varepsilon_{yz}^{sc}(y_i, z_i) \end{bmatrix} = [R(y_i, z_i)]_{(6 \times 2N)} \{d\}_{(2N \times 1)} \quad (4.41)$$

where

$$\begin{aligned}
R_{1j}(y_i, z_i) &= \begin{cases} \frac{\operatorname{sgn}(z_i) \bar{\lambda}_s c}{k^2} \int_0^\infty \left[(s^2 - \bar{v}_s \alpha^2) e^{-\alpha|z_i|} - (\alpha^2 - \bar{v}_s s^2) e^{-\beta|z_i|} \right] q_j^c(y_i) ds, & j = 1, 2, \dots \\ \frac{\bar{\lambda}_s c}{2k^2} \int_0^\infty \left[\frac{\gamma(\bar{v}_s \alpha^2 - s^2)}{s\alpha} e^{-\alpha|z_i|} - 2(1 - \bar{v}_s) s \beta e^{-\beta|z_i|} \right] p_{j-N}^c(y_i) ds, & j = N+1, \dots \end{cases} \\
R_{2j}(y_i, z_i) &= \begin{cases} -\frac{\operatorname{sgn}(z_i) \bar{\lambda}_s c}{k^2} \int_0^\infty \gamma (e^{-\alpha|z_i|} - e^{-\beta|z_i|}) q_j^c(y_i) ds, & j = 1, 2, \dots \\ -\frac{\bar{\lambda}_s (1 - \bar{v}_s) c}{4k^2} \int_0^\infty \left[\frac{\gamma^2}{\alpha s} e^{-\alpha|z_i|} - 4s\beta e^{-\beta|z_i|} \right] p_{j-N}^c(y_i) ds, & j = N+1, N+2, \dots \end{cases} \\
R_{3j}(y_i, z_i) &= \begin{cases} \frac{\mu_s c}{2k^2} \int_0^\infty \left[\frac{\gamma^2}{s\beta} e^{-\beta|z_i|} - 4s\alpha e^{-\alpha|z_i|} \right] p_j^c(y_i) ds, & j = 1, 2, \dots \\ \frac{\operatorname{sgn}(z_i) \mu_s c}{k^2} \int_0^\infty \gamma (-e^{-\alpha|z_i|} + e^{-\beta|z_i|}) q_{j-N}^c(y_i) ds, & j = N+1, N+2, \dots \end{cases} \\
R_{4j}(y_i, z_i) &= \begin{cases} -\frac{\operatorname{sgn}(z_i) c}{k^2} \int_0^\infty \left[s^2 e^{-\alpha|z_i|} - \frac{\gamma}{2} e^{-\beta|z_i|} \right] q_j^c(y_i) ds, & j = 1, 2, \dots \\ -\frac{c}{2k^2} \int_0^\infty \left[\frac{\gamma}{2\alpha} e^{-\alpha|z_i|} - \beta e^{-\beta|z_i|} \right] p_{j-N}^c(y_i) ds, & j = N+1, \dots \end{cases} \\
R_{5j}(y_i, z_i) &= \begin{cases} -\frac{\operatorname{sgn}(z_i) c}{k^2} \int_0^\infty \left(-\alpha^2 e^{-\alpha|z_i|} + \frac{\gamma}{2} e^{-\beta|z_i|} \right) q_j^c(y_i) ds, & j = 1, 2, \dots \\ -\frac{c}{k^2} \int_0^\infty \left[\frac{\gamma\alpha}{2s} e^{-\alpha|z_i|} + s\beta e^{-\beta|z_i|} \right] p_{j-N}^c(y_i) ds, & j = N+1, N+2, \dots \end{cases} \\
R_{6j}(y_i, z_i) &= \begin{cases} \frac{c}{2k^2} \int_0^\infty \left[\frac{\gamma^2}{s\beta} e^{-\beta|z_i|} - 4s\alpha e^{-\alpha|z_i|} \right] p_j^c(y_i) ds, & j = 1, 2, \dots \\ \frac{\operatorname{sgn}(z_i) c}{k^2} \int_0^\infty \gamma (-e^{-\alpha|z_i|} + e^{-\beta|z_i|}) q_{j-N}^c(y_i) ds, & j = N+1, N+2, \dots \end{cases}
\end{aligned} \tag{4.42}$$

with

$$\bar{\lambda}_s = \frac{E(1 - \nu_s)}{(1 - 2\nu_s)(1 + \nu_s)}, \quad \bar{v}_s = \frac{\nu_s}{1 - \nu_s}, \quad \mu_s = \frac{E_s}{2(1 + \nu_s)}$$

$$q_j^c(y_i) = (-1)^n J_j(sc) \begin{cases} \sin(sy_i) & j = 2n+1 \\ \cos(sy_i) & j = 2n \end{cases}$$

4.5 Dynamic interaction and multiple scattering of elastic waves

Based on the solutions for the sensor problem and the crack problem described in the sections 4.3 and 4.4, dynamic interaction of the piezoelectric sensor and cracks can be solved using the pseudo incident wave, as illustrated in section 4.2, which will integrate the coupled single sensor and single crack problem.

For the sensor problem, the piezoelectric sensor is subjected to the following pseudo incident wave

$$\{F^{ps}\}_p = \sum_{j=1}^n \{F^{sc}\}_{pj} + \{F^0\}_p \quad (4.43)$$

where $\{F^0\}_p$ and $\{F^{sc}\}_{pj}$ are resulting stress components along the sensor-host interface ($z = 0$) induced by the original incident wave and the scattered wave from the j th crack, respectively. From the analysis in Fig. 4.4, the shear stress $\{\tau_{pj}^{sc}\}$ and normal stress $\{\sigma_{pj}^{sc}\}$ at the collocation points along the sensor-host interface induced by the scattered wave from the j th crack are obtained as

$$\begin{aligned} \tau_{pj}^{sc}(y^l, 0) &= -\sigma_y^{sc}(\bar{y}_j, \bar{z}_j) \sin \varphi_{pj} \cos \varphi_{pj} + \sigma_\eta^{out}(\bar{y}_j, \bar{z}_j) \sin \varphi_{pj} \cos \varphi_{pj} + \tau_{\xi\eta}^{out}(\bar{y}_j, \bar{z}_j) \cos(2\varphi_{pj}) \\ \sigma_{pj}^{sc}(y^l, 0) &= \sigma_y^{sc}(\bar{y}_j, \bar{z}_j) \cos^2 \varphi_{pj} + \sigma_z^{sc}(\bar{y}_j, \bar{z}_j) \sin^2 \varphi_{pj} + \tau_{yz}^{sc}(\bar{y}_j, \bar{z}_j) \sin(2\varphi_{pj}) \end{aligned} \quad (4.44)$$

with

$$\begin{aligned} \bar{y}_j &= -d_{pj} \cos(\varphi_{pj} + \theta_{pj}) + y^l \cos \varphi_{pj} \\ \bar{z}_j &= d_{pj} \sin(\varphi_{pj} + \theta_{pj}) - y^l \sin \varphi_{pj} \end{aligned} \quad (4.45)$$

where y^l is the collocation points defined in Equation (4.35), d_{pj} are the distance between the centres of the piezoelectric sensor and the j th crack, θ_{pj} and φ_{pj} are the inclination and

orientation angles of the j th crack, as shown in Fig. 4.4. They can be obtained in the global coordinate as $d_{pj} = \sqrt{(y_j^c)^2 + (z_j^c)^2}$ and $\theta_{pj} = \arctan(-z_j^c / y_j^c)$. In these equations, σ_y^{sc} , σ_z^{sc} and τ_{yz}^{sc} are scattered wave due to the j th crack, and have been determined in the single crack scattering problem, as given in Equation (4.41)

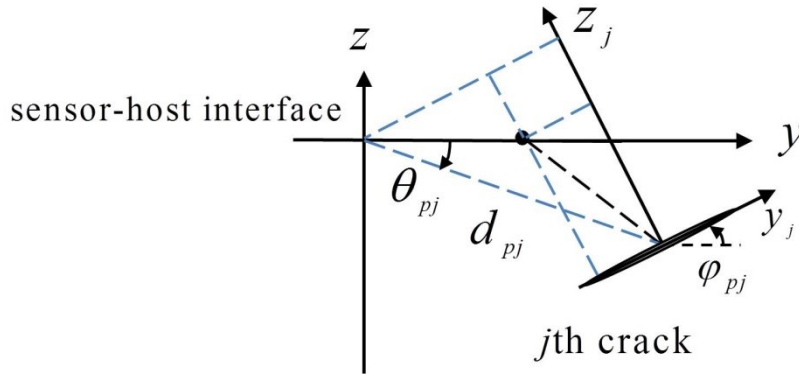


Fig. 4.4: The stress components at the sensor-host interface induced by the scattered wave from the j th crack

Then $\{F^{sc}\}_{pj}$ can be obtained by substituting Equation (4.26) into (4.44)

$$\{F^{sc}\}_{pj} = [T]_{pj} [R]_j \{d\}_j \quad (4.46)$$

where $[R]_j$ is the corresponding matrix $[R]$ in Equation (4.42) after replacing y, z by \bar{y}_j, \bar{z}_j ,

i.e. $[R]_j = [R(\bar{y}_j, \bar{z}_j)]$, and $[T]_{pj}$ is the coordinate transformation matrix, given by

$$[T]_{pj} = \begin{bmatrix} -\sin \varphi_{pj} \cos \varphi_{pj} & \sin \varphi_{pj} \cos \varphi_{pj} & \cos(2\varphi_{pj}) \\ \cos^2 \varphi_{pj} & \sin^2 \varphi_{pj} & \sin(2\varphi_{pj}) \end{bmatrix} \quad (4.47)$$

Therefore, for the piezoelectric sensor, the scattered wave can be determined from Equation (4.23), by replacing the incident wave as $\{F^{ps}\}_p$, such that

$$[B]_p \{d\}_p = \{F^{ps}\}_p \quad (4.48)$$

where $[B]_p$, $\{d\}_p$ and $\{F^{ps}\}_p$ are the corresponding matrix, Chebyshev polynomials coefficients and the pseudo incident wave of the sensor, which have been given in Equation (4.23) in the piezoelectric sensor problem.

The pseudo incident wave along the piezoelectric sensor-host structure interface is given in Equation (4.43). Therefore, the following algebraic equations can be obtained by substituting Equations (4.43), (4.46) into (4.48),

$$[B]_p \{d\}_p - \sum_{j=1}^n [T]_{pj} [R]_j \{d\}_j = \{F^0\}_p \quad (4.49)$$

For the crack problem, as shown in Fig. 4.2(b), crack i is subjected to an unknown incident wave F_i^{ps} which represents the superposition of the scattered waves from the piezoelectric sensor-host system, other cracks and the original incident wave. Therefore, the pseudo incident wave for crack i is

$$\{F^{ps}\}_i = \{F^{sc}\}_p + \sum_{\substack{j=1 \\ j \neq i}}^n \{F^{sc}\}_{ij} + \{F^0\}_i \quad (4.50)$$

where $\{F^0\}_i$, $\{F^0\}_p$ and $\{F^{sc}\}_{ij}$ are resulting stress components along the surface of the i th crack ($z_i = 0$) induced by the original incident wave, scattered wave from the piezoelectric sensor and the scattered wave from the j th crack ($j \neq i$), respectively. From the analysis in Fig. 4.5, the shear stress $\{\tau_{ij}^{sc}\}$ and normal stress $\{\sigma_{ij}^{sc}\}$ on the surface of the i th crack due to the scattered wave from the j th crack are obtained

$$\begin{aligned}\tau_{ij}^{sc}(y_i^l) &= \left[-\sigma_y^{sc}(\bar{y}_j, \bar{z}_j) + \sigma_z^{sc}(\bar{y}_j, \bar{z}_j) \right] \sin \varphi_{ij} \cos \varphi_{ij} + \tau_{yz}^{sc}(\bar{y}_j, \bar{z}_j) \cos(2\varphi_{ij}) \\ \sigma_{ij}^{sc}(y_i^l) &= \sigma_y^{sc}(\bar{y}_j, \bar{z}_j) \sin^2 \varphi_{ij} + \sigma_z^{sc}(\bar{y}_j, \bar{z}_j) \cos^2 \varphi_{ij} - \tau_{yz}^{sc}(\bar{y}_j, \bar{z}_j) \sin(2\varphi_{ij})\end{aligned}\quad (4.51)$$

with

$$\begin{aligned}\bar{y}_j &= d_{ij} \cos \theta_{ij} + y_i^l \cos \varphi_{ij} \\ \bar{z}_j &= -d_{ij} \sin \theta_{ij} + y_i^l \sin \varphi_{ij}\end{aligned}\quad (4.52)$$

where y_i^l is the collocation points defined in Equation (4.35), d_{ij} are the distance between the centres of the i th and j th crack, θ_{ij} are the inclination angles and φ_{ij} are the orientation angles of the i th crack, as shown in Fig. 4.5. They are obtained in the global coordinate as $d_{ij} = \sqrt{(y_i^c - y_j^c)^2 + (z_i^c - z_j^c)^2}$, $\theta_{ij} = \arctan[(z_i^c - z_j^c)/(y_i^c - y_j^c)]$ and $\varphi_{ij} = \phi_i - \phi_j$ (ϕ_i, ϕ_j are the orientations of the i th crack and the j th crack in the global coordinate, respectively). In these equations, σ_y^{sc} , σ_z^{sc} and τ_{yz}^{sc} are that of scattered field due to j th crack, and have been determined in the single crack scattering problem, as given in Equation (4.41)

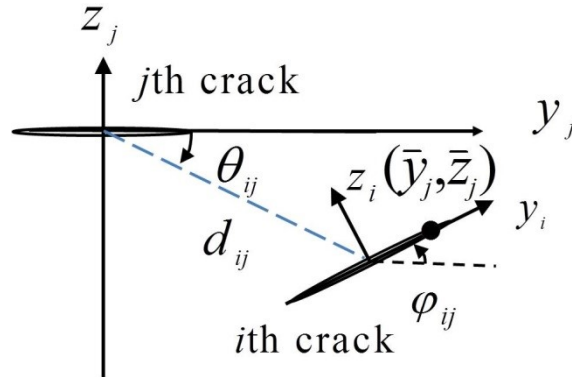


Fig. 4.5: The stress components on the surfaces of the i th crack due to the scattered wave from the j th crack

Therefore, $\{F^{sc}\}_{ij}$ can be obtained by substituting Equation (4.41) into (4.51) as

$$\{F^{sc}\}_{ij} = [T]_{ij} [R]_j \{d\}_j \quad (4.53)$$

where $[R]_j$ is the corresponding matrix $[R]$ in Equation (4.42) after replacing y, z by \bar{y}_j, \bar{z}_j ,

i.e. $[R]_j = [R(\bar{y}_j, \bar{z}_j)]$, and $[T]_{ij}$ is the coordinate transformation matrix, given by

$$[T]_{ij} = \begin{bmatrix} -\sin \varphi_{ij} \cos \varphi_{ij} & \sin \varphi_{ij} \cos \varphi_{ij} & \cos(2\varphi_{ij}) \\ \sin^2 \varphi_{ij} & \cos^2 \varphi_{ij} & -\sin(2\varphi_{ij}) \end{bmatrix}. \quad (4.54)$$

Similarly, the shear stress $\{\tau_{ip}^{sc}\}$ and normal stress $\{\sigma_{ip}^{sc}\}$ on the surface of the i th crack induced by the scattered wave from the piezoelectric sensor can be determined from Equation (4.53) by replacing the subscript j by p as

$$\{F^{sc}\}_{ip} = [T]_{ip} [R]_p \{d\}_p. \quad (4.55)$$

The scattered wave of the i th crack, when it is subjected to the pseudo incident wave, can be determined from Equation (4.36), by replacing the incident wave with $\{F_i^{ps}\}$ in the single crack solution

$$[B]_i \{d\}_i = \{F_i^{ps}\} \quad (4.56)$$

where $[B]_i$, $\{d\}_i$ and $\{F_i^{ps}\}$ are the corresponding matrices, Chebyshev polynomials coefficients and the pseudo incident wave of the i th crack, which have been given in Equation (4.36) in the single crack problem.

The pseudo incident wave along the surfaces of the i th crack is given by Equation (4.50). Therefore, the following algebraic equations can be obtained by substituting Equations (4.50), (4.53) into (4.56),

$$[B]_i \{d\}_i - [T]_{ip} [R]_p \{d\}_p - \sum_{\substack{j=1 \\ j \neq i}}^n [T]_{ij} [R]_j \{d\}_j = \{F^0\}_i \quad (4.57)$$

For the dynamic interactions between a piezoelectric sensor and n cracks, a linear system of equations of the Chebyshev polynomial coefficients can be determined by combining Equations (4.49) and (4.57) as

$$\begin{bmatrix} [B]_p & -[T]_{p1}[R]_1 & -[T]_{p2}[R]_2 & \cdots & -[T]_{pn}[R]_n \\ -[T]_{1p}[R]_p & [B]_1 & -[T]_{12}[R]_2 & \cdots & -[T]_{1n}[R]_n \\ -[T]_{2p}[R]_p & -[T]_{21}[R]_1 & [B]_2 & \cdots & -[T]_{2n}[R]_n \\ \vdots & \vdots & \vdots & \ddots & \vdots \\ -[T]_{np}[R]_p & -[T]_{n1}[R]_1 & -[T]_{n2}[R]_2 & \cdots & [B]_n \end{bmatrix} \begin{Bmatrix} \{d\}_p \\ \{d\}_{11} \\ \{d\}_{22} \\ \vdots \\ \{d\}_n \end{Bmatrix} = \begin{Bmatrix} \{F^0\}_p \\ \{F^0\}_{11} \\ \{F^0\}_{22} \\ \vdots \\ \{F^0\}_n \end{Bmatrix} \quad (4.58)$$

where $\{F^0\}_i$ ($i=p,1,2, \dots, n$) are the vectors representing the stress components at the piezoelectric sensor-host interface ($i=p$) and at the surfaces of the i th crack due to the original incident wave, $[B]_i$ ($i=p,1,2, \dots, n$) are the coefficient matrices of the single piezoelectric sensor problem ($i=p$) or single crack problem, and $[T]_{ij}[R]_j$ ($i=p,1,2, \dots, n$) represent the effect of the j th crack upon the piezoelectric sensor ($i=p$) or the i th crack.

The Chebyshev polynomial coefficients can be found through solving Equation(4.58). Then the stress and strain of the wave field in the structures can be calculated directly.

4.6 Results and discussion

The dynamic interactions among multiple cracks in piezoelectric based SHM systems are dominated by the linear algebraic Equations (4.58). By solving the system of equations, the Chebyshev polynomial coefficients are determined, and all displacement, strain and stress components can then be obtained. In this section, firstly, the current model will be compared

with existing results, followed by the multiple scattering of elastic wave among multiple cracks, and the dynamic interaction between sensors and cracks will be studied.

In the solution of the problem, based on the careful evaluation of the convergence of Chebyshev polynomial expansion, 20 terms of Chebyshev polynomials are used in the numerical calculation, which ensures that the current results considered are convergent.

The incident wave considered is a time-harmonic longitudinal plane wave

$$\begin{aligned}\sigma_y^0 &= \sigma_m (1 - 2\kappa^2 \sin^2 \Gamma) \exp[-ik(y \cos \Gamma + z \sin \Gamma)] \\ \sigma_z^0 &= \sigma_m (1 - 2\kappa^2 \sin^2 \Gamma) \exp[-ik(y \cos \Gamma + z \sin \Gamma)] \\ \tau_{yz}^0 &= \sigma_m \kappa^2 \sin(2\Gamma) \exp[-ik(y \cos \Gamma + z \sin \Gamma)]\end{aligned}\quad (4.59)$$

where σ_m is the maximum amplitude of the normal stress corresponding to the incident wave front, Γ is the angle angel with the y -axis, K is the longitudinal wave number and

$$\kappa^2 = \frac{1 - 2\nu_s}{2(1 - \nu_s)}.$$

4.6.1 Comparison with existing results

To the best of authors' knowledge, there are no works on multiple scattering of elastic waves between surface bonded piezoelectric sensors and multiple cracks, however, there are some simpler related cases, such as the dynamic behaviour of a surface bonded piezoelectric sensor (Congrui Jin and Wang, 2011; Wang and Huang, 2006b) and the dynamic interaction of cracks (Meguid and Wang, 1995). These simpler cases are studied using the current solution and compared with the existing results in Congrui Jin and Wang (2011) and Meguid and Wang (1995).

Comparison is first made to a single piezoelectric sensor problem solved by Jin and Wang (2011), by using only the first row in Equation (4.58), i.e.

$$[B]_p \{d\}_p = \{F^0\}_p. \quad (4.60)$$

The material properties of the piezoelectric sensor are given in Table 2.1. Meanwhile, the material properties of the host structures are $2.74 \times 10^{10} Pa$ for Young's modulus, 0.3 for Poisson's ratio and $2700 Kg / m^3$ for the mass density. The mass density of the piezoelectric sensor is also assumed as $2700 Kg / m^3$.

The dynamic strain ratio is “the percentage of deformation transferred from the host medium to the sensor” (Huang and Wang, 2006). It is an index of the sensing characteristics of the piezoelectric sensor. It is defined as

$$\kappa_y(y) = \varepsilon_y(y) / \varepsilon_y^0(y) \quad (4.61)$$

where $\varepsilon_y^0(y)$ is the resulting strain on the free surface of the host structure. In general, $\kappa_y(y)$ is in the complex form. The resulting dynamic strain ratio studied in this chapter is the real part of $\kappa_y(y)e^{-i\omega t}$.

Fig. 4.6 shows the amplitude of the dynamic strain ratio along the sensor under different loading frequencies when the sensor system is subjected to a normal incident wave with K being the longitudinal wave number. Very good agreement are observed, which validating the current model and program of the piezoelectric sensor problem.

The results of the current model are then compared with that of interacting crack problems, which have been extensively studied using numerical methods, such as FEM or BEM, and analytical methods (Achenbach, 1973; Meguid and Wang, 1995). Meguid and Wang (1995) developed a semi-analytical model to determine the dynamic interaction of two cracks using the superposition of a series of the analytical solution of a single crack. This

method solved the multiple scattering of elastic waves back and forth between two cracks by using a number of iterations of scattering wave from a single crack to convergence.

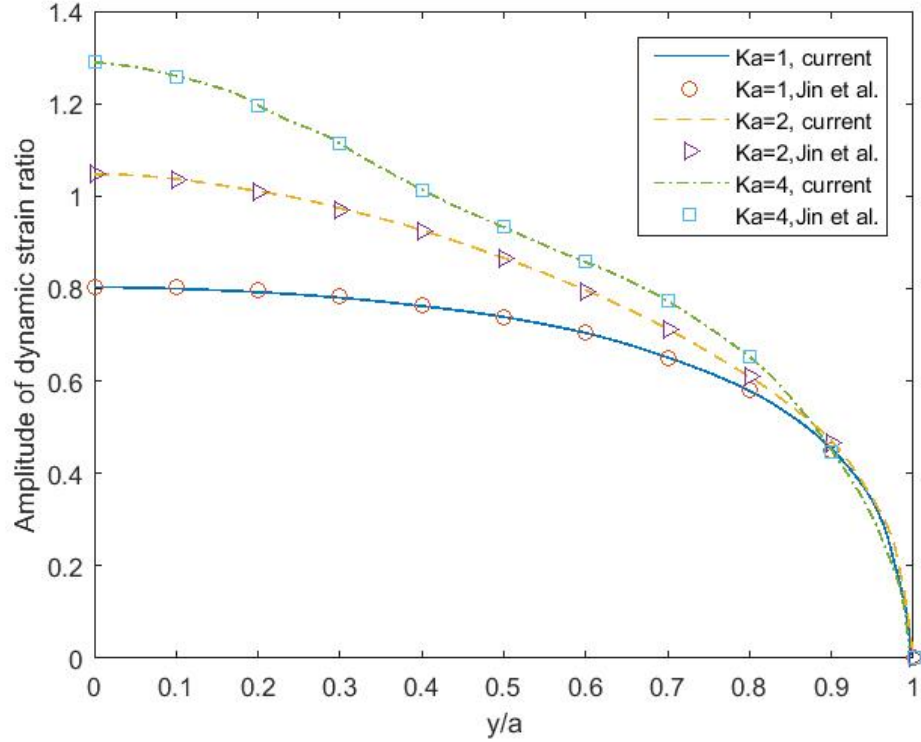


Fig. 4.6: The amplitude of the dynamic strain ratio along the sensor under different loading frequencies.

In the current method, the dynamic stress intensity factors (SIF) of the i th crack can be expressed in terms of Chebyshev polynomials coefficients $\{d\}_i$ as

$$\begin{aligned}
 K_I^{R_i} &= -\frac{E}{4(1-\nu^2)} \sqrt{\pi c_i} \sum_{j=1}^N d_{ij}, & K_I^{L_i} &= -\frac{E}{4(1-\nu^2)} \sqrt{\pi c_i} \sum_{j=1}^N (-1)^j d_{ij}, \\
 K_{II}^{R_i} &= -\frac{E}{4(1-\nu^2)} \sqrt{\pi c_i} \sum_{j=1}^N c_{ij}, & K_{II}^{L_i} &= -\frac{E}{4(1-\nu^2)} \sqrt{\pi c_i} \sum_{j=1}^N (-1)^j c_{ij},
 \end{aligned} \tag{4.62}$$

where $K_I^{R_i}$, $K_{II}^{R_i}$ and $K_I^{L_i}$, $K_{II}^{L_i}$ are the dynamic SIFs at the right and the left tips of the i th crack, respectively.

To evaluate the accuracy of the current method for simplified case without sensors, the dynamic SIFs of two collinear cracks are determined and compared to the existing results. Fig. 4.7 shows the comparison between the results from the current model and that from Meguid and Wang (1995) for different loading frequencies (kc) and different c_2/c_1 values. In this figure, the normalized SIF is defined as $K_I^* = K_I^{R_1} / K_I^{static}$ with K_I^{static} being the static SIF of a single crack and kc being the normalized wave number. The interaction between two collinear cracks is studied, with Poisson's ratio being $\nu = 1/3$, the half-length of the first crack being c_1 , the centre-to-centre distance being $d = 2.2c_1$, and the half-length of the second crack c_2 being allowed to vary. The interacting cracks are subjected to a normal incident wave propagating perpendicularly to the cracks, given in Equation (4.59).

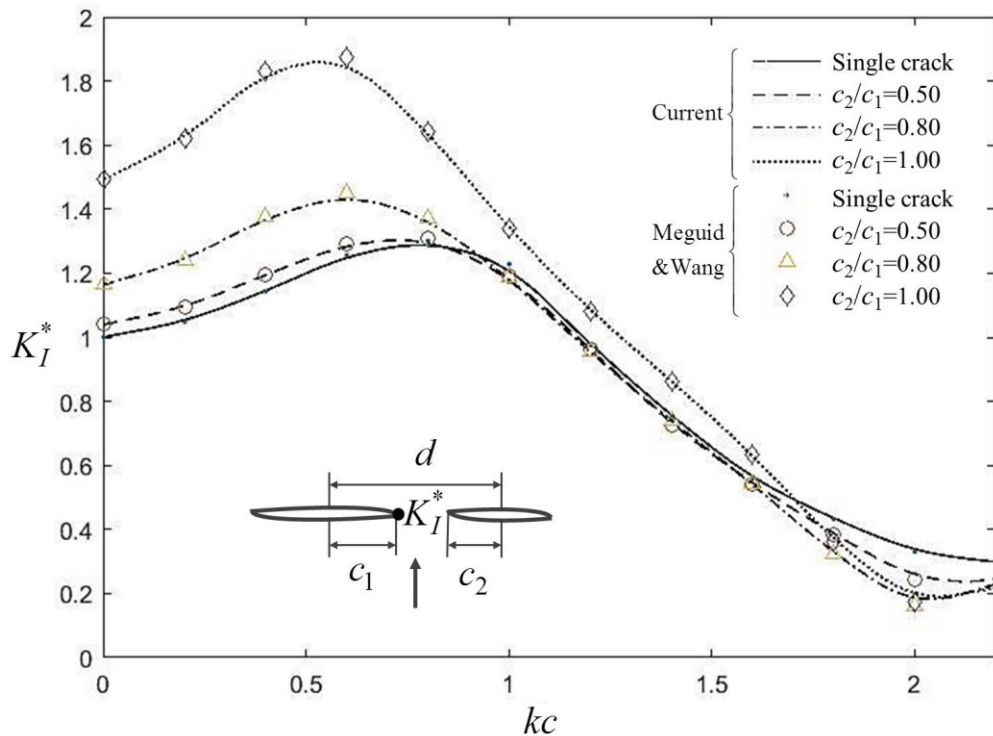


Fig. 4.7: Variation of normalized dynamic SIFs versus kc for different lengths of a collinear crack induced by a normal incident wave.

The results showed a very good agreement with the result of Meguid and Wang (1995). The good agreement verifies that the current solution can predict the wave fields reliably and accurately caused by the dynamic interaction between cracks.

4.6.2 Dynamic interaction between piezoelectric sensors and cracks

The dynamic interactions among cracks in piezoelectric based SHM systems are dominated by a system of linear algebraic Equations (4.58). By solving these equations, the voltage output can be determined. This section will focus on analyzing the voltage output of the piezoelectric smart sensor, which can be used as the surface signals for crack identification. The material properties used in this section are same as that given in section 4.6.1.

The current method can be reduced to solving dynamic interaction of multiple cracks in an infinite medium. The SIFs can be determined from Equation (4.62) after determining all Chebyshev polynomial coefficients, which are the solutions of Equation (4.58) after eliminating first row and column. Because this problem of interacting multiple cracks has been solved by Meguid and Wang (1995), therefore, except the SIFs of two collinear cracks with difference lengths shown in Fig. 4.7 for comparison, other results of interacting only multiple cracks determined by the current method are given in Appendix C.

Based on the constitutive equations of piezoelectric materials, the voltage output $V(y)$ along the sensor can be expressed as (Jin and Wang, 2011)

$$V(y) = -\int_0^h E_z(y) dz = \frac{eh}{\lambda} \varepsilon_y \quad (4.63)$$

where ε_y is the axial strain along the piezoelectric sensor and

$$e = e_{13} - e_{33}c_{13} / c_{33}, \quad \lambda = \lambda_{33} + e_{33}^2 / c_{33}$$

with c_{ij} being the stiffness coefficients, e_{ij} being the piezoelectric constants, and λ_{ij} being the dielectric constants. It is noted that the voltage output determined is in the complex form, and only the amplitudes are considered in the current analysis.

The voltage output of the piezoelectric smart sensor may be affected by embedded cracks in the structure, and contains the information of crack parameters. To illustrate the effect of a crack upon the voltage output, specific results with and without cracks subjected to a normal incident wave are compared and plotted in Fig. 4.8, which show the results under a dynamic loading (normalized wave number $Ka=1$ with K and a being the longitudinal wave number and half-length of the piezoelectric sensor). The crack is parallel to the piezoelectric sensor with its length being equal to that of the sensor and the distance between the sensor and the crack being $a/2$. The voltage output of the piezoelectric sensor is normalized by dividing $V_{\max} = eh \max(\varepsilon_y) / \lambda$ with $\max(\varepsilon_y)$ representing the maximum strain induced by the incident wave ($Ka=1$ for Fig. 4.8) for the structure without any cracks. For the case of $Ka=1$, the voltage output is affected significantly by the existence of the embedded crack. The voltage outputs under different frequencies are studied and shown in Fig. 4.9. The voltage output is normalized by dividing the maximum voltage for the static case without any cracks. For the case with a crack, the incident wave is scattered from both the crack and the sensor, so the wave propagation involves multiple scattering and will be very complicated. The wave field and the voltage output from the sensor depend on loading frequencies and crack characteristics. The current model will enable the description of such a complicated wave field and the final voltage output for different configurations.

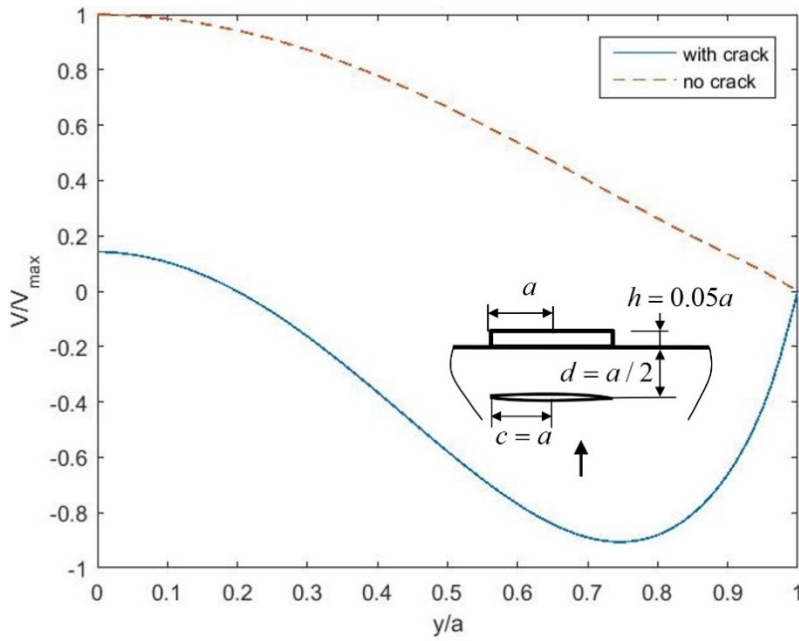


Fig. 4.8: Comparison of voltage output along the piezoelectric sensor surface for none crack case and with crack case under a dynamic load ($Ka=1$).

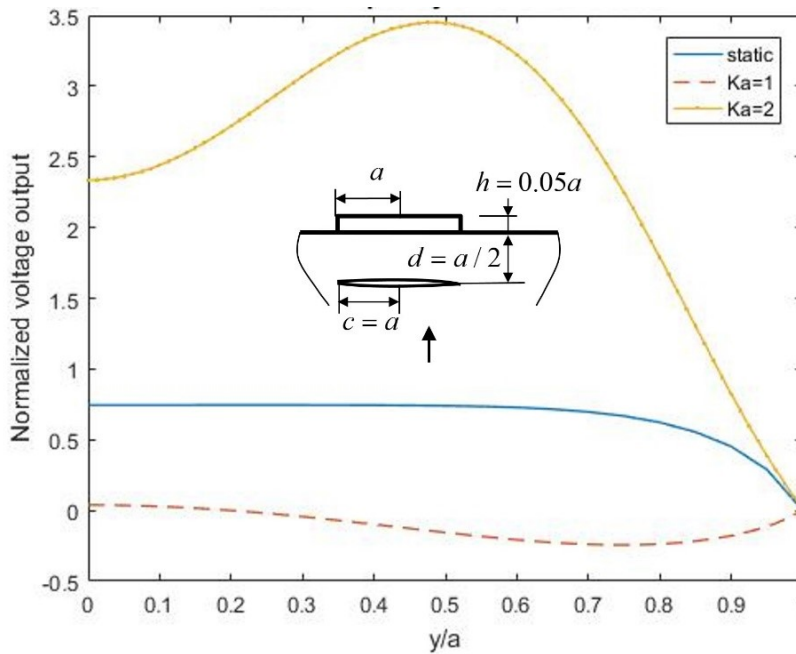


Fig. 4.9: Comparison of voltage output along the piezoelectric sensor surface for different loading frequencies.

In summary, the voltage output of the piezoelectric sensor in response to embedded cracks can be determined, which contains the information of crack parameters. This result can then be used to identify embedded crack from known sensor signals, i.e. the recorded voltage data of surface bonded piezoelectric sensor.

The sensor response to multiple cracks is also studied for the case of $Ka=2$, under a normal incident wave. Three collinear cracks are distributed uniformly with the same half-length being $a/4$ and the distance between the sensor and the cracks being $a/2$, as shown in Fig. 4.10. The voltage output is shown in Fig. 4.10. The voltage is normalized by the voltage value of the one crack configuration at the centre of the piezoelectric sensor. From the figure, the voltage output for these two configurations is significantly different along the sensor surface. The amplitude for three crack configuration is higher than the one crack configuration. Therefore, the difference in the crack configurations can be distinguished from the voltage output of the sensor. It should be mentioned that the three collinear cracks occupy the same length as the single crack.

Piezoelectric element, as an inhomogeneity of the structure, may affect the fracture behaviour of near cracks. The dynamic SIFs of cracks can also be obtained from the method directly. Fig. 4.11 shows the variation of normalized dynamic SIFs versus ka for different locations of a parallel crack induced by a normal incident wave. Comparison with the corresponding SIF of a single crack in an infinite medium is also provided. When the distance between the piezoelectric element and the crack is small ($d=0.1$ for example), there is a significant difference between the current dynamic SIF and that for the single crack case. As expected, the difference will be reduced with the increase of the distance.

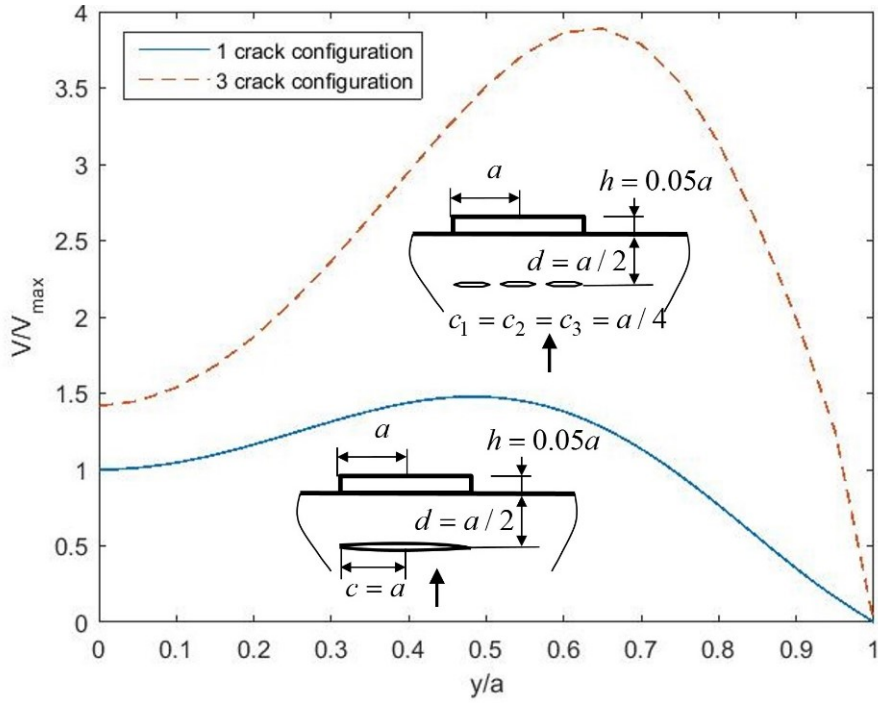


Fig. 4.10: Comparison of voltage output along the piezoelectric sensor surface for one crack configuration and three crack configuration under a dynamic load ($Ka=2$).

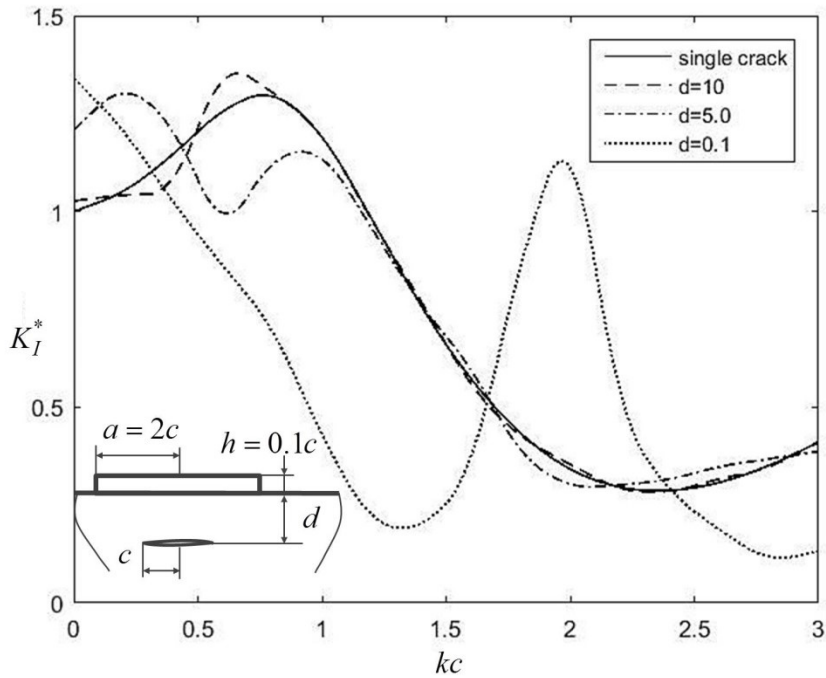


Fig. 4.11: Variation of normalized dynamic SIFs versus ka for different locations of a parallel crack induced by a normal incident wave.

4.7 Conclusions

A semi-analytical methodology is presented to simulate the complicated dynamic interaction among cracks in a piezoelectric smart structure under plane elastic wave loading using the pseudo incident wave method and proper superposition technique. Through this method, the complicated multiple scattering problem is reduced to the coupled solution of the single crack problem and the single piezoelectric sensor problem. The resulting integral governing equations for both are solved using Chebyshev polynomials. The main contribution of this chapter is the development of explicit forms of the voltage output of the piezoelectric sensor and dynamic SIFs of cracks by solving the complicated dynamic interaction problem. The method is compared with the existing results of simplified cases. Numerical results of the voltage output and the dynamic SIFs for different configurations and frequencies are determined and analyzed. The loading frequency shows complicated effects on the voltage output of the sensor, which depends on the crack characteristics. For specific crack configuration, certain frequencies can be used to generate more significant voltage output which can potentially be used for crack identification. The current method is very general and can reliably simulate the complicated interaction between piezoelectric sensors and cracks.

Chapter 5: A novel crack identification technique using optimization methods

In the previous chapter, the wave propagation by interacting the cracks and the piezoelectric sensor can be determined, and the surface voltage signals and interface stress can be obtained theoretically, which related the surface signals with the crack characteristics. Inversely, the unknown parameters of cracks, including the sizes, shapes and locations, can be determined through the obtained surface signals by integrating the relation into an optimization process. This chapter will study a novel crack detection technique using the surface signals determined from piezoelectric smart sensors based on an optimization method. Numerical examples will be given to demonstrate the accuracy and evaluate the effectiveness of the current approach.

5.1 Introduction

In a typical structural health monitoring system, piezoelectric sensors can be used to measure the scattered waves, and the recorded signals contain the health signatures of the embedded cracks which will be useful for estimating their parameters. One of the most fundamental issues in such a crack identification system is the extraction of crack information from the measured signals precisely. Four methods to interpret the surface signals have been summarized and compared in the literature review analysis in Section 1.2.4, including comparing feature parameters between damaged and undamaged structures (Schulz et al., 1999), scanning method (Hoseini et al., 2013), time-reversal technique (Meng et al., 2006)

and optimization methods (De Fenza et al., 2015). An effective way to identify cracks is to use a traditional optimization process based on theoretical solutions of sensor response to different crack configurations, which has been studied in the previous chapter. Through the comparison, the optimization scheme will be conducted to determine the length, the positions and orientations of the embedded cracks using known surface signals of piezoelectric smart sensors.

The relation between crack parameters and the scattered field has been integrated into an optimization algorithm to predict unknown crack parameters by Bao and Wang (2009, 2011). Bao and Wang (2009) presented a framework to identify a crack in an infinite elastic medium subjected to a longitudinal incident wave using BFGS algorithm with the known strains of the scattered elastic waves, and then multiple cracks detection was conducted following the same process in their later work (Bao and Wang, 2011). In their works, the known strains used to identify crack parameters were around the cracked area, which is impracticable for industrial application. Meanwhile, their simulation results ignored the effects of sensors upon the signals, but per our results in Section 4.6.2, the sensors will have a significant influence on the scattered wave field due to the interaction between the cracks and sensors.

This project will study the quantitative crack identification using traditional optimization scheme based on known voltage output from surface bonded piezoelectric sensors. The voltage output of the piezoelectric sensor in response to unknown crack parameters will be simulated using the solution developed in previous chapter for specific crack configurations. The position, the length and the orientation of embedded cracks will

then be estimated through minimizing the difference of the known voltage output and that determined in the developed interacting sensor/crack solution.

5.2 Formulation of the problem

A piezoelectric smart sensor with uniform thickness h and half-length a is surfaced attached to an isotropic and elastic host structure, in which cracks may be embedded, as shown in Fig. 5.1. It is assumed that the poling direction of the piezoelectric sensor is along the z -axis, perpendicular to the x - y plane. The host structure can be idealized as a semi-infinite plane which corresponding to the case that cracks are far from the lower boundaries. To describe the structure, a Cartesian coordinate system (y, z) is illustrated in Fig. 5.1, and n local Cartesian systems (y_i, z_i) , $i = 1, 2, \dots, n$ are used to characterize the coordinates of the crack i . The unknown parameters for the i th crack are assumed to be c_i for half lengths, ϕ_i for the orientation angles and (y_i^c, z_i^c) for the location in the global Cartesian coordinate.

The problem investigated is to identify the unknown crack characteristics through the known voltage signals from the piezoelectric smart sensor when the structure is subjected a time-harmonic incident wave. Two tasks will be conducted. One is the direct problem and the sensitivity analysis of the solution, which determines the dynamic response of the structures (the voltage output of the piezoelectric sensor) when the excitation loading, structural constants and the crack parameters are known. The other one is the inverse problem to identify the crack parameters using the known voltage output. In the current study, the voltage output of the sensor will be numerical simulated using the solution developed in the previous chapter.

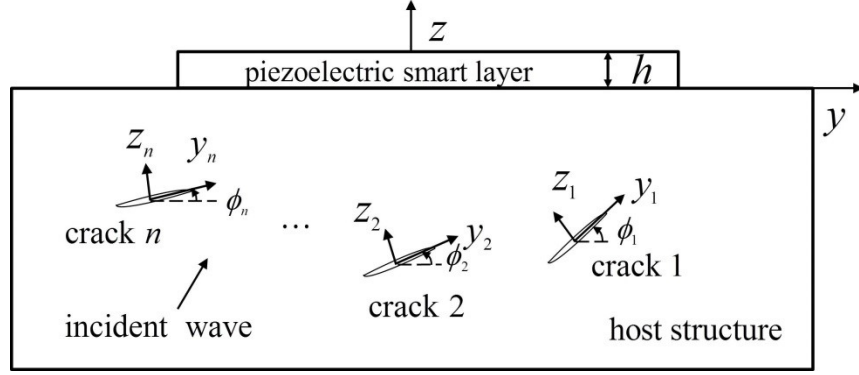


Fig. 5.1: General schematics of the piezoelectric sensor systems for embedded crack identification.

5.2.1 The direct problem

The direct problem is to simulate the voltage output along the piezoelectric smart sensor in response to specific embedded cracks under a time harmonic loading. Chapter 4 has provided an effective and accurate semi-analytical model for dealing with the dynamic interaction among piezoelectric sensors and embedded cracks using the PsIW method. This model will be used in the current section to related the voltage output of the piezoelectric sensor to crack parameters.

Based on the constitutive equations of piezoelectric materials (Jin and Wang, 2011), the voltage output $V(y)$ along the sensor in open-loop condition can be expressed as

$$V(y) = -\int_0^h E_z(y) dz = \frac{eh}{\lambda} \varepsilon_y \quad (5.1)$$

where ε_y is the axial strain along the piezoelectric sensor and

$$e = e_{13} - e_{33}c_{13} / c_{33}, \quad \lambda = \lambda_{33} + e_{33}^2 / c_{33}$$

with c_{ij} being the stiffness coefficients, e_{ij} being the piezoelectric constants, and λ_{ij} being the dielectric constants.

The axial strain of the piezoelectric sensor is controlled by the interfacial stress transferred from the host structure to the sensor $\tau(y)$, as given in Equation (4.8), as

$$\begin{aligned} \varepsilon_y(y) = & \frac{\sin k_p(a+y)}{hE_p \sin 2k_p a} \int_{-a}^a \cos k_p(\zeta-a) \tau(\zeta) d\zeta \\ & - \int_{-a}^y \cos k_p(\zeta-y) \frac{\tau(\zeta)}{hE_p} d\zeta, \quad |y| < a \end{aligned} \quad (5.2)$$

where k_p and c_p represent the wave number and the axial wave velocity in the piezoelectric layer, with $k_p = \omega / c_p$ and $c_p = \sqrt{E_p / \rho}$.

According to the solution in Chapter 4, the interfacial shear stress $\tau(y)$ can be determined by the following Chebyshev expansions,

$$\tau(y) = \sum_{j=1}^N d_j T_j(\eta^l) / \sqrt{1-(\eta^l)^2} \quad (5.3)$$

where d_j are Chebyshev polynomials coefficients, T_j is the Chebyshev polynomials of the first kind with $T_j(\cos \theta) = \cos(j\theta)$, and η^l are the locations of N selected collocation points along the piezoelectric sensor-host structure interface with

$$\eta^l = y^l / a = \cos\left(\frac{l-1}{N-1} \pi\right), \quad l=1,2,\dots,N. \quad (5.4)$$

For specific loading conditions and crack geometries, the Chebyshev polynomial coefficients $\{d\}_p$ can be determined using the solution obtained in the previous Chapter, Equation (4.58). The interfacial shear stress $\tau(y)$ and voltage output $V(y)$ along the piezoelectric smart sensor can then be obtained.

This section summarizes the relation between the voltage output of the sensor and the crack parameters. In this problem, each potential crack has four crack parameters. These four parameters of the i th crack are denoted as

$$\mathbf{p}_i = (p_{4(i-1)+1}, p_{4(i-1)+2}, p_{4(i-1)+3}, p_{4i})^T \quad (5.5)$$

with $p_{4(i-1)+1} = c_i$, $p_{4(i-1)+2} = \phi_i$, $p_{4(i-1)+3} = y_i^c$, $p_{4i} = z_i^c$ being the half length, the orientation and two position coordinates of the crack centre in the global Cartesian coordinate. For a specific structure attached with a known piezoelectric smart sensor under a given time harmonic loading, the resulting voltage output is only determined by the crack parameters \mathbf{p} , i.e.

$$V(y) = V_f(\mathbf{p}) \quad (5.6)$$

where $\mathbf{p} = \{p_1, p_2, p_3, p_3, \dots, p_{4n-1}, p_{4n}\}^T$ with $p_1 = c_1$, $p_2 = \phi_1$, $p_3 = y_1^c$, $p_4 = z_1^c$, \dots , $p_{4n-1} = y_n^c$, $p_{4n} = z_n^c$. The solution of the direct problem is a predictor or solver, through which the theoretical solution of resulting voltage output can be obtained if the crack parameters are given.

5.2.2 Sensitivity analysis

For the direct problem, the inputs are the crack parameters and the outputs are the voltage data of the piezoelectric sensor. In the current chapter, the sensitivity analysis is adopted to evaluate the variation of the voltage output at selected points along the piezoelectric sensor with the change of positions, lengths and orientations of every crack. Mathematically, sensitivity analysis is equivalent to evaluating the partial derivative of the voltage output with respect to crack parameters. The results of the sensitivity analysis will be used to determine the gradient vector and the Hessian matrix to determine the searching direction in the optimization iteration.

In this problem, each potential crack has four crack parameters, one length parameter, two position coordinates, one orientation. For a case where n cracks might exist, a total of $4n$

parameters need to be identified. The sensitivity can be obtained by determining the partial derivative of the voltage output function with respect to each parameter. However, the direct differentiation is difficult to determine because the formulation of the voltage output function is very complicated. Therefore, the finite difference approximation is used to provide simpler and more convenient way of calculating local sensitivity. It requires no extra code beyond the original model solver.

In general, the crack parameters are represented as a vector given in Equation (5.5). The first and second order derivative of voltage output with respect to the crack parameter p_i can be mathematically formulated by

$$\begin{aligned}\frac{\partial V}{\partial p_i} &= \frac{V_f(p_i + \delta) - V_f(p_i - \delta)}{2\delta}, \\ \frac{\partial^2 V}{\partial p_i^2} &= \frac{V_f(p_i + \delta) - 2V_f(p_i) + V_f(p_i - \delta)}{\delta^2}, \\ &(i = 1, 2, \dots)\end{aligned}\tag{5.7}$$

where $V_f(p_i + \delta)$, $V_f(p_i)$ and $V_f(p_i - \delta)$ are the corresponding voltage output for crack parameter $p_i + \delta$, p_i and $p_i - \delta$ respectively with δ being a small disturbance value, which will be identified later.

Using these equations, the sensitivity of the voltage output to every parameter of every crack can be determined.

5.2.3 The inverse problem

The relation between crack characteristics and the voltage output has been obtained by solving the direct problem. This relation between signals and crack parameters can be integrated into an optimization algorithm to predict the cracks parameters from known voltage output along the sensor. The crack parameters, including the length, orientation and

locations, can be identified by minimizing the distance between the known voltage data and corresponding voltage predicted by the direct problem. If this distance is defined as an objective function $f(\mathbf{p})$, the inverse problem is to then determine crack parameters \mathbf{p} which minimize the objective function, i.e.

$$\min f(\mathbf{p}) = \frac{1}{2} \sum_{f=1}^{n_p} \sum_{q=1}^{n_\omega} \|V_f(\mathbf{p}, \omega_q) - \bar{V}_f(\omega_q)\|^2 \quad (5.8)$$

where $\bar{V}_f(\omega_q)$ is the known voltage output at n_p selected points along the sensor described by $y_i, i=1,2,\dots,n_p$ in response to embedded cracks and loading frequency ω_q , n_p is the number of selected points, n_ω is the number of frequencies, and $V_f(\mathbf{p}, \omega_q)$ is the surface voltage output along the sensor obtained through the direct problem for the crack parameters \mathbf{p} and the frequency ω_q .

In the current study, proper initial values of crack parameters, which are different from the target crack geometry, will be assumed. Minimization of the objective function will occur if the estimated crack parameters \mathbf{p} approach the actual parameters, which are used to generate $\bar{V}_f(\omega_q)$. This is a large-scale and nonlinear optimization problem.

This objective function can be reduced to a simpler case when only a single frequency is used. This case requires only an incident wave with a specific frequency, so it can work for real-time health monitoring. However, the number of measurement points along the piezoelectric smart sensor will limit the monitoring capability. If there are only 4 data points at the piezoelectric smart sensor, this system will only be able to monitor more than one crack, which is characterized by its four parameters.

If only one frequency is used, Equation (5.8) can be reduced to

$$\min f(\mathbf{p}) = \frac{1}{2} \sum_{f=1}^{n_p} \|V_f(\mathbf{p}) - \bar{V}_f\|^2 \quad (5.9)$$

where \bar{V}_f is the known recorded voltage signal at n_p selected points described by $y_i, i=1,2,\dots,n_p$ and $V_f(\mathbf{p})$ is the surface voltage solution at the n_p selected points predicted by the direct problem for the crack parameters \mathbf{p} .

Multiple frequencies can be used to enhance the monitoring capability when limited signal points are available in a SHM system. If there are only 4 sensing points at the piezoelectric smart sensor, this system will still be able to identify more than one cracks if data from enough frequencies are collected. In the limiting case where only one is available, Equation (5.8) is reduced to

$$\min f(\mathbf{p}) = \frac{1}{2} \sum_{q=1}^{n_\omega} \|V(\mathbf{p}, \omega_q) - \bar{V}(\omega_q)\|^2 \quad (5.10)$$

where $\bar{V}(\omega_q)$ is the known recorded voltage under loading frequency ω_q and $V(\mathbf{p}, \omega_q)$ is the surface voltage solution predicted by the direct problem for the crack parameters \mathbf{p} and the frequency ω_q .

In the following discussion, attention will be paid to only the single frequency case.

5.3 Quantitative crack identification

By solving the previous direct and inverse problems, the crack parameters can be estimated from known voltage data from piezoelectric sensors. The flow chart for the crack identification process will be summarized, followed by the analysis of optimization methods.

The flow chart for the crack identification process is shown in Fig. 5.2. The inputs are the recorded voltage data, structural constants, loading data and the initial guess for crack parameters. The recorded data will be used to determine the objective function and the other three will be substituted into the direct problem solution for predicting the corresponding theoretical voltage output. After updating the crack parameters through the process, the estimated crack parameters will approach these of true cracks if convergence is achieved.

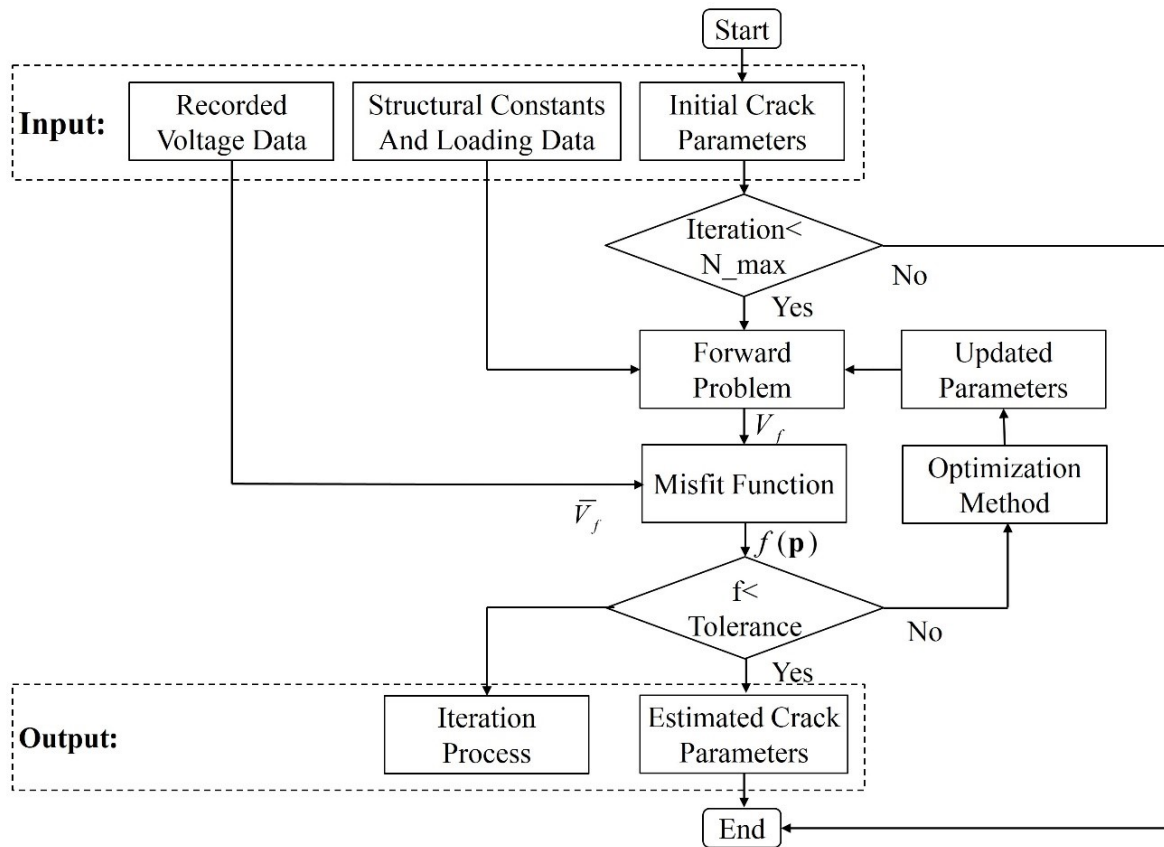


Fig. 5.2: The flow chart for the crack identification process using harmonic wave propagation and optimization method.

For the identification of cracks, a reasonable crack number needs to be assumed first. Ideally, if the maximum number of cracks is assumed to be n , the current model will be able

to identify not more than n cracks. The maximum crack number is limited by the sensor data and also limited by the convergence of the numerical process in optimization. For example, if there is only one crack, the results will be the parameters of this crack and 0 for all other $n-1$ cracks. When the number of existing cracks is larger than the capability the piezoelectric sensor, extra voltage data for different loading frequencies will be required to enhance the capability of the current system.

The problem is to find the solution minimizing the objective function $f(\mathbf{p})$ of $4n$ variables, where $\mathbf{p} = \{p_1, p_2, \dots, p_{4n}\}^T$ are the $4n$ crack parameters. Although the direct problem $V_f(\mathbf{p}, \omega_q)$ given by Equation 5.8 is linear with respect to the wave field but nonlinear regarding the crack parameters, this problem is a nonlinear minimization problem which is usually solved using Newton's methods (Métivier et al., 2013), because the rate of convergence is faster than most of other optimization methods. The Newton's method is to approximate the objective function by constructing a quadratic function, with its first and second derivatives at the current point match the corresponding values of the original objective function at this point. The quadratic approximation to $f(\mathbf{p})$ can be obtained from the second order Taylor expansion as

$$q(\mathbf{p}) = f(\mathbf{p}^{(k)}) + \mathbf{g}^{(k)}(\mathbf{p} - \mathbf{p}^{(k)}) + \frac{1}{2} H^{(k)}(\mathbf{p} - \mathbf{p}^{(k)})^2 \quad (5.11)$$

where $\mathbf{g}^{(k)} = f'(\mathbf{p}^{(k)})$ is the gradient of the function with respect to estimated parameters $\mathbf{p}^{(k)}$ with k being the iteration number, and the matrix $H^{(k)}$ is the corresponding Hessian matrix (Métivier et al., 2014) with $H^{(k)} = f''(\mathbf{p}^{(k)})$. Fig. 5.3 is a two-dimensional schematic diagram showing the iteration principle of the Newton method for finding the minimum. For each step

k , the minimizer of $q(\mathbf{p})$ is determined, which corresponds to a value of $\mathbf{p}^{(k)}$. In the next step $k+1$ of the iteration $\mathbf{p}^{(k)}$ will be used as the starting point. This procedure is repeated

$$\mathbf{p}^{(k+1)} = \mathbf{p}^{(k)} - \left(H^{(k)}\right)^{-1} \mathbf{g}^{(k)} \quad (5.12)$$

until a convergent solution is obtained for \mathbf{p} .

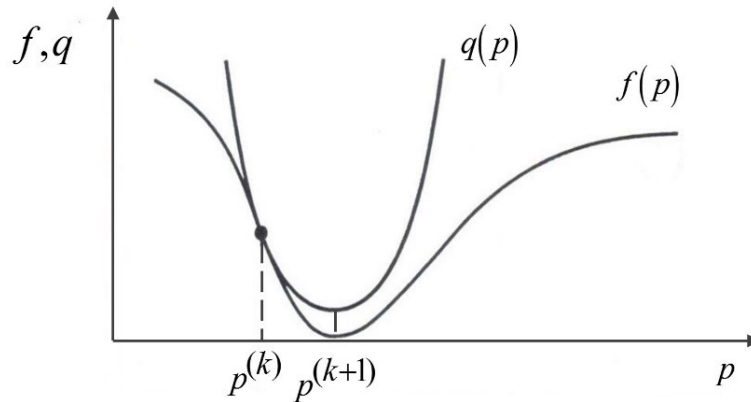


Fig. 5.3: A two-dimensional schematic diagram to show the iteration principle of the Newton method for finding the minimum.

The Newton's method will head in the descent direction of the objective function when the Hessian matrix is positive definite. But for the current problem, positive definite of Hessian matrix cannot be proved. In order to ensure the descent property of the Newton's method for the current problem, Equation (5.12) is modified as

$$\mathbf{p}^{(k+1)} = \mathbf{p}^{(k)} - \alpha_k \left(H^{(k)}\right)^{-1} \mathbf{g}^{(k)} \quad (5.13)$$

where α_k is the optimal step size in the direction of $-\left(H^{(k)}\right)^{-1} \mathbf{g}^{(k)}$, which can be determined through a one-dimensional search method, such as golden section search method and secant

method (Métivier et al., 2013). With this modification, it is guaranteed that $f(\mathbf{p}^{(k+1)}) < f(\mathbf{p}^{(k)})$ for any $\mathbf{g}^{(k)} \neq \mathbf{0}$.

The Newton's method requires computing the inverse of the hessian matrix \mathbf{H}^{-1} in every iteration and it is inefficient. Consequently, quasi-newton methods are adopted, and the inverse Hessian matrix is approximated using the Broyden-Fletcher-Goldfarb-Shanno (BFGS) algorithm (Bao and Wang, 2009). Based on BFGS algorithm, the inverse Hessian matrix can be approximated using the updating rules below

$$H_{k+1} = H_k + \left[1 + \frac{\Delta \mathbf{g}^{(k)T} H_k \Delta \mathbf{g}^{(k)}}{\Delta \mathbf{g}^{(k)T} \Delta \mathbf{p}^{(k)}} \right] \frac{\Delta \mathbf{p}^{(k)} \Delta \mathbf{p}^{(k)T}}{\Delta \mathbf{p}^{(k)T} \Delta \mathbf{g}^{(k)}} - \frac{H_k \Delta \mathbf{g}^{(k)} \Delta \mathbf{p}^{(k)T} + \left(H_k \Delta \mathbf{g}^{(k)} \Delta \mathbf{p}^{(k)T} \right)^T}{\Delta \mathbf{g}^{(k)T} \Delta \mathbf{p}^{(k)}} \quad (5.14)$$

where $\Delta \mathbf{p}^{(k)} = -\alpha_k H_k \mathbf{g}^{(k)}$, $\Delta \mathbf{g}^{(k)} = \mathbf{g}^{(k+1)} - \mathbf{g}^{(k)}$ and superscript T means matrix transpose. $\mathbf{g}^{(k)}$ is gradient vector obtained in the sensitivity analysis.

The BFGS optimization scheme is conducted to find the optimal estimated crack parameters \mathbf{p}^* from the recorded surface voltage signals of the piezoelectric sensor. The algorithm for this problem is summarized in the following 5 steps, as shown in Table 5.1. The BFGS algorithm guarantees that inverse Hessian matrix is positive definite in each iteration, so the iterative process has the descent property, which guarantees that the local minimum is obtained through the algorithm. If the initial crack parameters are not far from the optimal, the relatively accurate length, orientation and the position of the cracks can be identified through this algorithm. The selection of initial crack parameters will be discussed in the following section.

Table 5.1: The optimization algorithm for finding the optimal estimated crack parameters from the recorded surface voltage signals of the piezoelectric smart sensor.

-
- (a) Set $k = 0$; input structural constants, loading and recorded voltage data; select initial crack parameters $\mathbf{p}^{(0)}$ and H_0 (H_0 should be symmetric and positive definite).
- (b) Solve the direct problem; compute objective function $f(\mathbf{p}^{(k)})$ and gradient vector $\mathbf{g}^{(k)}$.
- (c) If $\mathbf{g}^{(k)} = \mathbf{0}$ or $f < tolerance$, output optimal crack parameters \mathbf{p}^* and stop; else find α_k that minimizes $f(\mathbf{p}^{(k)} - \alpha_k H_k \mathbf{g}^{(k)})$ and $\mathbf{p}^{(k+1)} = \mathbf{p}^{(k)} - \alpha_k H_k \mathbf{g}^{(k)}$.
- (d) Compute $\Delta \mathbf{p}^{(k)} = -\alpha_k H_k \mathbf{g}^{(k)}$, $\Delta \mathbf{g}^{(k)} = \mathbf{g}^{(k+1)} - \mathbf{g}^{(k)}$ and estimate H_{k+1} using Equation (5.14).
- (e) Set $k = k + 1$ and go to step (b).
-

5.4 Results and discussion

For an elastic isotropic and homogeneous structure with a surface attached piezoelectric sensor, a dynamic excitation can be applied by an exciter, such as ultrasonic transducers or piezoelectric actuators, to generate elastic wave propagation in it. When the wave encounters cracks, it will be scattered and the scattered wave will be recorded by the piezoelectric sensors. The recorded signals contain the signature of the cracks thus can be used to identify the parameters of the cracks using the optimization algorithm given in Table 5.1.

The material properties of the piezoelectric sensor and the host structure are same as these used in Chapter 4. The incident wave considered is a time-harmonic longitudinal plane wave propagating in the z -axis direction perpendicular to the sensor, given in Equation (4.59) with the incident angle $\Gamma = 90^\circ$. The half-length of the sensor is $a = 1.0\text{cm}$ and the

normalized wave number $Ka = 1.0$, with K is the longitudinal wave number. In the current theoretical study, the known voltage signals used in the inverse problem are provided by the solution of the direct problem solution from the pre-assumed crack parameters.

This following section will study some specific cases to show the effectiveness of the current crack identification method. Consider a specific case of a piezoelectric sensor with the thickness being $h=0.05a$ parallel to three uniformly distributed collinear cracks with the same half-length $c_1 = c_2 = c_3 = a/4$. The location of the centres of the three cracks are therefore $(-3a/4, -a/2)$, $(0, -a/2)$ and $(3a/4, -a/2)$. The configuration and geometric details are shown in Fig. 5.4.

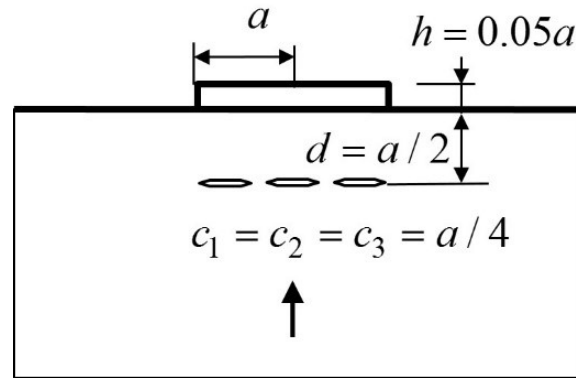


Fig. 5.4: Case 1 of three uniformly distributed collinear cracks parallel to the piezoelectric sensor subjected to a normal incident wave.

Using these crack parameters, the direct problem subjected to the incident wave with $Ka=1$ is solved to generate the voltage output of the sensor. The results are normalized by dividing the maximum voltage value V_0 for no crack case. The resulting voltage data at 12 selected locations along the sensor are given in Table 5.2.

Table 5.2: Known voltage signals at 12 selected locations along the piezoelectric sensor for case 1.

Number	1	2	3	4	5	6
Location y/a	0	0.05	0.10	0.15	0.20	0.25
Voltage V/V_0	1.1798	1.1703	1.1436	1.1023	1.0496	0.9897
Number	7	8	9	10	11	12
Location y/a	0.30	0.40	0.50	0.60	0.70	0.80
Voltage V/V_0	0.9265	0.7996	0.6738	0.5371	0.3797	0.2118

The voltage data at these 12 selected locations are substituted into the BFGS algorithm in Table 5.1. The algorithm starts from guessed initial parameters as shown in Table 5.3, which are different from the actual parameters. The iteration process of finding the optimal crack parameters is shown in Fig. 5.5. The figure shows that the rate of convergence is very quick, indicating suitability of the BFGS algorithm for this optimization problem.

The crack parameters predicted by the current method is also given in Table 5.3. Comparing with the actual parameters, the difference is very small. The very good agreement with the actual values theoretically demonstrates the accuracy and the effectiveness of this technique to identify cracks. It should be noted that the current crack identification is limited to theoretical study only. The inevitable noise in real structures has been ignored here, and experimental validation with noise being considered should be carried out in the future work.

Table 5.3: The estimated crack parameters for case 1.

Crack parameters	Actual parameters	Initial parameters	Estimated parameters
c_1 (mm)	0.25	1.0	0.251
ϕ_1 (°)	0	1.0	0.014
y_1^c (mm)	-0.75	1.0	-0.752
z_1^c (mm)	-0.5	-1.0	-0.501
c_2 (mm)	0.25	1.0	0.250
ϕ_2 (°)	0	1.0	0.011
y_2^c (mm)	0	1.0	0.000
z_2^c (mm)	-0.5	-2.0	-0.499
c_3 (mm)	0.25	1.0	0.251
ϕ_3 (°)	0	1.0	0.026
y_3^c (mm)	0.75	1.0	0.748
z_3^c (mm)	-0.5	-3.0	-0.501

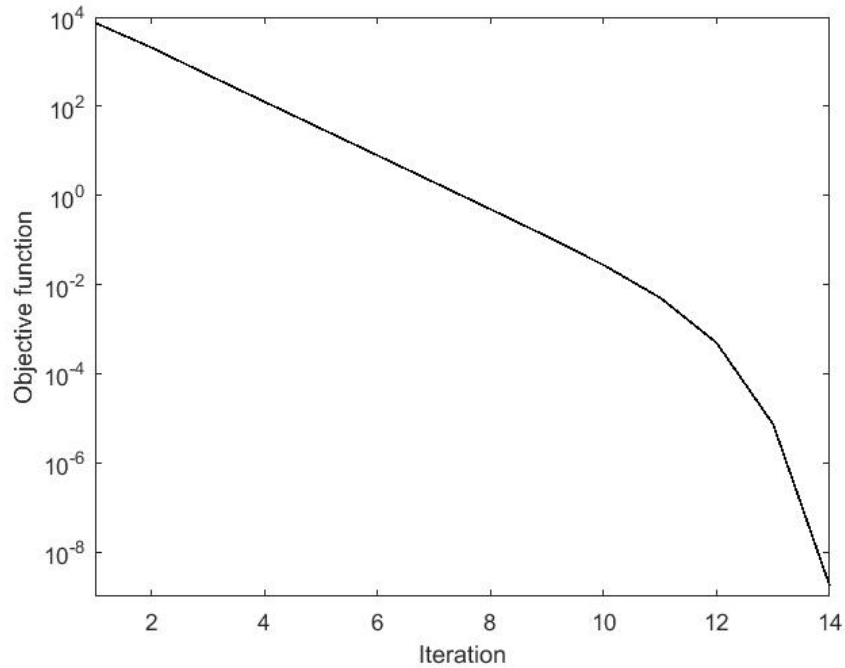


Fig. 5.5: The objective function vs iteration for case 1.

In case 2 of the crack identification, a similar configuration but with only one long crack with its half-length being $c=a$ is considered. The configuration and detailed geometry are shown in Fig. 5.6. This case will be compared with the previous three crack case to evaluate the sensitivity of the current method in distinguishing similar crack geometries. The voltage output of the sensor corresponding to these crack parameters is obtained from the solution of the direct problem and is given in Table 5.4. Similar to the previous case, the voltage output at 12 selected locations along the sensor is used.

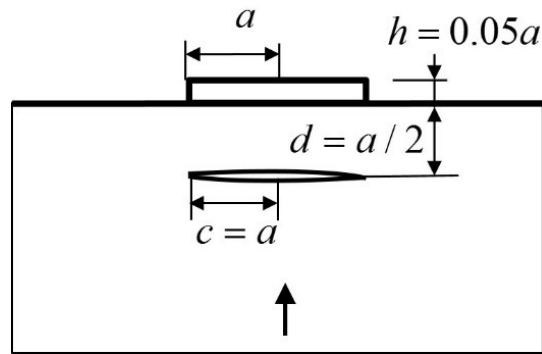


Fig. 5.6: Case 2 of one big crack parallel to the piezoelectric sensor subjected to a normal incident wave.

Table 5.4: Known voltage signals at 12 selected locations for case 2.

Number	1	2	3	4	5	6
Location y/a	0	0.05	0.10	0.15	0.20	0.25
Voltage V/V_0	0.0384	0.0356	0.0282	0.01615	-0.0002	-0.0205
Number	7	8	9	10	11	12
Location y/a	0.30	0.40	0.50	0.60	0.70	0.80
Voltage V/V_0	-0.0441	-0.0985	-0.1562	-0.2075	-0.2400	-0.2375

The optimization process is conducted by considering three possible cracks and using the crack parameters for the previous three crack case as the initial parameters, as given in Table 5.5. The iteration process is shown in Fig. 5.7. The rate of convergence is also very quick. The crack parameters predicted by the current method are in very good agreement with the actual values for the existing crack. The results predict accurately the parameters for the long crack and the other cracks are predicted to have almost zero lengths. This study clearly shows the reliability of the current approach in identifying cracks.

Table 5.5: The estimated crack parameters for case 2.

Parameters notation	Actual parameters	Initial parameters	Estimated parameters
c_1 (mm)	1.0	0.25	0.997
ϕ_1 (°)	0	0	0.062
y_1^c (mm)	0	-0.75	0.000
z_1^c (mm)	-0.5	-0.5	-0.500
c_2 (mm)	0	0.25	0.000
ϕ_2 (°)	0	0	0.003
y_2^c (mm)	0	0	0.000
z_2^c (mm)	0	-0.5	0.000
c_3 (mm)	0	0.25	0.000
ϕ_3 (°)	0	0	0.011
y_3^c (mm)	0	0.75	0.001
z_3^c (mm)	0	-0.5	0.000

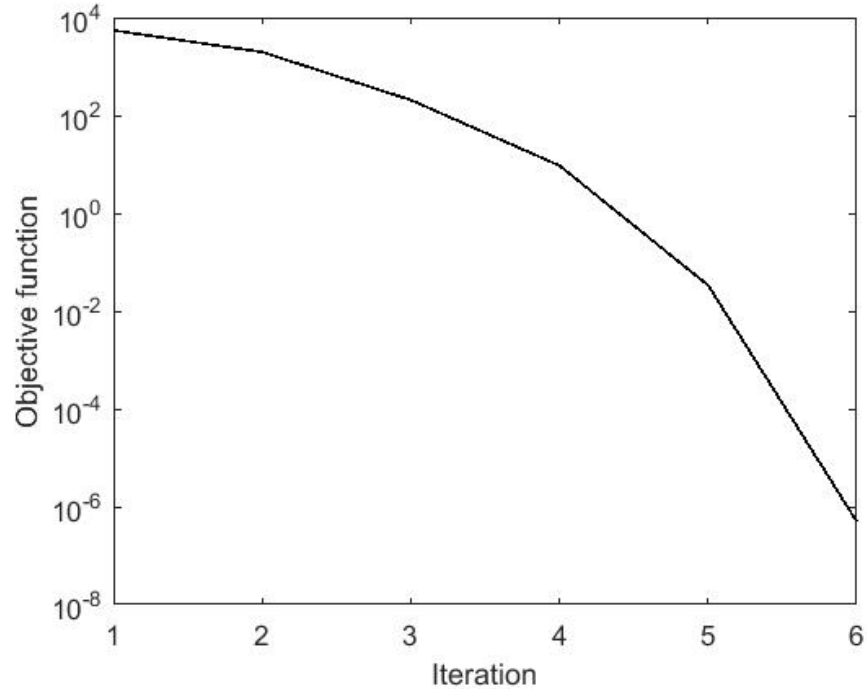


Fig. 5.7: The objective function vs the iteration number

The two cases considered represent two extreme cases, one long crack and closely packed small cracks. The results reliably predicted the crack geometries in both cases, showing the effectiveness and reliability of current method to identify embedded cracks theoretically. It should be mentioned that convergence can be easily achieved if reasonable initial values of the crack parameters are used. If the initial values are significantly far away from the expected ones, desirable convergence may not be available. For example, when the initial parameters are selected to be $c_1 = c_2 = c_3 = 100$ and all other parameters are 0, the optimization process will be convergent but the results are far from the expected parameters.

This method can identify crack parameters quantitatively using limited voltage signals of the piezoelectric sensor. The problem investigated is a strong nonlinear optimization problem with respect to multiple parameters. In addition, this problem is solved using local optimization methods. Thus, the initial parameters guessed should not be too far away from

the expected values to ensure convergence the global minimum rather than just to a local minimum.

In order to guarantee initial parameters are reasonable to converge to the global minimum in the crack detection of real structures, two approaches can be considered to help to choose the initial crack parameters for the identification. and make the current approach suitable for real application:

- (1) When continuous crack monitoring is available, the last known crack information can be used as the initial condition. By ensuring that the interval between two continuous detections is short enough, the crack status change will be in a reasonable range and this will guarantee the objective function is near the local minimum.
- (2) To conduct a typical Non-Destructive-Testing, such as B-Scan, to obtain an initial estimate of possible cracks. In this situation, the current method will serve as a further developed technique for quantitative identification of cracks.

5.5 Conclusions

A crack identification method is provided to quantitatively identify the position, the length and the orientation of cracks embedded in structures using the voltage output of the surface-bonded piezoelectric sensor. The explicit forms of the voltage output with respect to crack characteristics are obtained by solving the direct problem, i.e. the dynamic interaction problem. Inversely, this form and known sensor data are then used to identify the cracks by integrated them into a BFGS optimization process. Numerical examples are presented, which show rapid convergence and effectiveness of the current method in crack identification.

This chapter shows that the dynamic interaction can provide a richer description of interacting cracks, which enables the accurate identification of the cracks. At this stage, the theoretical investigation is completed and a framework is established to realize quantitative crack identification. To further apply this framework in practical applications, experimental validation will be conducted in future work.

Chapter 6: Contributions and future work

This chapter summarizes the main contributions of this thesis and suggests several problems that remain to be addressed in the future work.

6.1 Main contributions

This thesis conducted a systematic investigation of the dynamic behaviour of piezoelectric sensors, multiple scattering of elastic waves and its application on crack identification. Throughout this project, four major issues essential to the establishment of a piezoelectric based SHM system are studied, (1) how to model the piezoelectric sensor; (2) how elastic waves propagate in the piezoelectric coupled solid structures under time harmonic loading; (3) how elastic waves are scattered back and forth between cracks and sensors; (3) how to detect embedded cracks using the piezoelectric sensors.

Corresponding to these four major issues, the specific contributions of this project can be summarized as follows.

6.1.1 A new model for piezoelectric sensors/actuators with bending effect

This thesis develops a modified two-dimensional model of thin-sheet piezoelectric sensors/actuators, bonded to half planes. This sensor/actuator model is an extension of the one dimension model given in Wang and Meguid, (2000) with added bending effects. The electromechanical response of the sensor/actuator is studied under different mechanical and geometrical conditions to evaluate the effect of bending. Numerical examples are conducted to study the effects of the material properties, the geometry and interfacial debonding upon the load transfer between the actuator and the host structure.

6.1.2 A new analytical solution for dispersion relation in layered piezoelectric structures

The dispersion equations of layered piezoelectric structures normally can only be solved using pure numerical solution. This thesis develops an analytical dispersion equation, which reduces the complicated problem to a much simpler one using the new sensor model. The resulting eigen-value problem is much simpler yet captures major wave modes for the current layered piezoelectric structure. Typical examples are provided to illustrate the wave modes and the effects of the piezoelectricity, geometry and material properties. Comparison with exact results indicates that the current solution is accurate for low-order wave modes.

6.1.3 A new solution for dynamic interaction between piezoelectric sensors and cracks

A semi-analytical systematic methodology is established to simulate the complicated dynamic interaction among cracks and the piezoelectric sensor. Through this methodology, the original multiple scattering problem is reduced to the solution of coupled single crack problem and single piezoelectric sensor problem. The resulting integral equations governing the dynamic behaviour of single crack/sensor are solved by using Chebyshev polynomial expansion and the collocation point method. Numerical results of the voltage output and the dynamic stress field for different configurations and frequencies are determined and analyzed.

This methodology takes the advantages of the reliability of analytical solutions and the flexibility of numerical methods. It is very general and can provide a reliable simulation of complicated interaction problem.

6.1.4 A quantitative technique for quantitative crack identification

A crack identification technique is provided to quantitatively identify the position, the length and the orientation of cracks embedded in structures using the voltage output of the surface-bonded piezoelectric sensor. The calculated voltage output of the piezoelectric sensor in

response to the existence of multiple cracks and the known data are integrated into a BFGS optimization process to predict unknown crack parameters. Numerical examples show that this technique can potentially quantitatively identify multiple cracks effectively. But current examples are limited to near parallel crack cases, and more general cases need to be verified in the future work.

6.2 Future work

Although the work of this thesis has tried to cover the major gap found in the existing literature as stated in Chapter 1, some problems still need to be addressed in the future to extend the application of current methods.

1. Effect of interfacial debonding and structural boundaries

For piezoelectric based SHM systems, poor adhesive conditions and high-stress concentration may cause partial debonding between the piezoelectric sensor and the structure. The effect of debonding on the voltage output of the piezoelectric sensor should be studied. The scattered waves from these interfacial cracks can also be modelled in the similar method with dislocation density functions and traction free boundary conditions. Then, the current methodology for dynamic interaction problems can be extended to involve interfacial cracks. On the other hand, the host structure is idealized as a semi-infinite plane, which is corresponding to the case that the sensors and embedded cracks are far from boundaries. The current method can also be extended by considering the effect of other boundaries. The scattered or reflected wave from the boundaries can deal with using the superposition method similar to that for the free surface with piezoelectric sensors.

2. Different types of cracks

This thesis considered only through-thickness cracks to show the methodology and effectiveness of the current methods. In practical applications, different types of cracks, such as penny-shaped cracks may exist. The scattered wave of such cracks can be derived and substituted into the current method for dynamic interaction to evaluate the interaction between the crack and the sensor. This can then be used in the optimization process developed for the identification of these cracks.

3. Experiment validation

This thesis mainly focused on theoretical studies, which help us understand the dynamic behaviour of piezoelectric based SHM systems, multiple scattering of elastic waves and give insights into developing new methods for quantitative crack identification. However, these theoretical studies are based on some assumptions. Although they have been validated by comparing with existing results or simplified cases, the related experiments should be done in the future to further validate these theoretical solutions, especially the effectiveness of the optimization algorithm in practical applications for crack identification.

Bibliography

- Achenbach, J.D., 2002. Modeling for quantitative non-destructive evaluation. *Ultrasonics* 40, 1–10. doi:10.1016/S0041-624X(02)00083-5
- Achenbach, J.D., 1973. *Wave propagation in elastic solids*. North-Holland Pub. Co.
- Achenbach, J.D., Keshava, S.P., 1967. Free Waves in a Plate Supported by a Semi-Infinite Continuum. *J. Appl. Mech.* 34, 397–404. doi:10.1115/1.3607696
- Ang, W.-T., 2014. *Hypersingular Integral Equations in Fracture Analysis*. Elsevier.
- Ang, W.-T., 2007. *A Beginner's Course in Boundary Element Methods*. Universal-Publishers.
- Bailey, T., Ubbard, J.E., 1985. Distributed piezoelectric-polymer active vibration control of a cantilever beam. *J. Guid. Control Dyn.* 8, 605–611. doi:10.2514/3.20029
- Bakker, M.C.M., Verweij, M.D., 2002. An approximation to the far field and directivity of elastic wave transducers. *J. Acoust. Soc. Am.* 111, 1177–1188.
- Banks, H.T., Joyner, M.L., Wincheski, B., Winfree, W.P., 2002. Real time computational algorithms for eddy-current-based damage detection. *Inverse Probl.* 18, 795. doi:10.1088/0266-5611/18/3/318
- Banks, H.T., Smith, R.C., Wang, Y., 1996. *Smart material structures: modeling, estimation, and control*. John Wiley & Son Ltd.
- Bao, Y.G., Wang, X.D., 2011. Identification of multiple cracks based on optimization methods using harmonic elastic waves. *Int. J. Fract.* 172, 77–95. doi:10.1007/s10704-011-9649-z
- Bao, Y.G., Wang, X.D., 2009. Crack identification based on optimization methods using harmonic elastic waves. *Int. J. Fract.* 160, 1–18. doi:10.1007/s10704-009-9394-8
- Bellis, C., Bonnet, M., 2013. Qualitative identification of cracks using 3D transient elastodynamic topological derivative: Formulation and FE implementation. *Comput. Methods Appl. Mech. Eng.* 253, 89–105. doi:10.1016/j.cma.2012.10.006
- Bent, A.A., Hagood, N.W., Rodgers, J.P., 1995. Anisotropic Actuation with Piezoelectric Fiber Composites. *J. Intell. Mater. Syst. Struct.* 6, 338–349. doi:10.1177/1045389X9500600305
- Biemans, C., Staszewski, W.J., Boller, C., Tomlinson, G.R., 1999. Crack Detection in Metallic Structures Using Piezoceramic Sensors. *Key Eng. Mater.* 167–168, 112–121. doi:10.4028/www.scientific.net/KEM.167-168.112

- Boller, C., 2000. Next generation structural health monitoring and its integration into aircraft design. *Int. J. Syst. Sci.* 31, 1333–1349. doi:10.1080/00207720050197730
- Botteldooren, D., 1995. Finite-difference time-domain simulation of low-frequency room acoustic problems. *J. Acoust. Soc. Am.* 98, 3302–3308. doi:10.1121/1.413817
- Bromwich, T.J.I., 1898. On the Influence of Gravity on Elastic Waves and in particular on the Vibrations of an Elastic Globe. *Proc. Lond. Math. Soc.* s1-30, 98–120. doi:10.1112/plms/s1-30.1.98
- Chang, F.-K., Markmiller, J.F.C., Yang, J., Kim, Y., 2011. Structural Health Monitoring, in: Johnson, S.B., Gormley, T.J., Kessler, S.S., Mott, C.D., Patterson-Hine, A., Reichard, K.M., Jr, P.A.S. (Eds.), *System Health Management*. John Wiley & Sons, Ltd, pp. 419–428.
- Cheng, N.C., Sun, C.T., 1975. Wave propagation in two - layered piezoelectric plates. *J. Acoust. Soc. Am.* 57, 632–638. doi:10.1121/1.380479
- Crawley, E.F., Anderson, E.H., 1990. Detailed Models of Piezoceramic Actuation of Beams. *J. Intell. Mater. Syst. Struct.* 1, 4–25. doi:10.1177/1045389X9000100102
- Crawley, E.F., De Luis, J., 1987. Use of piezoelectric actuators as elements of intelligent structures. *AIAA J.* 25, 1373–1385. doi:10.2514/3.9792
- Cruse, T.A., 1972. Numerical evaluation of elastic stress intensity factors by the boundary-integral equation method. *The surface crack: Physical Problems and Computational Solutions* (American Society of Mechanical Engineers). pp 153-17.
- Datta, S.K., Shah, A.H., Al-Nassar, Y., Bratton, R.L., 1988. Elastic Wave Dispersion in Laminated Composite Plate, in: Thompson, D.O., Chimenti, D.E. (Eds.), *Review of Progress in Quantitative Nondestructive Evaluation*. Springer US, pp. 987–994.
- De Fenza, A., Sorrentino, A., Vitiello, P., 2015. Application of Artificial Neural Networks and Probability Ellipse methods for damage detection using Lamb waves. *Compos. Struct.* 133, 390–403. doi:10.1016/j.compstruct.2015.07.089
- Denoyer, K.K., Kwak, M.K., 1996. Dynamic modelling and vibration suppression of a swelling structure utilizing piezoelectric sensors and actuators. *J. Sound Vib.* 189, 13–31. doi:10.1006/jsvi.1996.0003
- Deraemaeker, A., Nasser, H., 2010. Numerical evaluation of the equivalent properties of Macro Fiber Composite (MFC) transducers using periodic homogenization. *Int. J. Solids Struct.* 47, 3272–3285. doi:10.1016/j.ijsolstr.2010.08.006
- Durão, L.M.P., Panzera, T.H., Scarpa, F., Filho, S.L.M.R., Oliveira, P.R., 2015. Damage assessment of fibre reinforced laminates. *Compos. Struct.* 133, 939–946. doi:10.1016/j.compstruct.2015.08.020

- Elachi, C., Zyl, J.J. van, 2006. Introduction To The Physics and Techniques of Remote Sensing. John Wiley & Sons.
- Gandhi, M.V., Thompson, B.S., 1992. Smart materials and smart structures. Chapman and Hall, London.
- Giurgiutiu, V., 2005. Tuned Lamb Wave Excitation and Detection with Piezoelectric Wafer Active Sensors for Structural Health Monitoring. *J. Intell. Mater. Syst. Struct.* 16, 291–305. doi:10.1177/1045389X05050106
- Glushkov, E.V., Glushkova, N.V., Eremin, A.A., Evdokimov, A.A., Lammering, R., 2016. Ultrasonic Guided Wave Characterization and Inspection of Laminate Fiber-Reinforced Composite Plates, in: Parinov, I.A., Chang, S.-H., Topolov, V.Y. (Eds.), *Advanced Materials, Springer Proceedings in Physics*. Springer International Publishing, pp. 449–457. doi:10.1007/978-3-319-26324-3_31
- Gross, D., Zhang, C., 1988. Diffraction of SH waves by a system of cracks: Solution by an integral equation method. *Int. J. Solids Struct.* 24, 41–49. doi:10.1016/0020-7683(88)90097-2
- Hagood, N.W., Kindel, R., Ghandi, K., Gaudenzi, P., 1993. Improving transverse actuation of piezoceramics using interdigitated surface electrodes. pp. 341–352. doi:10.1117/12.152766
- Han, J.-H., Lee, I., 1998. Analysis of composite plates with piezoelectric actuators for vibration control using layerwise displacement theory. *Compos. Part B Eng.* 29, 621–632. doi:10.1016/S1359-8368(98)00027-4
- Henneke, E.G., Reifsnider, K.L., Stinchcomb, W.W., 1979. Thermography — An NDI Method for Damage Detection. *JOM* 31, 11–15. doi:10.1007/BF03354475
- Horner, G., Teter, J., Robbins, W., Copeland, B., 2002. Piezoelectric composite device and method for making same. US20020038990 A1.
- Hoseini, M.R., Wang, X., Zuo, M.J., 2012. Estimating ultrasonic time of flight using envelope and quasi maximum likelihood method for damage detection and assessment. *Measurement* 45, 2072–2080. doi:10.1016/j.measurement.2012.05.008
- Hoseini, M.R., Zuo, M.J., Wang, X., 2013. Using ultrasonic pulse-echo B-scan signals for estimation of time of flight. *Measurement* 46, 3593–3599. doi:10.1016/j.measurement.2013.06.014
- Hosokawa, A., 2015. Numerical analysis of ultrasound backscattered waves in cancellous bone using a finite-difference time-domain method: isolation of the backscattered waves from various ranges of bone depths. *IEEE Trans. Ultrason. Ferroelectr. Freq. Control* 62, 1201–1210. doi:10.1109/TUFFC.2014.006946

- Huang, B., Kim, H.S., Yoon, G.H., 2015. Modeling of a partially debonded piezoelectric actuator in smart composite laminates. *Smart Mater. Struct.* 24, 075013. doi:10.1088/0964-1726/24/7/075013
- Huang, G., Song, F., Wang, X., 2010. Quantitative modeling of coupled piezo-elastodynamic behavior of piezoelectric actuators bonded to an elastic medium for structural health monitoring: a review. *Sensors* 10, 3681–3702.
- Huang, G.L., Wang, X.D., 2006. On the dynamic behaviour of interfacial cracks between a piezoelectric layer and an elastic substrate. *Int. J. Fract.* 141, 63–73.
- Hurlebaus, S., Gaul, L., 2004. Smart Layer for Damage Diagnostics. *J. Intell. Mater. Syst. Struct.* 15, 729–736. doi:10.1177/1045389X04041937
- Ihn, J.-B., Chang, F.-K., 2004. Detection and monitoring of hidden fatigue crack growth using a built-in piezoelectric sensor/actuator network: I. Diagnostics. *Smart Mater. Struct.* 13, 609. doi:10.1088/0964-1726/13/3/020
- Im, S., Atluri, S.N., 1989. Effects of a piezo-actuator on a finitely deformed beam subjected to general loading. *AIAA J.* 27, 1801–1807. doi:10.2514/3.10337
- Itou, S., 1980. Diffraction of an antiplane shear wave by two coplanar griffith cracks in an infinite elastic medium. *Int. J. Solids Struct.* 16, 1147–1153. doi:10.1016/0020-7683(80)90069-4
- Jain, Anjana, K. J., P., Sharma, A.K., Jain, Arpit, P.n, R., 2015. Dielectric and piezoelectric properties of PVDF/PZT composites: A review. *Polym. Eng. Sci.* 55, 1589–1616. doi:10.1002/pen.24088
- Jain, D.L., Kanwal, R.P., 1972. Diffraction of elastic waves by two coplanar and parallel rigid strips. *Int. J. Eng. Sci.* 10, 925–937. doi:10.1016/0020-7225(72)90002-X
- Jin, C., Wang, X., 2011. Analytical modelling of the electromechanical behaviour of surface-bonded piezoelectric actuators including the adhesive layer. *Eng. Fract. Mech.* 78, 2547–2562.
- Jin, Congrui, Wang, X., 2011. The Effect of Adhesive Layers on the Dynamic Behavior of Surface-bonded Piezoelectric Sensors with Debonding. *J. Intell. Mater. Syst. Struct.* 22, 655–670. doi:10.1177/1045389X11404956
- Jin, F., Qian, Z., Wang, Z., Kishimoto, K., 2005. Propagation behavior of Love waves in a piezoelectric layered structure with inhomogeneous initial stress. *Smart Mater. Struct.* 14, 515. doi:10.1088/0964-1726/14/4/009
- Jin, J., Wang, Q., Quek, S.T., 2002. Lamb wave propagation in a metallic semi-infinite medium covered with piezoelectric layer. *Int. J. Solids Struct.* 39, 2547–2556. doi:10.1016/S0020-7683(02)00091-4

- Kielczyński, P., Pajewski, W., Szalewski, M., 1990. Shear horizontal surface waves on piezoelectric ceramic with layered structure. *Appl. Phys. A* 50, 301–304. doi:10.1007/BF00324496
- Kim, S.J., Jones, J.D., 1996. Effects of Piezo-Actuator Delamination on the Performance of Active Noise and Vibration Control Systems. *J. Intell. Mater. Syst. Struct.* 7, 668–676. doi:10.1177/1045389X9600700606
- Kögl, M., Bucalem, M.L., 2005. A family of piezoelectric MITC plate elements. *Comput. Struct., Modelling of Smart Structures* 83, 1277–1297. doi:10.1016/j.compstruc.2004.04.025
- Kwak, M.K., Sciulli, D., 1996. Fuzzy-logic based vibration suppression control experiments on active structures. *J. Sound Vib.* 191, 15–28.
- Lee, J., Mal, A.K., 1995. A volume integral equation technique for multiple scattering problems in elastodynamics. *Appl. Math. Comput.* 67, 135–159. doi:10.1016/0096-3003(94)00057-B
- Li, P., Cheng, L., He, Y., Jiao, S., Du, J., Ding, H., Gao, J., 2016. Sensitivity boost of rosette eddy current array sensor for quantitative monitoring crack. *Sens. Actuators Phys.* 246, 129–139. doi:10.1016/j.sna.2016.05.023
- Liu, H., Wang, Z.K., Wang, T.J., 2001. Effect of initial stress on the propagation behavior of Love waves in a layered piezoelectric structure. *Int. J. Solids Struct.* 38, 37–51. doi:10.1016/S0020-7683(00)00009-3
- Liu, J., Yu, H., 2017. Concurrent deposition path planning and structural topology optimization for additive manufacturing. *Rapid Prototyp. J.* 23. doi:10.1108/RPJ-05-2016-0087
- Liu, J., Yu, H., Ma, Y., 2016. Minimum void length scale control in level set topology optimization subject to machining radii. *Comput.-Aided Des.* 81, 70–80. doi:10.1016/j.cad.2016.09.007
- Love, A.E.H., 1911. Some problems of geodynamics [WWW Document]. CERN Doc. Serv. URL <http://cds.cern.ch/record/466884> (accessed 10.7.16).
- Ludwig, R., Lord, W., 1996. A finite-element study of ultrasonic wave propagation and scattering in an aluminum block. *NDT E Int.* 4, 256.
- Martin, P.A., 2006. *Multiple Scattering*. Cambridge University Press.
- Masahiro Inoue, Hiroe Ssaki, Katsuaki Suganuma, Toshimi Kawasaki, Tetsuo Rokuhara, Takahiro Miyashita and Hiroshi Ishiguro, 2007. Development of an Electronic Packaging Technique Using Conductive Adhesives for Novel Human Machine Interfaces. *Azo J. Mater.* Volume 3. doi:10.2240/azojomo0257

- Meguid, S.A., Wang, X.D., 1995. On the Dynamic Interaction between a Microdefect and a Main Crack. *Proc. R. Soc. Lond. Ser. Math. Phys. Sci.* 448, 449–464. doi:10.1098/rspa.1995.0027
- Meng, W.-J., Zhou, L., Yuan, F.-G., 2006. A pre-stack reverse-time migration method for multidamage detection in composite structure. pp. 617444-617444–10. doi:10.1117/12.685446
- Métivier, L., Bretaudeau, F., Brossier, R., Operto, S., Virieux, J., 2014. Full waveform inversion and the truncated Newton method: quantitative imaging of complex subsurface structures. *Geophys. Prospect.* 62, 1353–1375. doi:10.1111/1365-2478.12136
- Métivier, L., Brossier, R., Virieux, J., Operto, S., 2013. Full Waveform Inversion and the Truncated Newton Method. *SIAM J. Sci. Comput.* 35, B401–B437. doi:10.1137/120877854
- Modest, M.F., 2013. Radiative Heat Transfer. Academic Press.
- Mseddi, S., Tekeli, F., Njeh, A., Donner, W., Ben Ghazlen, M.H., 2016. Effect of initial stress on the propagation behavior of SAW in a layered piezoelectric structure of ZnO/Al₂O₃. *Mech. Res. Commun.* 76, 24–31. doi:10.1016/j.mechrescom.2016.06.005
- Munoz, V., Valès, B., Perrin, M., Pastor, M.L., Weleman, H., Cantarel, A., Karama, M., 2016. Damage detection in CFRP by coupling acoustic emission and infrared thermography. *Compos. Part B Eng.* 85, 68–75. doi:10.1016/j.compositesb.2015.09.011
- Muskhelishvili, N.I., 1977. Some Basic Problems of the Mathematical Theory of Elasticity. Springer Netherlands, Dordrecht.
- Na, S., Lee, H.K., 2013. A multi-sensing electromechanical impedance method for non-destructive evaluation of metallic structures. *Smart Mater. Struct.* 22, 095011. doi:10.1088/0964-1726/22/9/095011
- Nayfeh, A.H., 1995. Wave Propagation in Layered Anisotropic Media: with Application to Composites. Elsevier.
- Norris, A.N., Achenbach, J.D., 1982. Mapping of a crack edge by ultrasonic methods. *J. Acoust. Soc. Am.* 72, 264–272. doi:10.1121/1.387988
- Pak, Y.E., 1990. Crack Extension Force in a Piezoelectric Material. *J. Appl. Mech.* 57, 647–653. doi:10.1115/1.2897071
- Pang, Y., Liu, J.-X., Wang, Y.-S., Zhao, X.-F., 2008. Propagation of Rayleigh-type surface waves in a transversely isotropic piezoelectric layer on a piezomagnetic half-space. *J. Appl. Phys.* 103, 074901-074901-8. doi:doi:10.1063/1.2902501

- Pang, Y., Liu, Y.-S., Liu, J.-X., Feng, W.-J., 2016. Propagation of SH waves in an infinite/semi-infinite piezoelectric/piezomagnetic periodically layered structure. *Ultrasonics* 67, 120–128. doi:10.1016/j.ultras.2016.01.007
- Park, J.-M., Kim, D.-S., Han, S.-B., 2000. Properties of interfacial adhesion for vibration controllability of composite materials as smart structures. *Compos. Sci. Technol.* 60, 1953–1963. doi:10.1016/S0266-3538(00)00081-6
- Peng, S., Zheng, X., Sun, J., Zhang, Y., Zhou, L., Zhao, J., Deng, S., Cao, M., Wei Xiong, Peng, K., 2012. Modeling of a micro-cantilevered piezo-actuator considering the buffer layer and electrodes. *J. Micromechanics Microengineering* 22, 065005. doi:10.1088/0960-1317/22/6/065005
- Pham, C.V., Vu, T.N.A., 2014. An approximate secular equation of Rayleigh waves in an isotropic elastic half-space coated with a thin isotropic elastic layer. *Acta Mech.* 225, 2539–2547. doi:10.1007/s00707-014-1090-8
- Phased Array Sectorial Scans | Olympus IMS [WWW Document], n.d. URL <http://www.olympus-ims.com/en/ndt-tutorials/instrumentation/pa-scan/> (accessed 11.3.16).
- Qian, Z., Jin, F., Hirose, S., 2010. A novel type of transverse surface wave propagating in a layered structure consisting of a piezoelectric layer attached to an elastic half-space. *Acta Mech. Sin.* 26, 417–423. doi:10.1007/s10409-010-0336-5
- Qian, Z.-H., Hirose, S., 2012. Theoretical validation on the existence of two transverse surface waves in piezoelectric/elastic layered structures. *Ultrasonics* 52, 442–446. doi:10.1016/j.ultras.2011.10.007
- Rabinovitch, O., Vinson, J.R., 2002. Adhesive Layer Effects in Surface-Mounted Piezoelectric Actuators. *J. Intell. Mater. Syst. Struct.* 13, 689–704. doi:10.1177/1045389X02013011001
- Ramadan, K.S., Sameoto, D., Evoy, S., 2014. A review of piezoelectric polymers as functional materials for electromechanical transducers. *Smart Mater. Struct.* 23, 033001. doi:10.1088/0964-1726/23/3/033001
- Reddy, J.N., 1999. On laminated composite plates with integrated sensors and actuators. *Eng. Struct.* 21, 568–593. doi:10.1016/S0141-0296(97)00212-5
- Ren, W., Liu, J., Tian, G.Y., Gao, B., Cheng, L., Yang, H., 2013. Quantitative non-destructive evaluation method for impact damage using eddy current pulsed thermography. *Compos. Part B Eng.* 54, 169–179. doi:10.1016/j.compositesb.2013.05.004
- Saadon, S., Sidek, O., 2011. A review of vibration-based MEMS piezoelectric energy harvesters. *Energy Convers. Manag.* 52, 500–504. doi:10.1016/j.enconman.2010.07.024

- Schafbuch, P.J., Thompson, R.B., Rizzo, F.J., 1990. Application of the boundary element method to elastic wave scattering by irregular defects. *J. Nondestruct. Eval.* 9, 113–127. doi:10.1007/BF00566388
- Schulz, M.J., Pai, P.F., Inman, D.J., 1999. Health monitoring and active control of composite structures using piezoceramic patches. *Compos. Part B Eng.* 30, 713–725. doi:10.1016/S1359-8368(99)00034-7
- Shi, Y., Pinna, C., Soutis, C., 2014. Modelling impact damage in composite laminates: A simulation of intra- and inter-laminar cracking. *Compos. Struct.* 114, 10–19. doi:10.1016/j.compstruct.2014.03.052
- Sodano, H.A., 2007. Development of an Automated Eddy Current Structural Health Monitoring Technique with an Extended Sensing Region for Corrosion Detection. *Struct. Health Monit.* 6, 111–119. doi:10.1177/1475921706072065
- Staszewski, W., Boller, C., Tomlinson, G.R., 2004. *Health Monitoring of Aerospace Structures: Smart Sensor Technologies and Signal Processing.* John Wiley & Sons.
- Su, Z., Ye, L., 2009. Introduction, in: *Identification of Damage Using Lamb Waves, Lecture Notes in Applied and Computational Mechanics.* Springer London, pp. 1–14. doi:10.1007/978-1-84882-784-4_1
- Su, Z., Ye, L., Lu, Y., 2006. Guided Lamb waves for identification of damage in composite structures: A review. *J. Sound Vib.* 295, 753–780.
- Sun, D., Tong, L., 2003. Closed-loop based detection of debonding of piezoelectric actuator patches in controlled beams. *Int. J. Solids Struct.* 40, 2449–2471. doi:10.1016/S0020-7683(03)00080-5
- Sun, D., Tong, L., Atluri, S.N., 2001. Effects of piezoelectric sensor/actuator debonding on vibration control of smart beams. *Int. J. Solids Struct.* 38, 9033–9051. doi:10.1016/S0020-7683(01)00180-9
- Sun, H., Waisman, H., Betti, R., 2013. Nondestructive identification of multiple flaws using XFEM and a topologically adapting artificial bee colony algorithm. *Int. J. Numer. Methods Eng.* 95, 871–900. doi:10.1002/nme.4529
- Sun, J.-H., Wu, T.-T., 2007. Propagation of acoustic waves in phononic-crystal plates and waveguides using a finite-difference time-domain method. *Phys. Rev. B* 76, 104304. doi:10.1103/PhysRevB.76.104304
- Sun, R., McMechan, G.A., 1986. Pre-stack reverse-time migration for elastic waves with application to synthetic offset vertical seismic profiles. *Proc. IEEE* 74, 457–465. doi:10.1109/PROC.1986.13486
- Tan, K.T., Watanabe, N., Iwahori, Y., 2011. X-ray radiography and micro-computed tomography examination of damage characteristics in stitched composites subjected

- to impact loading. *Compos. Part B Eng.* 42, 874–884. doi:10.1016/j.compositesb.2011.01.011
- Tiersten, H.F., 1969. Elastic Surface Waves Guided by Thin Films. *J. Appl. Phys.* 40, 770–789. doi:10.1063/1.1657463
- Tylikowski, A., 2001. Effects of piezoactuator delamination on the transfer functions of vibration control systems. *Int. J. Solids Struct.* 38, 2189–2202.
- Tzou, H.S., Tseng, C.I., 1991. Distributed vibration control and identification of coupled elastic/piezoelectric systems: Finite element formulation and applications. *Mech. Syst. Signal Process.* 5, 215–231. doi:10.1016/0888-3270(91)90044-6
- Usamentiaga, R., Venegas, P., Guerediaga, J., Vega, L., Molleda, J., Bulnes, F.G., 2014. Infrared Thermography for Temperature Measurement and Non-Destructive Testing. *Sensors* 14, 12305–12348. doi:10.3390/s140712305
- Varadan, V.K., Varadan, V.V., Pao, Y.-H., 1978. Multiple scattering of elastic waves by cylinders of arbitrary cross section. I. SH waves. *J. Acoust. Soc. Am.* 63, 1310–1319. doi:10.1121/1.381883
- Vinh, P.C., Anh, V.T.N., Linh, N.T.K., 2016. Exact secular equations of Rayleigh waves in an orthotropic elastic half-space overlaid by an orthotropic elastic layer. *Int. J. Solids Struct.* 83, 65–72. doi:10.1016/j.ijsolstr.2015.12.032
- Vinh, P.C., Linh, N.T.K., 2012. An approximate secular equation of Rayleigh waves propagating in an orthotropic elastic half-space coated by a thin orthotropic elastic layer. *Wave Motion* 49, 681–689. doi:10.1016/j.wavemoti.2012.04.005
- Wandowski, T., Malinowski, P., Ostachowicz, W., Rawski, M., Tomaszewicz, P., Luba, T., Borowik, G., 2015. Embedded Damage Localization Subsystem Based on Elastic Wave Propagation. *Comput.-Aided Civ. Infrastruct. Eng.* 30, 654–665. doi:10.1111/mice.12129
- Wang, C., Wang, X., 2016. Modeling and simulation of wave scattering of multiple inhomogeneities in composite media. *Compos. Part B Eng.* 90, 341–350. doi:10.1016/j.compositesb.2016.01.010
- Wang, Q., Quek, S.T., Varadan, V.K., 2001. Love waves in piezoelectric coupled solid media. *Smart Mater. Struct.* 10, 380. doi:10.1088/0964-1726/10/2/325
- Wang, X., Yu, H., Abdel-Gawad, S., Wang, C., 2015. On the pseudo-incident wave technique for interacting inhomogeneities in electromechanical problems. Presented at the COUPLED PROBLEMS 2015 - Proceedings of the 6th International Conference on Coupled Problems in Science and Engineering, Venice, Italy.
- Wang, X.D., Huang, G.L., 2006a. Wave propagation generated by piezoelectric actuators attached to elastic substrates. *Acta Mech.* 183, 155–176.

- Wang, X.D., Huang, G.L., 2006b. The coupled dynamic behavior of piezoelectric sensors bonded to elastic media. *J. Intell. Mater. Syst. Struct.* 17, 883–894.
- Wang, X.D., Huang, G.L., 2004a. Identification of embedded cracks using back-propagating elastic waves. *Inverse Probl.* 20, 1393.
- Wang, X.D., Huang, G.L., 2004b. Study of elastic wave propagation induced by piezoelectric actuators for crack identification. *Int. J. Fract.* 126, 287–306.
- Wang, X.D., Huang, G.L., 2001. Wave Propagation in Electromechanical Structures: Induced by Surface-Bonded Piezoelectric Actuators. *J. Intell. Mater. Syst. Struct.* 12, 105–115. doi:10.1106/MHD5-0N62-24EH-8B9T
- Wang, X.D., Meguid, S.A., 2000. On the electroelastic behaviour of a thin piezoelectric actuator attached to an infinite host structure. *Int. J. Solids Struct.* 37, 3231–3251.
- Wang, X.D., Meguid, S.A., 1997. Diffraction of SH-Wave by Interacting Matrix Crack and an Inhomogeneity. *J. Appl. Mech.* 64, 568–575. doi:10.1115/1.2788930
- Waterman, P.C., 1965. Matrix formulation of electromagnetic scattering. *Proc. IEEE* 53, 805–812. doi:10.1109/PROC.1965.4058
- Wilkie, W.K., Bryant, R.G., High, J.W., Fox, R.L., Hellbaum, R.F., Jalink, J., Anthony, Little, B.D., Mirick, P.H., 2000. Low-cost piezocomposite actuator for structural control applications. pp. 323–334. doi:10.1117/12.388175
- Williams, R.B., Park, G., Inman, D.J., Wilkie, W.K., 2002. An overview of composite actuators with piezoceramic fibers. *Proceeding IMAC XX* 4–7.
- Yu, H., Wang, X., 2016. Modelling and simulation of surface-bonded piezoelectric actuators with bending effects. *J. Intell. Mater. Syst. Struct.* in press.
- Zhang, C., 1992. Elastodynamic Analysis of a Periodic Array of Mode III Cracks in Transversely Isotropic Solids. *J. Appl. Mech.* 59, 366–371. doi:10.1115/1.2899529
- Zhang, C., Achenbach, J.D., 1989. Time-domain boundary element analysis of dynamic near-tip fields for impact-loaded collinear cracks. *Eng. Fract. Mech.* 32, 899–909. doi:10.1016/0013-7944(89)90006-4
- Zhao, M., Dang, H., Li, Y., Fan, C., Xu, G., 2016. Displacement and temperature discontinuity boundary integral equation and boundary element method for analysis of cracks in three-dimensional isotropic thermoelastic media. *Int. J. Solids Struct.* 81, 179–187. doi:10.1016/j.ijsolstr.2015.11.024
- Zhu, R., Huang, G.L., Yuan, F.G., 2013. Fast damage imaging using the time-reversal technique in the frequency–wavenumber domain. *Smart Mater. Struct.* 22, 075028. doi:10.1088/0964-1726/22/7/075028

Zou, Y., Tong, L., Steven, G.P., 2000. Vibration-based model-dependent damage (delamination) identification and health monitoring for composite structures - a review. *J. Sound Vib.* 230, 357–378. doi:10.1006/jsvi.1999.2624

Appendix

Appendix A: The governing equations of piezoelectric materials

In the rectangular Cartesian coordinates, the equations of motion without body force are given by

$$\sigma_{ji,j} = \rho \frac{\partial^2 u_i}{\partial t^2} \quad (\text{A.1})$$

and the Gauss' law

$$D_{i,i} = 0. \quad (\text{A.2})$$

The constitutive equations of piezoelectric materials are given by (Kögl and Bucalem, 2005)

$$\begin{bmatrix} \sigma_{xx} \\ \sigma_{yy} \\ \sigma_{zz} \\ \sigma_{yz} \\ \sigma_{xz} \\ \sigma_{xy} \\ D_x \\ D_y \\ D_z \end{bmatrix} = \begin{bmatrix} c_{11} & c_{12} & c_{13} & & & & & & & e_{31} \\ c_{12} & c_{11} & c_{13} & & & & & & & e_{31} \\ c_{13} & c_{13} & c_{33} & & & & & & & e_{33} \\ & & & c_{44} & & & & & & e_{15} \\ & & & & c_{44} & & e_{15} & & & \\ & & & & & c_{66} & & & & \\ & & & & e_{15} & & -\lambda_{11} & & & \\ & & & e_{15} & & & & -\lambda_{11} & & \\ e_{31} & e_{31} & e_{33} & & & & & & & -\lambda_{33} \end{bmatrix} \begin{bmatrix} \varepsilon_{xx} \\ \varepsilon_{yy} \\ \varepsilon_{zz} \\ 2\varepsilon_{yz} \\ 2\varepsilon_{xz} \\ 2\varepsilon_{xy} \\ -E_x \\ -E_y \\ -E_z \end{bmatrix} \quad (\text{A.3})$$

$$= \begin{bmatrix} \mathbf{c} & \mathbf{e} \\ \mathbf{e}^T & -\boldsymbol{\lambda} \end{bmatrix} \begin{bmatrix} \boldsymbol{\varepsilon} \\ -\mathbf{E} \end{bmatrix}$$

Where

$$\varepsilon_{ij} = \frac{1}{2}(u_{i,j} + u_{j,i}), E_i = -V_{,i}, \quad i, j = x, y, z. \quad (\text{A.4})$$

In above equations, σ_{ij} , ε_{ij} and u_i are the stress components, the strain components and the mechanical displacements, while D_i , E_i and V represent the electric displacements, the

electric field intensity and the potentials, respectively. c_{ij} are the stiffness parameters for a constant electric potential, λ_{ij} are the dielectric constants, e_{ij} are the piezoelectric constants, and ρ is the mass density.

Then, the governing equations of the piezoelectric material can be obtained by combining these equations together, as

$$\begin{aligned} c_{11}u_{x,xx} + c_{66}u_{x,yy} + c_{44}u_{x,zz} + (c_{12} + c_{66})u_{y,xy} + (c_{13} + c_{44})u_{z,xz} + (e_{31} + e_{15})V_{,xz} &= \rho'' \\ (c_{12} + c_{66})u_{x,yx} + c_{66}u_{y,xx} + c_{11}u_{y,yy} + c_{44}u_{y,zz} + (c_{13} + c_{44})u_{z,yz} + (e_{31} + e_{15})V_{,yz} &= \rho'' \\ (c_{13} + c_{44})u_{x,zx} + (c_{13} + c_{44})u_{y,zy} + c_{44}u_{z,xx} + c_{44}u_{z,yy} + c_{33}u_{z,zz} + e_{15}V_{,xx} + e_{15}V_{,yy} + e_{33}V_{,zz} &= \rho'' \\ (e_{31} + e_{15})u_{x,xz} + (e_{31} + e_{15})u_{y,yz} + e_{15}u_{z,xx} + e_{15}u_{z,yy} + e_{33}u_{z,zz} - \lambda_{11}V_{,xx} - \lambda_{11}V_{,yy} - \lambda_{33}V_{,zz} &= 0 \end{aligned}$$

Appendix B: One-dimensional piezoelectric sensor model

According to the electro-elastic line model of piezoelectric sensors (Wang and Meguid, 2000), the stress component σ_y and the electric displacement D_z under plane strain condition can be obtained as,

$$\begin{aligned} \sigma_y &= E \frac{\partial u_y}{\partial y} - eE_z \\ D_z &= e \frac{\partial u_y}{\partial y} + \lambda E_z \end{aligned} \quad (\text{A.5})$$

with

$$E = c_{11} - \frac{c_{13}^2}{c_{33}}, \quad e = e_{13} - e_{33} \frac{c_{13}}{c_{33}}, \quad \lambda = \lambda_{33} + \frac{e_{33}^2}{c_{33}}. \quad (\text{A.6})$$

When the electric displacement across the piezoelectric layer $D_z = 0$, the stress component σ_y can be determined as

$$\sigma_y = E_{eff} \frac{\partial u_y}{\partial y} \quad (\text{A.7})$$

with $E_{eff} = E + \frac{e^2}{\lambda}$.

Appendix C: Dynamic interaction of multiple cracks

The method developed in Chapter 4 can also be used for dynamic interaction of multiple cracks in an infinite medium. Attention will be focused on the dynamic SIFs caused by the incident wave with the effect of crack interaction. The SIFs can be determined from Equation (4.62) after determining all Chebyshev polynomial coefficients, which are the solutions of Equation (4.58). The dynamic SIFs of other cracks can be also determined from Equation (4.62) in the same way. The SIFs of two collinear cracks with difference lengths subjected to a longitudinal incident wave have been determined and compared in the comparison with existing results. In this part, we first study the effect of the distance between two cracks on the dynamic SIFs, followed by the effect of the orientation of cracks. It should be noted that the dynamic SIFs induced by a time-harmonic incident wave are in general complex quantities. For convenience, only the amplitude of the SIFs is considered in the following figures.

The dynamic interaction of two collinear cracks is studied first to analyze the dynamic interaction. For two collinear cracks with the same length subjected to a longitudinal incident wave, the dynamic SIFs for difference distance between the two cracks can be determined, as shown in Fig. A.1. The figure reveals that the dynamic SIFs will be affected by the distance of the two cracks. For the low frequency, the dynamic SIF will become much larger with the decrease of the distance between two cracks, which means the effect of the collinear crack

will be larger upon the stress concentration at the right tip of the first crack when their distance becomes smaller. It is observed that the dynamic SIFs will become larger with the increase of the frequency and achieve the maximum value when the frequency is below $kc=1$. After passing the maximum value, they will decrease with the increase of the frequency and emerge almost together after $kc>2.5$. The maximum dynamic SIFs are larger than that corresponding to the static case, which is the well-known dynamic overshoot phenomenon. For high frequencies, which correspond to shorter wavelengths, the dynamic interaction between the cracks will become insignificance when the wavelength is smaller than the distance between cracks. We can conclude that the dynamic interaction should be considered when kc is relatively small, such as $kc<1$.

To further study the phenomenon, the dynamic SIFs for difference distance $d=2.2, 3, 8, 10, 20$ are plotted in Fig. A.2. The errors of dynamic SIFs with and without considering the dynamic interaction are defined by the maximum difference between the SIF of single crack and that of two collinear cracks with the same length $2c$. The errors for different distances between two crack centres are obtained and given in Table A.1. The error for $d/c=10$ is 3.12%, and for $d/c=8$ is 7.47%. The dynamic interaction of two collinear cracks under time harmonic loadings can be ignored when the distances of the crack centre $d>10c$ under an error of around 3%.

Table A.1: The errors of dynamic SIFs with and without considering the dynamic interaction for different distance d between the centres of two collinear cracks.

Distance d/c	3	8	10	20
Error	14.74%	7.47%	3.12%	1.99%

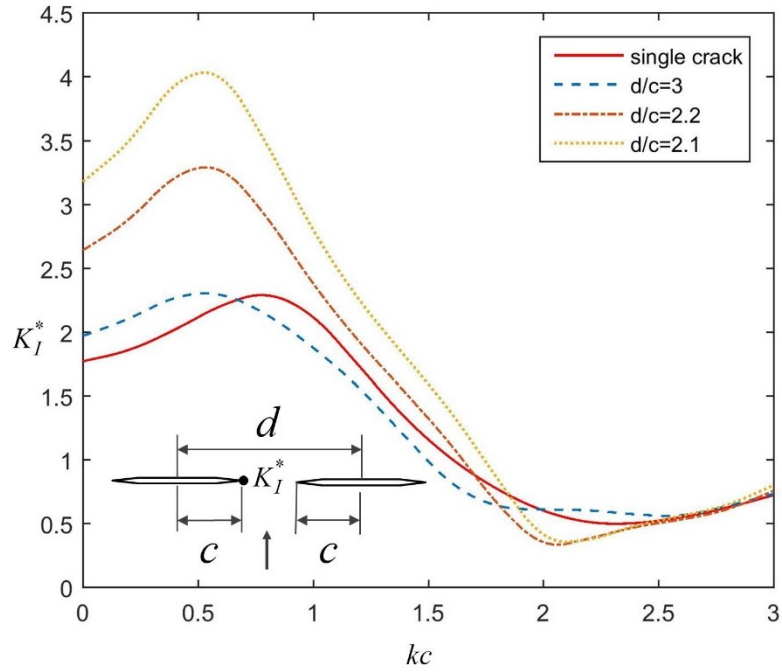


Fig. A.1: Normalized dynamic SIFs versus kc for different distances d between two near collinear cracks induced by a normal incident wave.

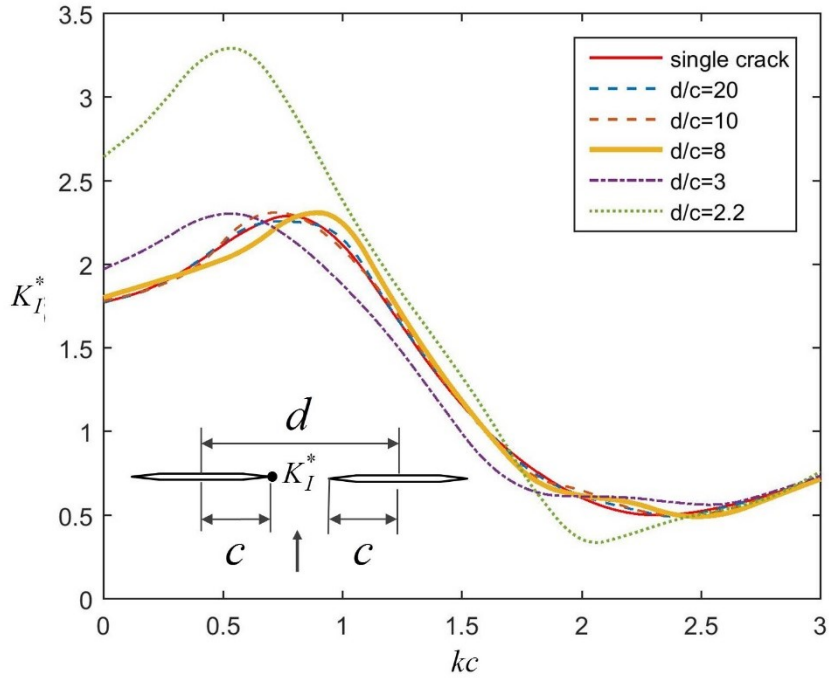


Fig. A.2: Normalized dynamic SIFs versus kc for different distances d between two collinear cracks induced by a normal incident wave.

Fig. A.3 shows the variation of normalized dynamic SIFs versus normalized wave number kc for different orientation angles of two interacting cracks induced by a normal incident wave. The configuration of cracks is also included in the figure. From the figure, all of the curves have the similar trend, increasing first and then decreasing with the increase of frequencies. For low frequency, $\theta = 0^\circ$ achieves the maximum dynamic SIFs while $\theta = 90^\circ$ achieves the minimum. This can be explained by the distance of two closest tips of cracks.

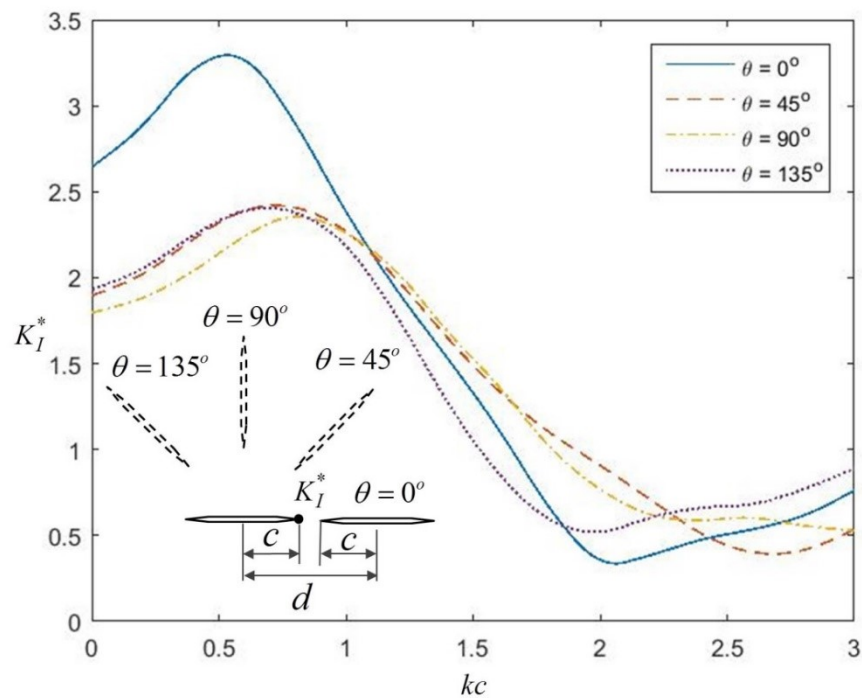


Fig. A.3: Normalized dynamic SIFs versus normalized wave number kc for different orientation angles induced by a normal incident wave.